Developing Strategies to Control Reactivity and Selectivity in Catalytic Transformations

by

Mark Alexander Mantell

A dissertation submitted in partial fulfillment
of the requirements for the degree of
Doctor of Philosophy
(Chemistry)
in the University of Michigan
2020

Doctoral Committee:

Professor Melanie Sanford, Chair
Professor Bryan Goldsmith
Professor Adam Matzger
Professor Nathaniel Szymczak

Mark Alexander Mantell

mmantell@umich.edu

ORCID iD: 0000-0003-1549-865X

Acknowledgements

I would first like to thank my family, without whom I never would have made it this far. My parents were incredibly supportive from the beginning, guiding me through high school, sending me to college, and being a source of regular advice throughout this entire process. I would also like to thank my amazing fiancée Lindsay, whom I met at Michigan and without whom none of this would be possible. I can't wait to spend my life with you.

I would next like to thank my advisor, Prof. Melanie Sanford. She was always ready to listen and provide insight into my problems, and her never-failing ability to think outside the box really drove my chemistry to success. Thank you for giving me the opportunity to work in your lab, this was an experience I'll never forget. Go Pats!

I would like to thank my undergraduate advisor at Worcester Polytechnic Institute, Prof. Marion Emmert. Working in your lab was some of the most fun I have had in chemistry, and you really inspired me to pursue this path. I wish you the best wherever life takes you, and I can't thank you enough for pushing me to reach for the doctorate.

I would like to thank my committee for their continued support. Thank you to Prof. Nate Szymczak for allowing me to rotate in your lab, where I learned a ton about inorganic synthesis and gained a lot of skills that I still use several years down the road. Thank you to Prof. Adam Matzger for being a strong voice in my early subgroup meetings and for your support in the job application process. Talking to you was always a pleasure, and you made those meetings considerably more fun to attend. Thank you to Prof. Bryan Goldsmith, for stepping up in my time of need.

I would like to give a special thanks to all of the amazing chemists and friends that have surrounded me since I joined the lab. Nomaan, Danielle, and BJ were my first lab bay-mates, and you all made the early days of my time in the lab a ton of fun. Nomaan, thank you for being a mentor as I got started, and BJ thank you for your help with MOFs and for being an amazing roommate. I would like to thank Sydonie for being an amazing mentor on the borylation chemistry. I would like to thank Prof. Courtney Roberts, without whom I would very genuinely not be defending my thesis. Thank you for your support both chemical and personal. Thank you to Kuam, who was an amazing bouncing board for talking about chemistry, politics, and life. Thank you to Anuska for commiserating with me in my final year, and Liz for all of the fun through our time here. Thank you to Ellen for being an amazing desk buddy, and thanks to Yiyang for being a great help with the Dow project and everything surrounding it.

Thank you to the amazing support staff that has helped me along the way: Andrew Higgs, Tom Veid, Liz Oxford, Kate Dyki, Nick O'Hair, Marc Hanosh, and Kaite Foster. Thank you for helping me to reach this point. Thank you to Dr. Jeff Kampf for your support in crystallography and to James Windak for countless trainings in instrumentation.

Table of Contents

List of Schemes

List of Figures

List of Tables

ABSTRACT

This thesis focuses on: (1) the development of catalysts for the C–H borylation of methane (Chapter 2); (2) the development of new methods for C(sp^2)–N bond formation with pyridine nucleophiles (Chapter 3); and (3) attempts to develop and study new catalytic reactions for the synthesis of aryl isocyanates (Chapter 4).

Chapter 2 describes the development of new Cp^RRh catalysts for the C–H borylation of methane with B_2Pin_2. Previous methods achieve high yields of borylated methane product but are susceptible to over-borylation of methane. We first aimed to decrease the amount of over-borylated product formed relative to the desired mono-borylated product through ligand design. Novel sterically bulky Cp^R ligands have been designed, and their efficacy evaluated both through experimental and computational methods. Our studies show that increasing the steric bulk of the Cp^R ligand decreases the amount of over-borylated product formed relative to the desired mono-borylated product. This principle is next applied to other C(sp^3)–H and C(sp^2)–H systems.

Chapter 3 describes the development of a photochemical method for the selective pyridination of electron rich arenes. First, the development, optimization, and selectivity of a photocatalytic coupling between aryl halides and pyridine is described. In contrast to related literature reports, this reaction proceeds with selectivity for cleaving C(sp^2)–halogen versus C(sp^2)–OR bonds. Second, these studies reveal that, under oxidizing conditions (under air with added TEMPO), selectivity can be switched to achieve the C(sp^2)–H pyridination of the same types of substrates. The scope, selectivity, and mechanistic aspects of this transformation are studied in

detail. Notably, with aryl ether substrates this C(sp^2)–H pyridination proceeds with an unusual preference for formation of *ortho*-substituted products.

Finally, Chapter 4 describes efforts to synthesize aryl isocyanates without the requirement for phosgene. The metal-catalyzed dehydrogenation of formanilides and the Cu-catalyzed coupling of aryl electrophiles with metal cyanates are both explored.

CHAPTER 1

Introduction

1.1. Significance of C–B and C–N Bonds

Compounds containing C–B bonds have received attention over recent years as important starting materials toward the forging of C–C bonds via the Suzuki-Miyaura cross-coupling. This reaction has emerged as a critical reaction in medicinal chemistry, appearing in over 20% of medicinal chemistry publications in 2014.[1] The Suzuki-Miyaura cross-coupling is often limited in its application by availability of the appropriate borylated starting material. Therefore, due to the rising prevalence of this reaction, new ways to synthesize the borylated starting materials are necessary in order to access the complex molecules which are in consistent demand.

Compounds containing aryl C–N bonds are ubiquitous in pharmaceuticals, agrichemicals, and in materials chemistry. Representing important functional groups like anilines, amides, and aryl ureas, compounds containing at least one aryl C–N bond made up over 40% of the top 200 selling small molecule pharmaceuticals in 2018 (**Figure 1.1.**).[2] Aryl C–N bonds are also present in important polymeric materials; for instance, polyurethane alone carries a demand of 2.0×10^7 tons per annum.[3] As such, development of new or milder methods for the installation of aryl C–N bonds remains of constant interest.

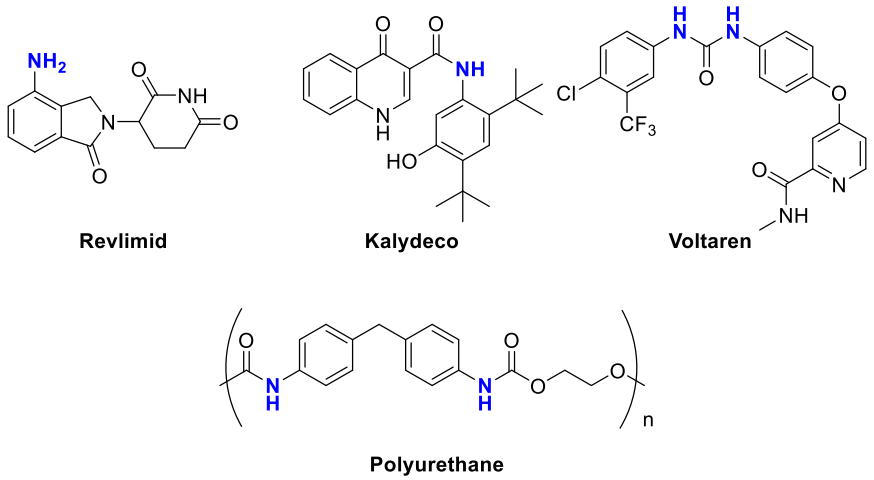

Figure 1.1. Representative examples of pharmaceuticals and polymers containing aryl C–N bonds.

1.2. Formation of C–B Bonds by C–H Activation

The most common methods employed for C–B bond formation prior to the development of C–H borylation reactions relied on prefunctionalized starting materials. Formation of an aryl Grignard from an aryl halide followed by further reaction with a borate or by a palladium catalyzed coupling between an aryl halide and a diboron reagent represent the most widely used methods to from aryl C–B bonds. Methods for installing alkyl C–B bonds were also reliant on prefunctionalized starting materials. Hydroboration reactions represent an important class of reaction which allowed the formation of C–B bonds between an alkene and a borane to form an alkyl C–B bond.[4]

The earliest examples of C–H borylation were stoichiometric borylation reactions described by Hartwig and coworkers, utilizing stoichiometric cyclopentadienyl (Cp) iron or tungsten carbonyl compounds bearing a catechol borane (Bcat) group. These reactions installed Bcat groups on aryl, alkyl, or vinyl C–H positions through photochemical processes.[5,6,7] Continued

study of this photochemical process led to the development of the first example of catalytic alkane borylation, described using a pentamethylcyclopentadienyl (Cp*) rhenium carbonyl complex, which produced high yields of primary alkylboronate esters.[8] These reactions were effective for introducing boryl groups to alkanes, but were quite slow. They often required over two days to reach high yields of borylated product.

A critical advance was made in catalytic C–H borylation when Hartwig and coworkers described an extremely active Cp*Rh catalyst capable of borylating both alkanes and arenes in high yields (**Figure 1.2.**).[9] This reaction showed a distinct preference for primary C–H bonds over secondary C–H bonds in alkane systems, denoting a strong steric control in alkane borylation. The reaction showed a tolerance for heteroatoms, and a preference for more electron-poor C–H bonds, such as those adjacent to fluoroalkyl groups.[10] Smith and coworkers reported on the regioselectivity of the rhodium catalyzed borylation of arenes using the same rhodium catalyst, observing that borylation was also largely sterically controlled in these systems by noting that little borylation occurred *ortho* to a bulky substitution on an arene.[11] A mechanistic investigation of this rhodium-catalyzed borylation was conducted by Hall and coworkers, who were the first to suggest that this reaction may also be applicable to methane.[12]

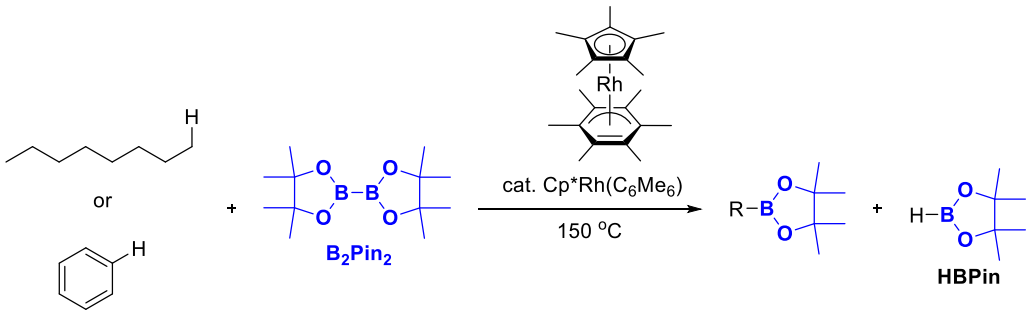

Figure 1.2. Cp*Rh(C_6Me_6) catalyzed C–H borylation using bispinacolatodiboron (B_2Pin_2) as described by Hartwig and coworkers.[9]

While many other metals have been reported to promote C–H borylation reactions, borylation reactions utilizing iridium-based complexes are gaining particular popularity in medicinal chemistry due to their allowance for lower temperatures and lower catalyst loadings.[13] Early work by Smith and coworkers detailed the stoichiometric C-H borylation of arenes with indenyl iridium cyclooctadienyl (COD) catalysts with bis-phosphine ligands.[14] These systems were later improved by the use of 4,4'-di-tert-butyl-2,2'-bipyridine as ligand and iridium di-cyclooctene (COE) chloride dimer as the iridium starting material, which promoted high yields of arene borylation at room temperature utilizing sub-stoichiometric quantities of iridium.[15] A large number of borylation systems using iridium complexes were reported, with several studying the regioselectivity of C–H borylation of (hetero)arenes.[16,17] These systems generally rely on substrate-controlled selectivity, with bulky groups on the substrates driving borylation to a less hindered site, as detailed in the stoichiometric example in **Figure 1.3.**

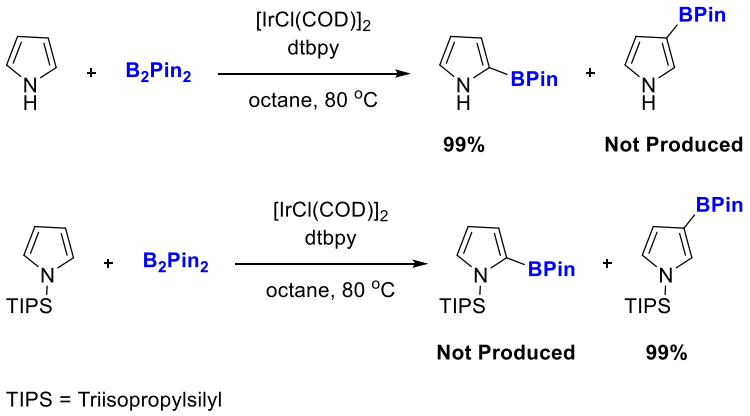

Figure 1.3. An example of substrate-controlled selectivity for C–H borylation of heteroarenes.[16]

Chapter 2 of this thesis is focused on the further development of the rhodium-catalyzed borylation of methane, and the use of ligand design to affect the selectivity of that borylation

reaction. It will also discuss the effect of ligand design on borylation of other systems, including selectivity in other alkane systems and the regioselective borylation of (hetero)arenes.

1.3. Formation of C–N Bonds

Currently, electrophilic nitration then reduction of the nitro group to free aniline is the most commonly used method to install a C(sp^2)–N bond.[18] This process requires the use of large amounts of strong acid, which can reduce its overall functional group tolerance and hinder its use in late-stage functionalization. Additionally, this reaction exhibits poor selectivity, resulting in over-functionalization or mixtures of isomeric products. This nitration-reduction sequence is used on commercial scale for the synthesis of aniline for polyurethane production. In an effort to discover a more economical and selective amination reaction, development of new methodologies that forge these bonds remains at a high interest. Several catalytic methods have arisen, and two general methods will be discussed here: metal catalyzed C–N bond formation and photochemical C–N bond formation.

Metal-catalyzed C–N bond formation through the Buchwald-Hartwig amination is currently one of the most used reactions in medicinal chemistry (**Figure 1.4.**).[1,19,20] This palladium-catalyzed reaction couples aryl halides with amines to form aryl amines in high yields, representing one of the chief ways these bonds are built in the synthesis of new pharmaceuticals and agrichemicals.[21] Copper-catalyzed reactions like the Chan-Lam coupling of aryl boronic esters and amines (**Figure 1.4.**),[22] have begun to emerge as researchers seek to avoid the use of more expensive palladium catalysts. Copper and palladium catalyzed reactions have also been described for the direct installation of isocyanates, an important functional group necessary for the synthesis

of polyurethane, without the need for an aniline intermediate.[23,24] While these reactions are effective for installing C–N bonds, they require the use of potentially expensive metal catalysts and pre-functionalized starting materials, and rarely yield the unprotected aniline or isocyanate product.

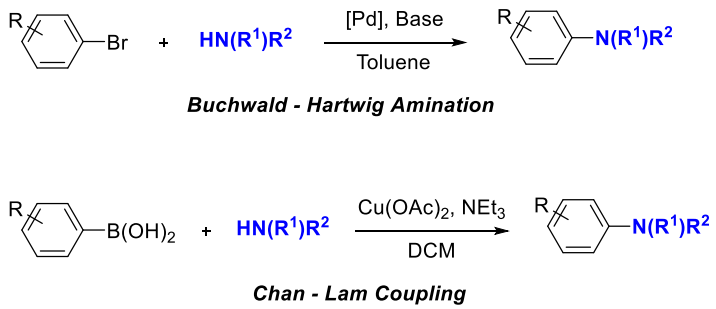

Figure 1.4. Metal catalyzed amination through the Buchwald-Hartwig and Chan-Lam couplings.

Rather than relying on prefunctionalized starting materials like in other metal catalyzed C–N bond forming reactions, C–H amination has emerged as a route of interest, although regioselectivity remains a challenge. Regioselective metal catalyzed C–H amination has been achieved, but, as reported by Daugulis and coworkers[25] and Shen and coworkers,[26] it is typically limited to substrates bearing a directing group. Photochemical processes have also been utilized for C-H amination in an effort to avoid the need for metal catalysts. While some early work focused on chemical oxidants,[27] studies by Sanford and coworkers[28] described formation of aryl amines by the photochemical generation of nitrogen centered radicals. This process is largely unselective on activated substrates and relies on highly specific carboxyl phthalimides to install the phthalimide group.

Later work by Nicewicz and coworkers details a more selective photocatalyzed amination of electron-rich arenes using a unique acridinium photocatalyst (**Figure 1.5.**).[29] This process is more versatile than earlier examples, installing either azole functional groups or free anilines

through the use of a carbamate-based ammonia surrogate. While the yields for this process are high, only the installation of azoles is selective, favoring the *para* product. The carbamate-based system that installs free anilines is almost entirely unselective, affording mixtures of *ortho*- and *para*- isomers. These reactions proceed through generation of an arene centered radical cation followed by attack of a nucleophile, a strategy that subsequent publications have expanded upon.[30,31,32]

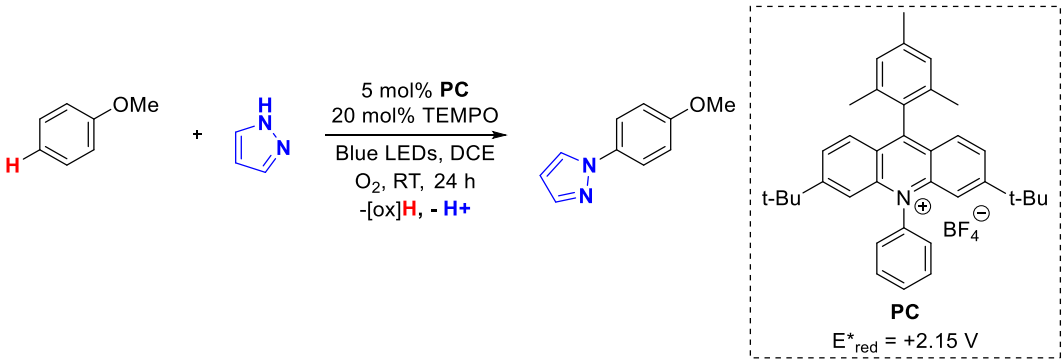

Figure 1.5. C–H amination system as described by Nicewicz and coworkers.

Chapter 3 of this thesis will focus on photocatalyzed formation of pyridinium salts with electron rich arenes. Chapter 4 of this thesis will focus on C–N bond formation by metal-catalyzed or mediated processes and focus on the formation of isocyanate groups.

1.4. References

[1] Brown, D. G.; Boström, J. Analysis of past and present synthetic methodologies on medicinal chemistry: Where have all the new reactions gone? *J. Med. Chem.* **2016**, *59*, 4443-4458.

[2] McGrath, N. A.; Brichacek, M.; Njardarson, J. T. A graphical journey of innovative organic architectures that have improved our lives. *J. Chem. Ed.* **2010**, *87*, 1348-1349.

[3] Brereton, G., Emanuel, R.M., Jr, Lomax, R., Pennington, K., Ryan, T., Tebbe, H., Timm, M., Ware, P., Winkler, K., Yuan, T., Zhu, Z., Adam, N., Avar, G., Blankenheim, H., Friederichs, W., Giersig, M., Weigand, E., Halfmann, M., Wittbecker, F.-W., Larimer, D.-R., Maier, U., Meyer-Ahrens, S., Noble, K.-L. and Wussow, H.-G. Polyurethanes. *Ullmann's Encyclopedia of Industrial Chemistry* **2019**.

[4] Burgess, K.; Ohlmeyer, M. J.; Transition-metal-promoted hydroborations of alkenes, emerging methodology for organic transformations. *Chem. Rev.* **1991**, *91*, 1179-1191.
[5] Mkhalid, I. A. I.; Barnard, J. H.; Marder, T. B.; Murphy, J. M.; Hartwig, J. F. C–H activation for the construction of C–B bonds. *Chem. Rev.* **2010**, *110*, 890-931.
[6] Waltz, K. M.; He, X.; Muhoro, C.; Hartwig, J. F. Hydrocarbon functionalization by transition metal boryls. *J. Am. Chem. Soc.* **1995**, 117, 45, 11357-11358
[7] Waltz, K. M.; Hartwig, J. F. Selective functionalization of alkanes by transition-metal boryl complexes. *Science* **1997**, *277*, 211-213.
[8] Chen, H.; Hartwig, J. F. Catalytic, regiospecific end-functionalization of alkanes: Rhenium-catalyzed borylation under photochemical conditions. *Angew. Chem., Int. Ed.* **1999**, *38*, 3391-3393.
[9] Chen, H.; Schlecht, S.; Semple, T. C.; Hartwig, J. F. Thermal, catalytic, regiospecific functionalization of alkanes. *Science* **2000**, *287*, 1995-1997.
[10] Lawrence, J. D.; Takahashi, M.; Bae, C.; Hartwig, J. F. Regiospecific functionalization of methyl C-H bonds of alkyl groups in reagents with heteroatom functionality. *J. Am. Chem. Soc.* **2004**, *126*, 15334-15335.
[11] Cho, J. Y.; Iverson, C. N.; Smith, M. R. Steric and chelate directing effects in aromatic borylation. *J. Am. Chem. Soc.* **2000**, *122*, 12868-12869.
[12] Hartwig, J. F; Cook, K. S.; Hapke, M.; Incarvito, C. D.; Fan, Y.; Webster, C. E.; Hall, M. B. Rhodium boryl complexes in the catalytic, terminal functionalization of alkanes. *J. Am. Chem. Soc.* **2005**, *127*, 2538-2552.
[13] Cernak, T.; Dykstra, K. D.; Tyagarajan, S.; Vachal, P.; Krska, S. W. The medicinal chemist's toolbox for late stage functionalization of drug-like molecules. *Chem. Soc. Rev.* **2016**, *45*, 546-576.
[14] Cho, J. Y.; Tse, M. K.; Holmes, D.; Maleczka, R. E.; Smith, M. R. Remarkably selective iridium catalysts for the elaboration of aromatic C–H bonds. *Science* **2002**, *295*, 305-308.
[15] Boller, T. M.; Murphy, J. M.; Hapke, M.; Ishiyama, T.; Miyaura, N.; Hartwig, J. F. Mechanism of the mild functionalization of arenes by diboron reagents catalyzed by iridium complexes. Intermediacy and chemistry of bipyridine-ligated iridium trisboryl complexes. *J. Am. Chem. Soc.* **2005**, *127*, 14263-14278.
[16] Takagi, J.; Sato, K.; Hartwig, J. F.; Ishiyama, T.; Miyaura, N. Iridium-catalyzed C–H coupling reaction of heteroaromatic compounds with bis(pinacolato)diboron: regioselective synthesis of heteroaryl boronates. *Tet. Lett.* **2002**, *43*, 5649-5651.
[17] Ishiyama, T.; Takagi, J.; Yonekawa, Y.; Hartwig, J. F.; Miyaura, N. Iridium-catalyzed direct borylation of five-membered heteroarenes by bis(pinacolato)diboron: Regioselective, stoichiometric, and room temperature reactions. *Adv. Synth. Catal.* **2003**, *345*, 1103-1106.
[18] Kahl, T.; Schröder, K. W.; Lawrence, F. R.; Marshall, W. J.; Höke, H.; Jäckh, R. Aniline. In Ullmann's Encyclopedia of Industrial Chemistry, (Ed.). 2011.
[19] Paul, F.; Patt, J.; Hartwig, J. F. Palladium-catalyzed formation of carbon-nitrogen bonds. Reaction intermediates and catalyst improvements in the hetero cross-coupling of aryl halides and tin amides. *J. Am. Chem. Soc.* **1994**, *116*, 5969−5970.
[20] Guram, A. S.; Rennels, R. A.; Buchwald, S. L. A simple catalytic method for the conversion of aryl bromides to arylamines. *Angew. Chem., Int. Ed.* **1995**, *34*, 1348−1350.
[21] Ruiz-Castillo, P.; Buchwald, S. L. Applications of palladium-catalyzed C–N cross-coupling reactions. *Chem. Rev.* **2016**, *116*, 12564-12649.
[22] Lam, P. Y. S.; Clark, C. G.; Saubern, S.; Adams, J.; Winters, M. P.; Chan, D. M. T.; Combs, A. New aryl/heteroaryl C–N bond cross-coupling reactions via arylboronic acid/cupric acetate arylation. *Tet. Lett.* **2001**, *42*, 3415-3418.
[23] Yang, X.; Zhang, Y.; Ma, D. Synthesis of aryl carbamates *via* copper-catalyzed coupling of aryl halides and potassium cyanate. *Adv. Synth. Catal.* **2012**, *354* 2443-2446.
[24] Vinogradova, E. V.; Fors, B. P.; Buchwald, S. L. Palladium-catalyzed cross-coupling of aryl chlorides and triflates with sodium cyanate: A practical synthesis of unsymmetrical ureas. *J. Am. Chem. Soc.* **2012**, *134*, 11132-11135.
[25] Tran, L. D.; Roane, J.; Daugulis, O. Directed amination of non-acidic arene C–H Bonds by a copper–silver catalytic system. *Angew. Chem. Int. Ed.* **2014**, *52*, 6043-6046.
[26] Xu, H.; Qiao, X.; Yang, S.; Shen, Z. Cu-catalyzed direct amidation of aromatic C–H bonds: An access to arylamines. *J. Org. Chem.* **2014**, *79*, 4414-4422.
[27] Kim, H. J.; Kim, J.; Cho, S. H.; Chang, S. Intermolecular oxidative C–N bond formation under metal-free conditions: control of chemoselectivity between aryl sp^2 and benzylic sp^3 C–H bond imidation. *J. Am. Chem. Soc.* **2011**, *133*, 16382-16385.
[28] Allen, L. J.; Cabrera, P. J.; Lee, M.; Sanford, M. S. N-Acyloxyphthalimides as nitrogen radical precursors in the visible light photocatalyzed room temperature C−H amination of arenes and heteroarenes. *J. Am. Chem. Soc.* **2014**, *136*, 5607-5610.

[29] Romero, N. A.; Margrey, K. A.; Tay, N. E.; Nicewicz, D. A. Site-selective arene C–H amination via photoredox catalysis. *Science* **2015**, *349*, 1326-1330.
[30] Tay, N. E. S.; Nicewicz, D. A. Cation radical accelerated nucleophilic aromatic substitution via organic photoredox catalysis. *J. Am. Chem. Soc.* **2017**, *139*, 16100-16104.
[31] Huang, H.; Strater, Z. M.; Rauch, M.; Shee, J.; Sisto, T. J.; Nuckolls, C.; Lambert, T. H.; Electrophotocatalysis with a trisaminocyclopropenium radical dication. *Angew. Chem.* **2019**, *131*, 13452-13456.

[32] Huang, H.; Lambert, T. H.; Electrophotocatalytic S_NAr reactions of unactivated aryl fluorides at ambient temperature and without base. *Angew. Chem. Int. Ed.* **2020**, *59*, 658-662.

CHAPTER 2

Catalytic Methane Borylation

2.1. Introduction

Metal-catalyzed C–H borylation is a strategy that has been used to add boryl (-$B(OR)_2$) groups into organic molecules. These are valuable as they serve as functional group handles for further functionalization to a wide range of substrates. The earliest examples of such transformations featured both arenes and simple linear alkanes as substrates and utilized rhodium and iridium catalysts.[1,2,3,4] Several reports have more deeply investigated the selectivity of rhodium- and iridium-catalyzed borylation reactions, finding that steric factors generally govern selectivity. In the iridium and rhodium-catalyzed C–H borylation of arenes systems, this commonly manifests in *meta*- or *para*-selectivity, with borylation occurring remote to a bulky substituent.[2,5,6,7] In alkane systems, using these catalysts, borylation occurs in very low yields on secondary carbon atoms due to high steric interference, leading almost exclusively functionalization of primary C–H bonds.[1,8] Additionally, multiple borylations of the same primary carbon are uncommon (**Figure 2.1.**). These rules governing selective borylation of linear alkanes are easily applied when approaching systems with multiple potential borylation sites containing different types of C–H bonds, but do not translate well when considering methane, which has only one carbon atom at which to borylate.

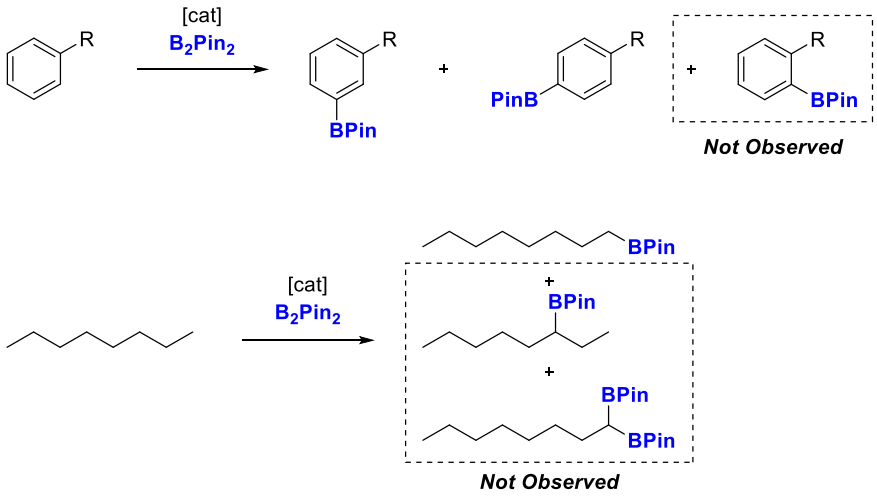

Figure 2.1. Sterically controlled selectivity in C–H borylation reactions.

Our group[9] and that of Minidola[10] recently reported the first examples of the catalytic C–H borylation of methane. Rhodium, iridium, and ruthenium catalysts were studied, and all produced moderate to high yields (45-99% yield) of borylated products. Through these experiments, we found that methane borylation poses some unique selectivity challenges in relation to other borylation reactions, in that we observed significant over-functionalization of the substrate to generate diborylated methane with all catalysts, along with some functionalization of the reaction solvent, cyclohexane (**Figure 2.2.**).

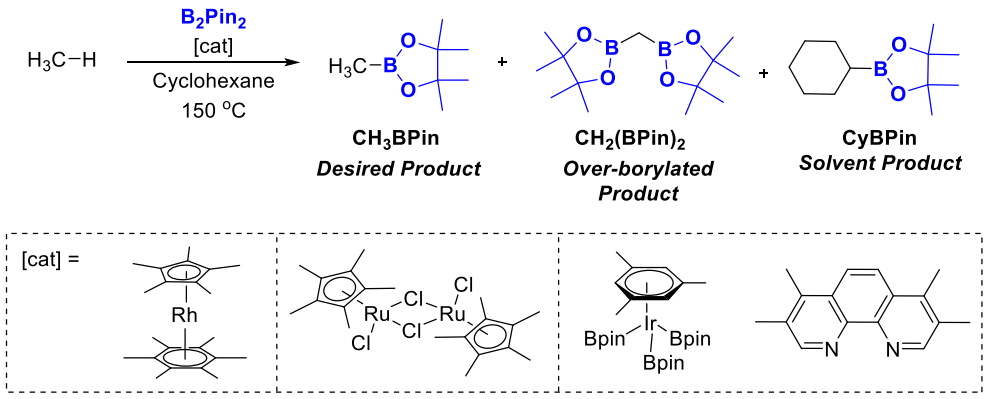

Figure 2.2. Catalysts used and products generated in the report by Sanford and coworkers.

In general, processes that aim to functionalize methane encounter unique challenges. First is the propensity of methane to over-functionalize as functional groups are added to methane. This is likely due to electronic effects from the newly added groups that tend to weaken the remaining C–H bonds, facilitating further functionalization of the methane carbon.[11,12] Also, due to the relative strength of the C–H bonds of methane when compared to other C(sp^3)–H bonds, solvent functionalization is often facile in comparison.

In our borylation systems, the addition of a boryl group to the methane carbon likely activated the remaining C–H bonds to further functionalization, leading to significant amounts of di-borylated product, up to a maximum of 4 : 1 mono- : di-borylated methane in the iridium catalyzed case.[9] In this work, we aim to improve the Rh-catalyzed system, which produced the highest yields of borylated product while remaining moderately selective (99% yield CH_3BPin, 8:1 mono- : di-borylated product), by attempting to selectively mono-borylate methane while avoiding over-borylation (**Figure 2.3.**). While functionalization of the cyclohexane solvent is observed in our systems, the relative amount is generally minimal (59 : 1 methane product : solvent product), so this challenge is not targeted in this Chapter.

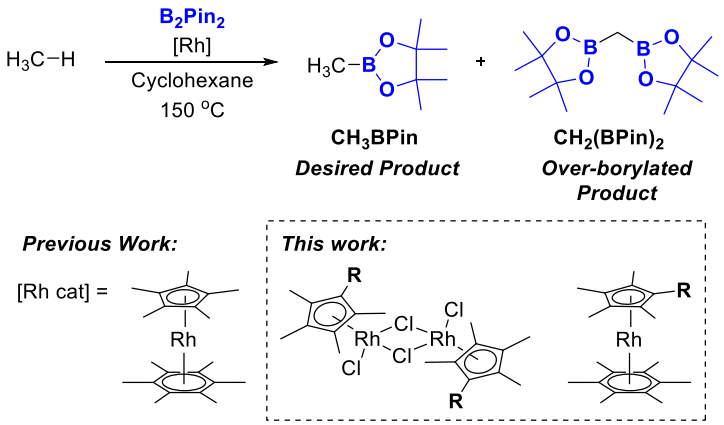

Figure 2.3. Proposed new catalysts for methane borylation.

We hypothesize that the over-functionalization of methane can be minimized through ligand design. In a study by Hall and coworkers, the mechanism of Rh-catalyzed C–H borylation was investigated using a combination of experimentation and calculation, which determined that the C–H activation step of the catalytic cycle is likely rate determining.[13] In our methane borylation system two C–H activations can occur; that of methane, which is small but has strong C–H bonds, or that of CH_3BPin, which is larger but has C–H bonds which are more prone to activation (**Figure 2.4.**). We hypothesize that by increasing the steric bulk of the ligand on our Rh catalyst it could be possible to increase the activation energy for C–H activation of CH_3BPin relative to that of CH_4 by harnessing the steric control normally observed in rhodium-catalyzed C–H borylation reactions. By disfavoring the activation of the bulkier CH_3BPin, we hypothesize that we can more selectively form mono-borylated product.

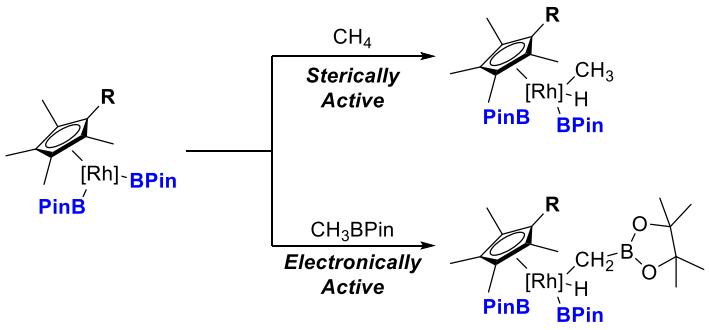

Figure 2.4. Potential C - H activation events in the methane borylation system.

In work previously performed by our group, we found that [Cp*Rh(C_6Me_6)] was the highest yielding catalyst tested, producing 99% yield mono-borylated methane in relation to available B_2Pin_2 with a selectivity of 8:1 mono-borylated : di-borylated methane at its maximal yield.[9] We determined that the optimal ligand on which to adjust the steric bulk here was the Cp* (pentamethylcyclopentadienyl) ligand, as the C_6Me_6 (hexamethylbenzene) ligand on the precatalyst was predicted to dissociate during catalyst activation.[13]

$[Cp^RRhCl_2]_2$ complexes (Cp^R = a substituted cyclopentadienyl ligand), which are also active methane borylation catalysts as well as necessary intermediates to synthesize $[Cp^RRh(C_6Me_6)]$ complexes, are common (pre)catalysts for organic reactions, including C–H alkylation,[14,15] C–H olefination,[16] C–H arylation,[17] C–H borylation,[1,2] alkene carboamination,[18] and related transformations.[19] The Cp* derivative is the most widely used for all of these applications. However, recent reports have shown that complexes bearing substituted cyclopentadienyl ligands exhibit enhanced reactivity and/or selectivity for many transformations.[14,15,18,20] These studies provide a library of Cp^R ligands to study, as well as providing a basis for the development of new Cp^R ligands. As such, the development of efficient, general, and high yielding synthetic routes to $[Cp^RRhCl_2]_2$ complexes are of high interest.

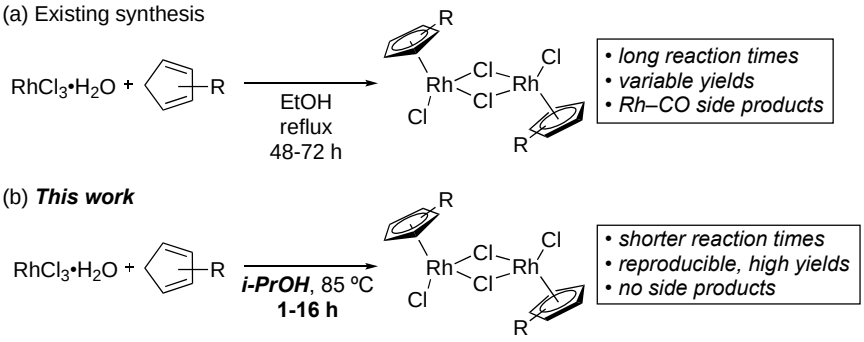

Scheme 2.1. (a) Existing synthetic route to $[Cp^RRhCl_2]_2$. (b) Revised synthetic route to $[Cp^RRhCl_2]_2$

The most common synthesis of $[Cp^RRhCl_2]_2$ involves refluxing a solution of $RhCl_3•H_2O$ and the appropriate cyclopentadiene in methanol or ethanol (**Scheme 2.1.a.**).[21] This procedure requires relatively long reaction times (typically 48-72 h) and often provides variable yields.[22] Furthermore, it can afford significant quantities Rh^I–CO containing side products (*vide infra*).[23] Several recent reports have described shorter syntheses, but these require specialized equipment

such as ball mills[24] or microwave reactors.[25] This work provides a new synthetic method for these compounds, which are critical for use in methane borylation (**Scheme 2.1.b.**).

This chapter describes efforts to develop a new method to synthesize $[Cp^{R}RhCl_2]_2$ complexes to be used in borylation reactions. Next, efforts to tune the selectivity of methane borylation by applying new $Cp^{R}Rh$ catalysts bearing newly designed sterically bulky Cp^{R} ligands are described. Using the data from part two, attempts to improve selectivity in borylation of other $C(sp^3)$–H borylation systems, as well as regioselectivity in (hetero)arene borylation systems are explored.

2.2. Results and Discussion

2.2.1. Synthesis of $[Cp^{R}RhCl_2]_2$ Complexes

We initially targeted the new complex $[Cp^{*3iPr}RhCl_2]_2$ (**1**, Cp^{*3iPr} = 1,3,4-tri-isopropyl-2,5-dimethylcyclopentadienyl) for applications in catalysis. Using the most common literature procedure (reaction of Cp^{*3iPr} with $RhCl_3•H_2O$ in refluxing EtOH for 48 h under N_2), we obtained variable yields of **1** (ranging from 0 to 35%). In addition, ^1H NMR spectroscopic analysis of the crude reaction mixture showed the presence of a major side product **2** in a 1:2 ratio with respect to 1. IR spectroscopic analysis of this mixture showed strong bands at 1979 cm^{-1} and 2050 cm^{-1}, suggesting the presence of a Rh^{I}–carbonyl. X-ray quality crystals of **2** were obtained by vapor diffusion of pentane into a $CHCl_3$ solution of a mixture of **1** and **2**. As shown in **Figure 2.5.**, **2** is the cationic dimer $[(Cp^{*3iPr})_2Rh_2Cl_3]^+$ with $[Rh(CO)_2Cl_2]^-$ as the counteranion (**Figure 2.5.b.**).

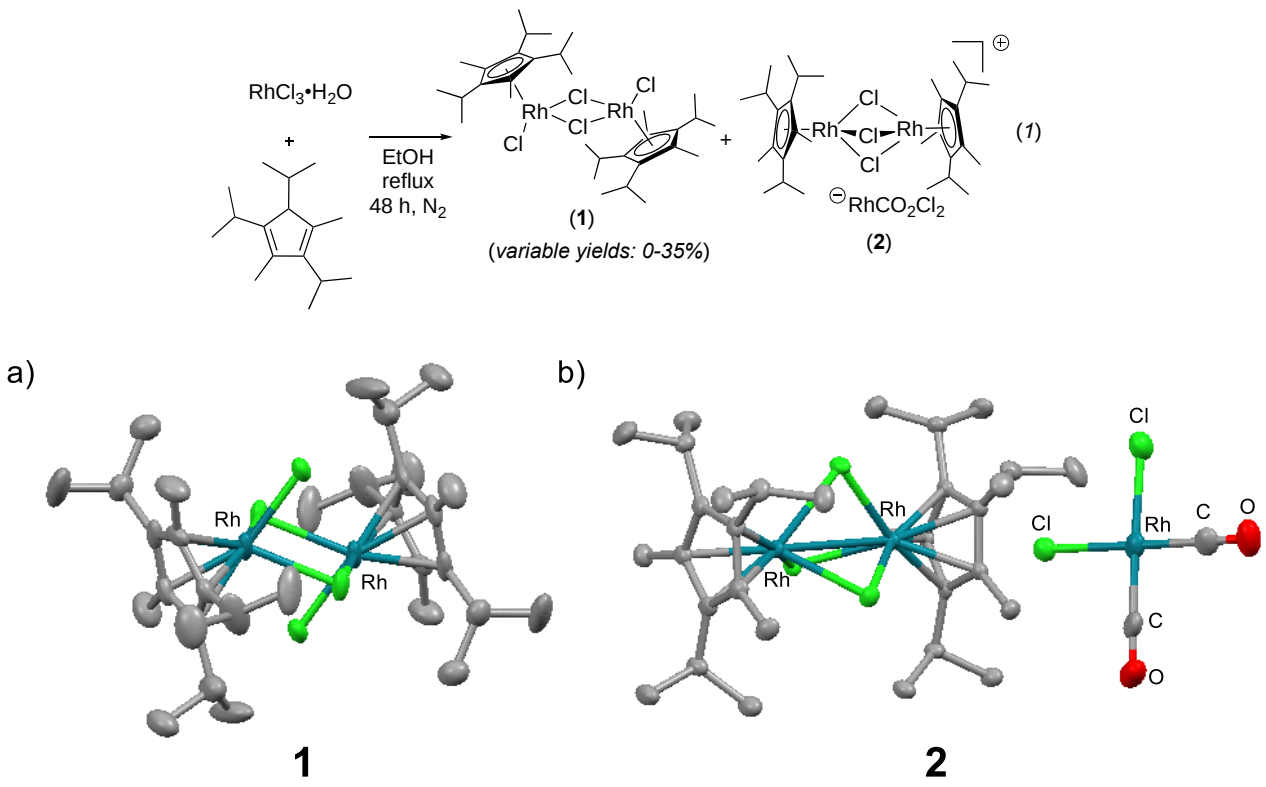

Figure 2.5. X-ray crystal structures of (a) **1** and (b) **2**.

We next examined whether Rh–CO side products are formed during the synthesis of other $[Cp^{R}RhCl_2]_2$ derivatives. Indeed, the analogous reactions of 1-cyclohexyl-2,3,4,5-tetramethylcyclopentadienyl (Cp^{*Cy}) and 1-*tert*-butyl-2,3,4,5-tetramethylcyclopentadienyl (Cp^{*tBu}) with $RhCl_3•H_2O$ in EtOH also show diagnostic IR peaks at ~1980 and 2055 cm^{-1}.

An analogue of **2** was prepared in the literature via the reaction of $RhCl_3•H_2O$ with KCp^{4iPr} (Cp^{4iPr} = tetra-isopropylcyclopentadienyl) in EtOH under an atmosphere of CO.[26] Here, the carbonyl ligand was proposed to originate from the added CO. In the current system, we propose that the carbonyl derives from the EtOH solvent.[27] Rhodium salts are well-known to promote the oxidation of 1º alcohols to aldehydes.[28] Subsequent oxidative addition of acetaldehyde at rhodium(I) and decarbonylation of the resulting metal acyl would then yield the CO ligands observed in **2**.[29] Importantly, this proposed mechanism implicates a simple strategy for preventing

the formation of **2**. Specifically, moving from a 1º to a 2º alcohol solvent should prevent the formation of aldehyde intermediates that are susceptible to decarbonylation.[30]

To test this hypothesis, we conducted the synthesis of $[Cp^{*3iPr}RhCl_2]_2$ in isopropanol. This reaction yielded **1** in 60% isolated yield after just 16 h. The X-ray crystal structure of this complex is shown in **Figure 2.5.a**. As predicted, IR analysis of this product showed no detectable Rh^I–CO peaks. This procedure was applied to a series of $[Cp^RRhCl_2]_2$ derivatives, including Cp^{*Cy}, Cp^{*tBu}, 1-(3,5-di-*tert*-butylphenyl)-2,3,4,5-tetramethylcyclopentadienyl ($Cp^{*dtBuPh}$), and 2,3,4,5-tetramethylcyclopentadienyl (Cp^{4Me}). The reaction times varied based on the Cp ligand, but all were significantly shorter than that required in EtOH (**Table 2.1**). Additionally, this procedure generally afforded comparable or higher yield and significantly less variability in yield compared prior syntheses.[31] In all cases examined, the product precipitated from solution over the course of the reaction and was isolated via filtration and subsequent washing with $CHCl_3$. Another advantage of this procedure is that the reactions are conducted under ambient atmosphere rather than under N_2. IR analysis showed no trace of Rh–CO side-products in any of the products isolated from this procedure.

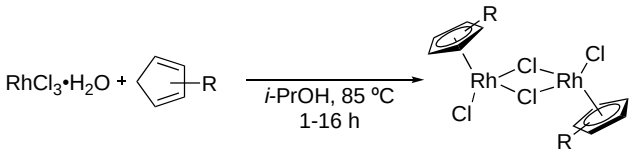

Rh Complex	Isolated yield (this work in ^{i}PrOH) (reaction time)	Isolated yield (*lit* procedure in EtOH) (reaction time)
[Cp*^{3iPr}RhCl$_2$]$_2$	60% (16 h)	0-35% (48-96 h)
[Cp*^{Cy}RhCl$_2$]$_2$	76% (16 h)	76% (48 h)
[Cp*^{tBu}RhCl$_2$]$_2$	53% (16 h)	21-47% (72 h)
[Cp^{4Me}RhCl$_2$]$_2$	79% (16 h)	75% (48 h)[9]
[Cp*^{dtBuPh}RhCl$_2$]$_2$	54% (16 h)	n/a
[Cp*RhCl$_2$]$_2$	75% (1 h)	63-95% (48 h) [31,21]

Table 2.1. Comparison of synthesis of [Cp^{R}RhCl$_2$]$_2$ in *i*-PrOH versus EtOH

2.2.2. Selectivity in Methane Borylation

Previous methane borylation studies revealed that the [Cp*RhCl$_2$]$_2$ performed similarly to the [Cp*Rh(C$_6$Me$_6$)] catalyst in terms of similar selectivity at similar yields of CH$_3$BPin. Due to the newly developed synthetic procedure and high bench stability of [Cp^{R}RhCl$_2$]$_2$, we used the [Cp^{R}RhCl$_2$]$_2$ precatalysts for initial selectivity comparisons. We first synthesized a series of Cp^{R} ligands bearing sequentially bulkier substitutions at a single site on the ring (**Figure 2.6.**). The novel ligand Cp*^{Ph35} was selected rather than the known Cp*^{Ph} to avoid borylation of the aryl ring on the catalyst.

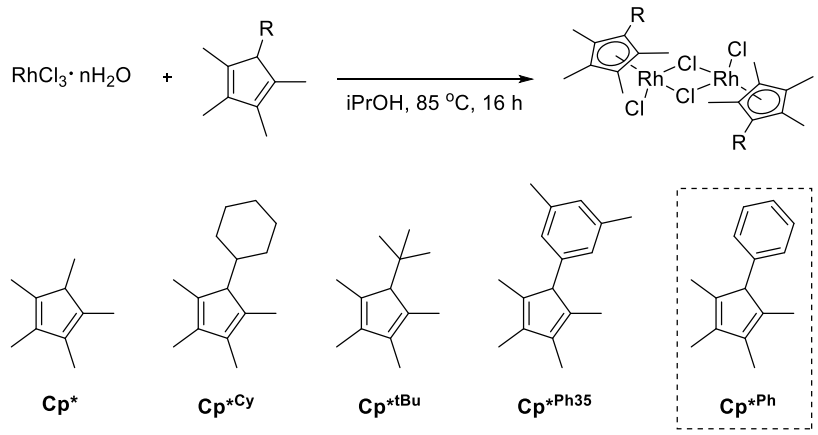

Figure 2.6. Initially synthesized ligand set including Cp*^{Ph} for comparison.

We first conducted time studies for each Rh pre-catalyst in the C–H borylation of methane. Reactions were conducted according to **Scheme 2.2.** using a Parr high-pressure batch reactor equipped with a reactor head designed for removing aliquots of the reaction mixture while simultaneously refreshing the methane pressure. Reactions were carried out at a scale of 2.67 mmol B_2Pin_2 and 35 bar (1.1 M dissolved in cyclohexane) of methane with 2,2,4,6,6-pentamethylheptane as internal standard. Reactions were analyzed by GC-FID.[9] Several early time points are acquired to establish initial activity, followed by later time points to observe long-term efficacy of the catalyst. As shown in **Scheme 2.2.**, the four catalysts show comparable activity, with high activity in the early stages of reaction, slowing at the end. Little activity is observed after 24 h despite observation of remaining B_2Pin_2, likely indicating catalyst deactivation.

Due to rate dependence of di-borylation on the concentration of CH_3BPin, reactions dependent on time rather than the concentration of CH_3BPin do not provide an accurate comparison of selectivity between the catalysts. Therefore, comparisons were made between catalysts at similar concentrations (yields) of CH_3BPin rather than at similar time points in the reaction. In each case, selectivity is compared at an early yield point (~30% yield CH_3BPin) before

we are able to observe significant catalyst decomposition as evidenced through borylation rate suppression (**Table 2.2.**).

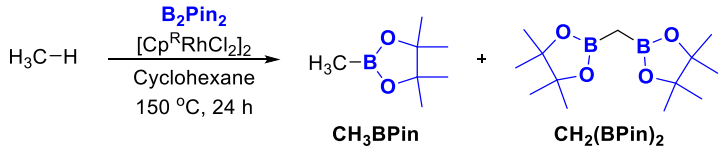

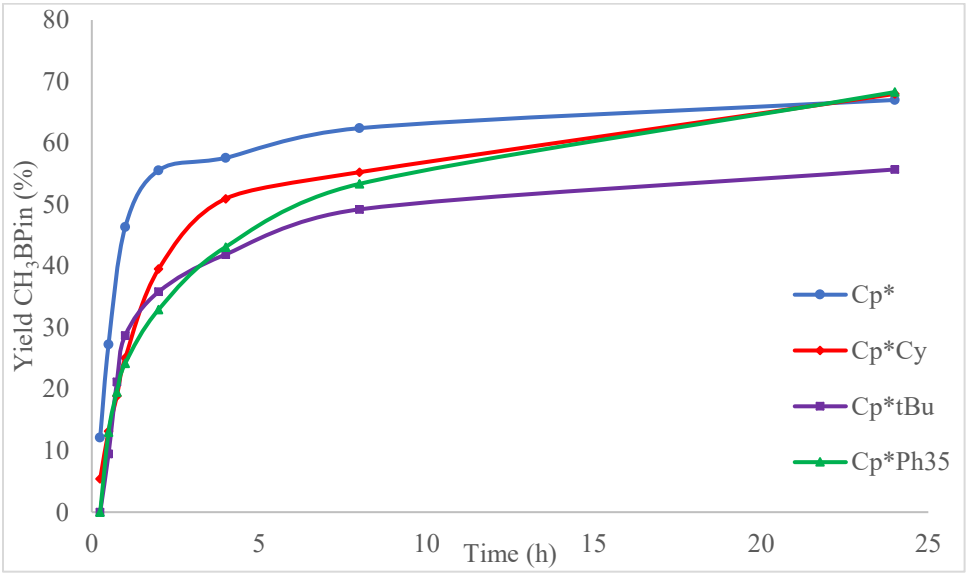

Scheme 2.2. Yield CH_3BPin vs time for methane borylation tested with $[Cp^RRhCl_2]_2$ catalysts.

Entry	Catalyst	Selectivity (CH_3BPin : $CH_2(BPin)_2$)
1	$[Cp^*RhCl_2]_2$	19 : 1
2	$[Cp^{*tBu}RhCl_2]_2$	38 : 1
3	$[Cp^{*Ph35}RhCl_2]_2$	67 : 1
4	$[Cp^{*Cy}RhCl_2]_2$	70 : 1

Table 2.2. $[Cp^RRhCl_2]_2$ catalysts compared by the selectivity of methane borylation at ~30% yield CH_3BPin.

The selectivity of each catalyst was found to be quite different at similar yields of CH_3BPin. At ~30% yield, the ratio of mono- to di-borylated methane was significantly higher in studies with

bulkier catalysts than that of the catalyst bearing Cp* (**Table 2.2.**). The most selective catalysts were those bearing Cp^{*Cy} and Cp^{*Ph35} (**Table 2.2.** entries 3,4). Due to consistent irregularities with the early time points of the studies containing Cp^{*Cy}, we moved forward in our studies using the catalyst $[Cp^{*Ph35}RhCl_2]_2$.

It has been demonstrated in our previous studies that an experimental $\Delta\Delta G^{\ddagger}$, the difference in transition state energies, between the mono- versus diborylation reactions can be approximated by taking the ratio of rate constants between the two processes.[9] Therefore, to further investigate the selectivity differences between $[Cp^*RhCl_2]_2$ and $[Cp^{*Ph35}RhCl_2]_2$, initial rates of CH_3BPin borylation were measured in order to estimate the rate constants of di-borylation for each catalyst (k_{Cp^*} and k_{Cp^*Ph35}) and therefore approximate the $\Delta\Delta G^{\ddagger}$, here the difference in transition state energies between the two catalysts, for di-borylation.

In our examination of the earliest stages of CH_3BPin borylation, we observed significant differences in initial rates between the catalysts, with an over eight-fold higher rate for the smaller Cp* catalyst over the bulkier Cp^{*Ph35} bearing catalyst (**Figure 2.7.**). These reactions were carried out by preparing four individual sealed Schlenk tubes, which were removed from heat at given time points and flash cooled to stop the reaction. Each sample was then analyzed by GC-FID. The data for the catalyst bearing Cp* indicated a significant induction period where di-borylated product is not observed until ten minutes into the reaction. This observed induction period complicates the estimation for k_{Cp^*}, and therefore calculation of a $\Delta\Delta G^{\ddagger}$.

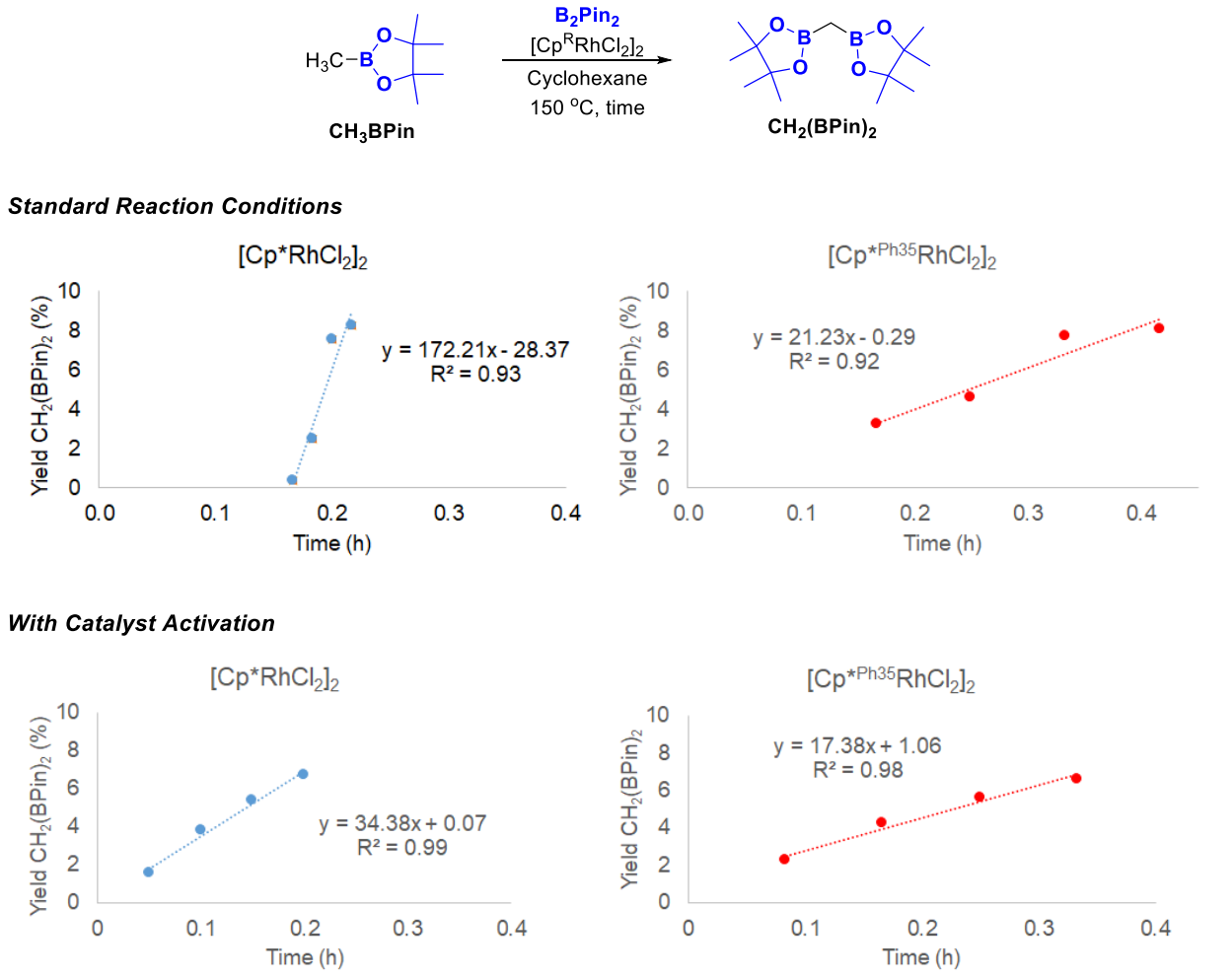

Figure 2.7. Initial rate studies with and without catalyst activation.

In response to the large induction period, we endeavored to measure initial rates after a period of catalyst activation. In the course of the previous initial rate studies, we observed a significant color change accompanying the initial formation of di-borylated product. We were therefore able to identify a likely point at which the active borylation catalyst was generated. A clear pressure tube containing enough precatalyst and B_2Pin_2 for several time points was heated in cyclohexane for 30 minutes, then flash cooled to room temperature to cease reaction. At this time, the tube was returned to the glovebox, where a solution containing CH_3BPin was added. The reaction was then separated into four individual tubes and heated to measure the initial rate, with

the results being analyzed by GC-FID. These reactions yielded a difference in slope of a factor of two between the catalysts, which is a significantly smaller difference than that observed without catalyst activation. Unfortunately, subsequent analysis revealed that a significant degree of catalyst decomposition was occurring during the activation procedure, as the catalyst turned over several times in the undesired borylation of the cyclohexane solvent. Based on this complication, it is most likely that the true difference in rate between the catalysts lies between each of the measured differences in initial rate.

With the knowledge that the increase in steric bulk does influence selectivity in our original time study data, we synthesized [$Cp^{R}Rh(C_6Me_6)$] precatalysts, which are expected to exhibit higher activity and to initiate faster. These were formed by refluxing the $[Cp^{R}RhCl_2]_2$ dimer in trifluoroacetic acid with hexamethylbenzene followed by salt metathesis with NH_4PF_6 to form $[Cp^{R}Rh(C_6Me_6)](PF_6)_2$. This intermediate was then reduced under inert atmosphere with cobaltocene to give [$Cp^{R}Rh(C_6Me_6)$].[32] Methane borylation time studies were carried out under similar conditions to those applied in our studies with the $[Cp^{R}RhCl_2]_2$ precatalysts using the same concentration of rhodium in solution. Here we observe that [$Cp^{*Ph35}Rh(C_6Me_6)$] is considerably more active for methane borylation than its Cp* counterpart, but that the overborylation selectivity differences discussed above are not observed (**Scheme 2.3.**). We observe similar selectivities at ~30% yield; both yielding ~30:1 mono-:di-borylated product (**Table 2.3.**).

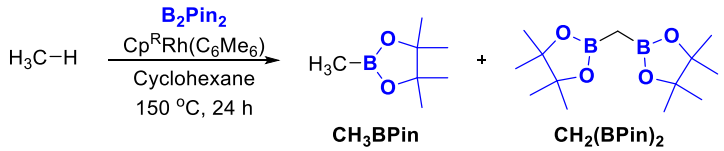

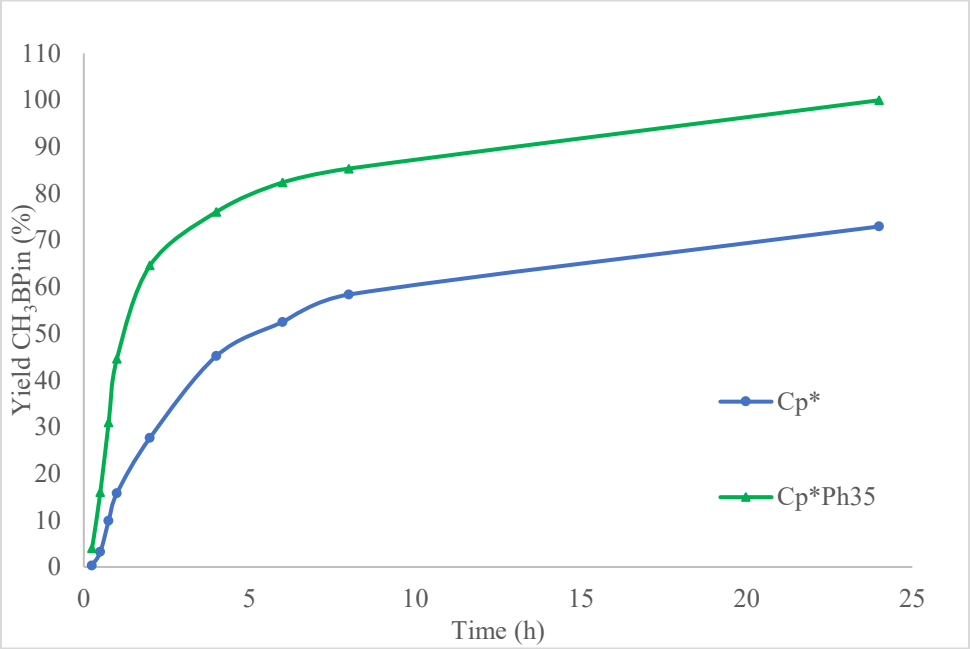

Scheme 2.3. Methane borylation time studies for [Cp^{R}Rh(C$_6$Me$_6$)]

Entry	Catalyst	Selectivity (CH_3BPin : $CH_2(BPin)_2$)
1	[Cp*Rh(C$_6$Me$_6$)]	30 : 1
2	[Cp*^{Ph35}Rh(C$_6$Me$_6$)]	34 : 1

Table 2.3. [Cp^{R}Rh(C$_6$Me$_6$)] catalysts compared by the selectivity of methane borylation at ~30% yield CH_3BPin.

2.2.3. Computational Investigation of Selectivity

In an effort to better understand the origins of mono-borylation selectivity, a computational study has been performed to determine possible effects of increasing the steric bulk on a single

site of the Cp ring on the activation energy for the C–H activation of methane and CH_3BPin. These C–H activation elementary steps are expected to be rate-determining in methane borylation, as proposed by Hall and coworkers.[13] Our model structures for these reactions are derived from those original calculations, which predicted two potential starting structures from two reaction pathways for CpRh-catalyzed C–H borylation. In both reaction pathways, C–H activation was calculated to be the rate-determining step. We derivatized structure (**X**), which we predicted to be the most relevant to our reaction conditions, varying one site on the cyclopentadienyl ring to model the new Cp^{*Ph35} ligand.

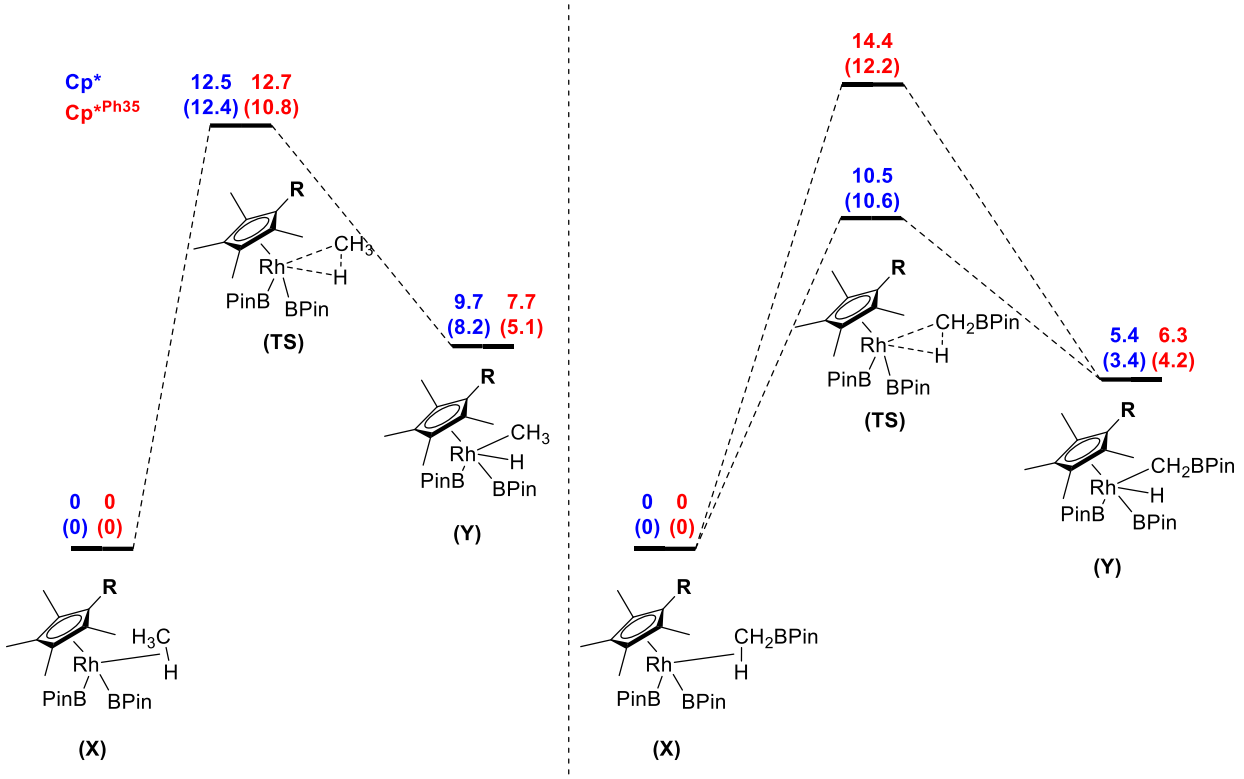

Figure 2.8. C–H Activation pathways calculated for both Cp* and Cp^{*Ph35}. Energies displayed in kcal/mol and listed as ΔG (ΔH).

DFT calculations were performed for the full reaction path utilizing both Cp* and Cp^{*Ph35} for borylation of CH_4 and CH_3BPin. Structures were optimized using B3LYP functional[33,34] and

LANL2DZ basis set [35,36,37] using the Q-Chem 5.0 software package.[38] Frequency calculations were carried out with B3LYP/LANL2DZ ensuring the correct number of imaginary frequencies. Growing string method was employed to determine minimum energy reaction pathways.[39,40,41]

Comparison of the C–H activation steps for CH_4 yielded a $\Delta\Delta G^{\ddagger}$ of 0.2 kcal between each catalyst (**Figure 2.8.**). This difference is very small and implies that the C–H activation step for methane borylation is not significantly altered by increased steric bulk on the Cp ligand. This result is reflected in our experimental data, where the mono-borylation of methane proceeded at comparable rates when the Cp^{*Ph35} catalyst was used.

Comparison of the C–H activation steps for CH_3BPin on the other hand yielded a $\Delta\Delta G^{\ddagger}$ of 4.0 kcal/mol with a higher $\Delta G^{\ddagger}$ for Cp^{*Ph35} (**Figure 2.8.**). This difference is significantly larger and implies steric interference is affecting the C–H activation step. Critically, our calculations place the bulky group of the ligand squarely in the field of approach for CH_3Bpin to maximize the potential observed effect of sterics on the approach and C–H activation of the substrate (**Figure 2.9.a.**). These calculations do not account for the ability of the Cp^{R} ring to rotate out of the vector of approach for the substrate, meaning the actual barrier changes induced by steric bulk of the ligand is likely considerably lower (**Figure 2.9.b.**). This effect is described by Rovis and coworkers, where they explain that the determining Tolman cone angle for a Cp ring assumes that due to free ring rotation, each substitution occupies a position only 20% of the time.[22] This implies that for a Cp^{*R} ring with only one change from the C_5Me_5 scaffold, the ring will still be sterically similar to a standard Cp* ring.

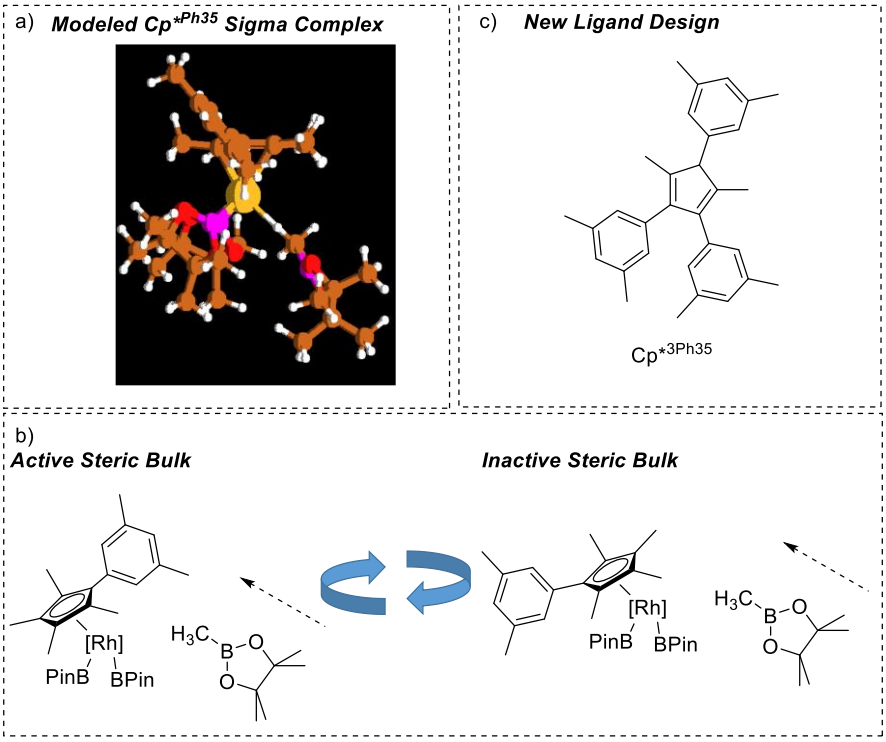

Figure 2.9. a) C–H sigma complex [Cp^{R}Rh(BPin)$_2$(CH$_3$BPin)] modeled using DFT. Model displays bulky aryl group pointing out-of-plane. b) Illustration of potential rotation effects on effects of steric bulk. c) Newly designed Cp^{R} derivative Cp*^{3Ph35} designed to mitigate potential rotation effects.

2.2.4. Design of a New Cp Ligand for Selective Methane Borylation

In an attempt to mitigate the effects of free ring rotation on overall relative Tolman cone angle, a new Cp^{R} derivative was synthesized to further increase the steric bulk of the ligand system. We hypothesized that if one bulky group was occupying a position in space around the rhodium center 20% of the time, we would observe a larger effect if we instead used three identical bulky groups, which would then increase the occupancy of a given site to 60%. Cp*^{3Ph35} (1,3,4-tri(3,5-dimethylphenyl)-2,5-dimethylcyclopentadienyl) was synthesized by similar methods to other bulky Cp^{R} rings, then metalated using an accelerated metalation method (**Figure 2.9.c.**).[25] When

[Cp*^{3Ph35}Rh(C_6Me_6)] was compared to the other catalysts through a methane borylation time study (**Scheme 2.4.**), the new complex indeed showed significantly higher selectivity (75 : 1 mono- : di-borylated methane) at comparable conversion CH_3BPin (**Table 2.4.** entry 3). This new catalyst was, however, less active for methane borylation than similar catalysts, likely due to the stark increase in steric bulk around the rhodium center.

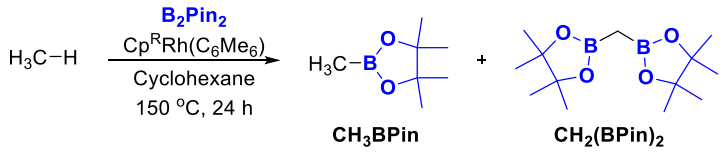

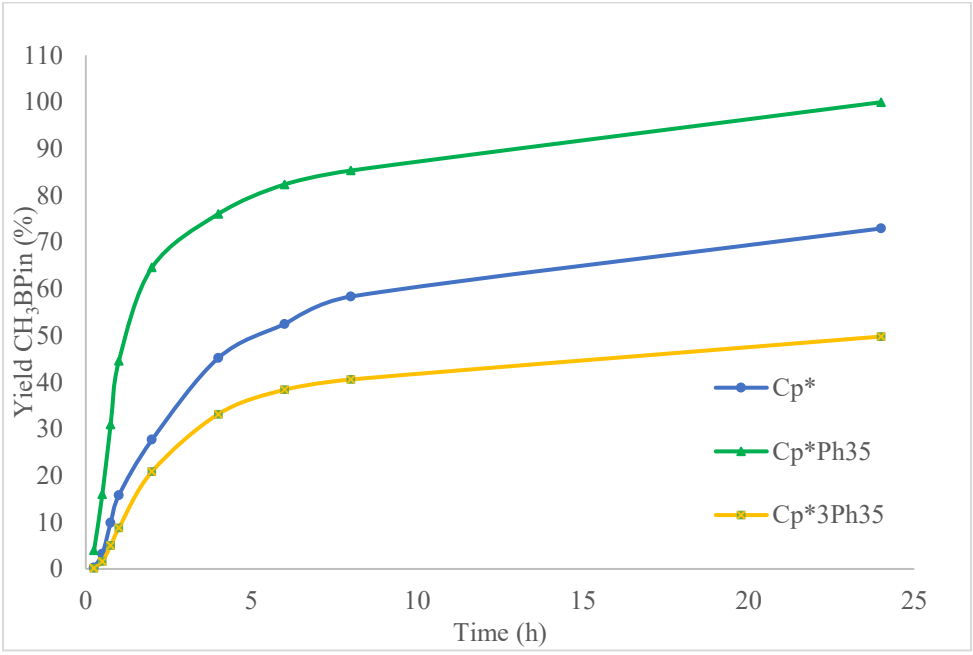

Scheme 2.4. Methane borylation time studies for [Cp^{R}Rh(C_6Me_6)] including [Cp*^{3Ph35}Rh(C_6Me_6)].

Entry	Catalyst	Selectivity (CH_3BPin : $CH_2(BPin)_2$)
1	[Cp*Rh(C_6Me_6)]	30 : 1
2	[Cp*^{Ph35}Rh(C_6Me_6)]	34 : 1
3	[Cp*^{3Ph35}Rh(C_6Me_6)]	75 : 1

Table 2.4. [Cp^{R}Rh(C_6Me_6)] catalysts compared by the selectivity of methane borylation at ~30% yield CH_3BPin including [Cp*^{3Ph35}Rh(C_6Me_6)].

2.2.5. Selectivity for Methane over Linear Hydrocarbons

We hypothesized that effects on selectivity similar to those observed in the pure methane system could be observed regarding selectivity between methane and larger hydrocarbons. First, we assessed changes in selectivity between methane and ethane in a mixed gas system. Competition experiments between methane and ethane were originally carried out in our previous study, where different metal catalysts were compared for their selectivity for methane over ethane.[9] Here we aimed to evaluate [Cp^{R}RhCl$_2$]$_2$ catalysts bearing Cp^R ligands of varying steric bulk for their selectivity for methane over ethane. Reactions were run in cyclohexane at a loading of 0.89 mmol B_2Pin_2 and 3 mol% Rh in a Parr vessel equipped with an analog pressure gauge and heated to 150 °C for 14 h. To accurately evaluate the quantity of gas being added for each reaction, the gases were added sequentially with the mass being noted in between loadings of ethane and methane to determine the molar amount of gas loaded. Reactions were cooled, then analyzed by GC-FID. After evaluating a series of [Cp^{R}RhCl$_2$]$_2$ catalysts, all catalysts showed a preference for methane over ethane, and only minor effects from increased steric bulk were observed between catalysts when compared to [Cp*RhCl$_2$]$_2$ (**Table 2.5.**). In all cases over-borylation of methane was observed while over-borylated ethane was not observed.

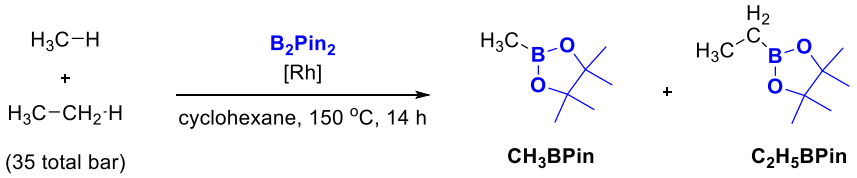

Rh Dimer Complex	Ratio of Products (Methane : Ethane)	Yield % (Methane : Ethane)	Yield % (Mono- : Di-borylated methane)
$[Cp^{4Me}RhCl_2]_2$	1.9 : 1	13 : 6.7	12 : 0.5
$[Cp^*RhCl_2]_2$	2.0 : 1	31 : 15	30 : 1.4
$[Cp^{*2Et}RhCl_2]_2$	2.4 : 1	33 : 14	32 : 1.3
$[Cp^{*Cy}RhCl_2]_2$	2.8 : 1	44 : 16	42 : 2.1

Table 2.5. Yields CH_3BPin and CH_3CH_2BPin in competition experiments.

Next, we sought to assess selectivity in a mixed methane and *n*-hexane system. We hypothesized that the steric difference between methane and ethane were too small, and that a larger linear hydrocarbon might produce starker differences in selectivity between catalysts of varying steric bulk. Reactions were run in neat *n*-hexane at a loading of 0.89 mmol B_2Pin_2 and 3% Rh in a standard Parr vessel heated to 150 °C for 14 h. A series of $[Cp^RRhCl_2]_2$ catalysts all showed a preference for hexane over methane, and only minor effects from increased steric bulk were observed between catalysts when compared to $[Cp^*RhCl_2]_2$. The preference for hexane borylation is likely due to the higher concentration of this hydrocarbon in solution (rather than an inherent preference for hexane C–H activation). In all cases over-borylation of methane was observed while over-borylated hexane was not observed (**Table 2.6.**).

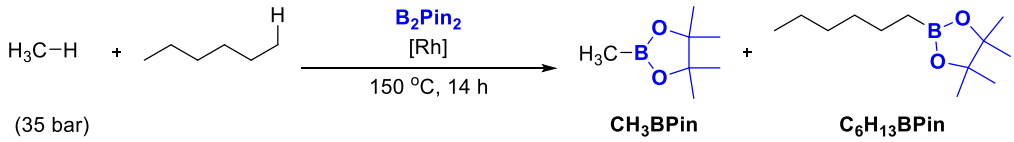

Rh Dimer Complex	Ratio of Products (Methane : Hexane)	Yield % (Methane : Hexane)	Yield % (Mono- : Di-borylated methane)
$[Cp^{4Me}RhCl_2]_2$	1.0 : 1.9	14 : 26	14 : 0.6
$[Cp^*RhCl_2]_2$	1.0 : 1.8	26 : 47	26 : 1.1
$[Cp^{*2Et}RhCl_2]_2$	1.0 : 1.7	27 : 45	27 : 0.9
$[Cp^{*Cy}RhCl_2]_2$	1.0 : 1.5	36 : 54	36 : 1.2

Table 2.6. Yields CH_3BPin and *n*-HexBPin in competition experiments.

2.2.6. Site Selectivity in the Borylation of (Hetero)arenes

We hypothesized that similar steric principles used to guide selectivity in the methane borylation system could also be applied to regioselectivity in arene borylation systems. We first applied a series of $[Cp^RRhCl_2]_2$ catalysts to 1,4-disubstituted arenes in an effort to shift borylation from *ortho*- to an electronically activating group to *ortho*- to a less sterically hindered group. We targeted aryl fluorides to provide a group with very little bulk that does not deactivate the ring. If steric principles applied, borylation should occur at the more electronically active position unless encountering a sterically bulky group, in which case borylation would shift adjacent to the fluorine. However, in our tests, borylation occurred *ortho*- to the fluorine regardless of substitution *para*- to the fluorine and regardless of substitution on the Cp^R ligand (**Figure 2.10.**).

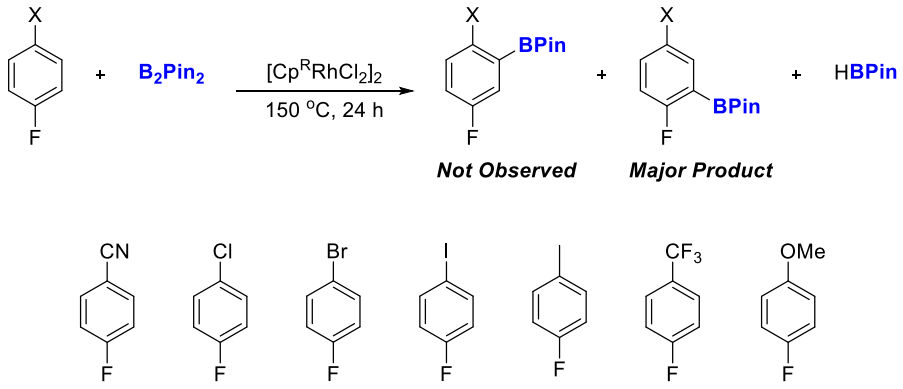

Figure 2.10. 1,4-disubstituted arenes used for C–H borylation.

We next aimed to evaluate regioselectivity in the borylation of N-alkyl pyrroles. We hypothesized that while N-alkylpyrroles are electronically activated at the 2-position, steric interference between an N-alkyl group and a bulky Cp^R ligand could force borylation to shift to the less hindered 3-position. N-methylpyrrole was evaluated first, and we found that although there are small effects observable in selectivity with catalysts of different steric bulk, the effects were relatively minor (**Table 2.7.**). Applying these principles to the bulkier N-ethylpyrrole, we hypothesized that a larger effect should be observed than for the methyl derivative. Upon testing, almost no effect was observed on selectivity by changing bulk on the Cp^R ligand, contrary to our hypothesis (**Table 2.8.**).

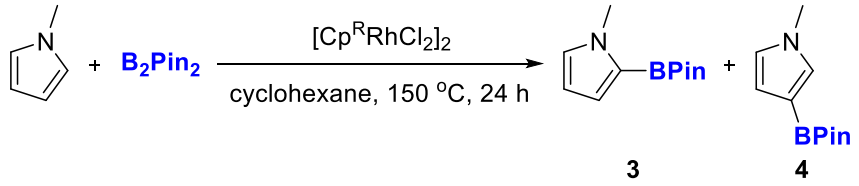

Rh Dimer Complex	Ratio of Products (3 : 4)
$[Cp^{4Me}RhCl_2]_2$	2.5 : 1
$[Cp^*RhCl_2]_2$	2.4 : 1
$[Cp^{*Cy}RhCl_2]_2$	1.9 : 1
$[Cp^{*2Et}RhCl_2]_2$	1.4 : 1

Table 2.7. Ratio of products from N-methylpyrrole borylation reactions.

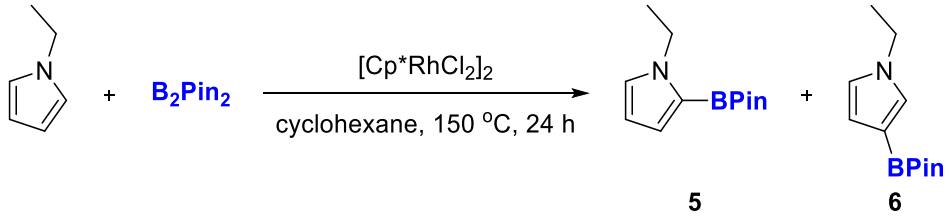

Rh Dimer Complex	Ratio of Products (5 : 6)
$[Cp^{4Me}RhCl_2]_2$	1 : 1.3
$[Cp^{*Cy}RhCl_2]_2$	1 : 1.3
$[Cp^*RhCl_2]_2$	1 : 1.4
$[Cp^{*Ph35}RhCl_2]_2$	1 : 1.5

Table 2.8. Ratio of products from N-ethylpyrrole borylation reactions.

In an attempt to probe the origin of this effect, we next tested the effect of ligand on the borylation of furan, which is unsubstituted on the heteroatom. Here we expected to see the majority of borylation at the 2-position and to observe no effects from large substituents on the Cp^R ligand. Contrary to this hypothesis, we saw significant selectivity changes with the larger Cp^R ligands.

This implies that an effect outside of sterics may be driving selectivity changes rather than direct interaction between the ligand and a large substituent on the substrate (**Table 2.9.**).

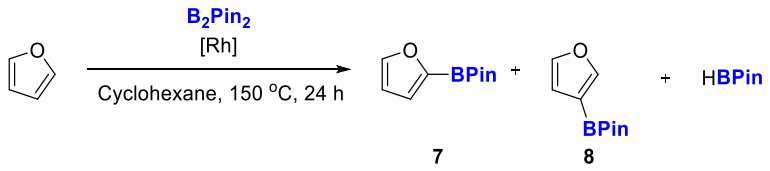

Rh Dimer Complex	Ratio of Products (7 : 8)
$[Cp^{*Ph35}RhCl_2]_2$	6.3 : 1
$[Cp^{*Cy}RhCl_2]_2$	7.3 : 1
$[Cp^{*}RhCl_2]_2$	10.4 : 1
$[Cp^{4Me}RhCl_2]_2$	11.4 : 1

Table 2.9. Ratio of products from furan borylation reactions.

2.3. Conclusions and Outlook

This chapter describes an improved synthesis of $[Cp^{R}RhCl_2]_2$ complexes. A simple solvent switch from the 1º alcohol ethanol to the 2º alcohol isopropanol eliminates the formation of Rh-carbonyl containing side products, while accelerating the reactions and often enhancing yields. Overall, we anticipate that this method will prove broadly useful for the synthesis of both known and new $[Cp^{R}RhCl_2]_2$ derivatives.

This chapter also describes the development of new $Cp^{R}Rh$ catalysts that are found to improve the selectivity of the C–H borylation of methane. These new catalysts are evaluated through both experimentation and DFT analysis. By varying the Cp ligand substitution, we were

able to increase the ratio of mono-borylated product to over-borylated product (up to 75 : 1 ratio), making the reaction overall more selective for mono-borylated product through the increase of steric bulk around the rhodium center. These catalysts were not found to have a similar effect on the selectivity of alkane competition reactions or on C(sp^2)–H borylation reactions. Further study in this field could aim to develop new bulky ligands that do not hinder reactivity in the rhodium system, or to focus on other methane C–H borylation catalysts to determine new ligands to enhance their selectivity. Additionally, it could be of interest to investigate the mechanistic differences between C–H borylation with $[Cp^RRhCl_2]_2$ and $[Cp^RRh(C_6Me_6)]$ precatalysts, as our experimental results indicate that the active catalyst produced using these two complexes are likely different.

2.4. Experimental Procedures and Characterization of Compounds

2.4.1. General Experimental

NMR spectra were recorded at room temperature on a Varian vnmrs 700 (699.76 MHz for ^1H) NMR spectrometer with the residual solvent peak ($CDCl_3$: ^1H: δ = 7.26 ppm or C_6D_6: ^1H: δ=7.16 ppm) as the internal reference. Chemical shifts are reported in parts per million (ppm, δ) relative to tetramethylsilane as an external reference at 0.00 ppm. Multiplicities are reported as follows: s (singlet), d (doublet), t (triplet), q (quartet), hept (heptet), m (multiplet). Coupling constants (*J*) are reported in Hz. Yields of complexes were determined by isolation and concentrations of product in crude reaction mixtures were determined by ^1H NMR. Yields for standard borylation reactions were determined by GC-FID using chlorobenzene as standard.

Yields for methane borylation time study reactions were determined by GC-FID using 2,2,4,6,6-pentamethylheptane as internal standard.

Cp^{*Cy}, Cp^{*tBu}, and Cp^{*2Et} were synthesized according to literature methods.[42,43,44] Cp^{*Ph35} was synthesized by an adapted literature method.[45] Cp^{*3iPr} and Cp^{*3Ph35} was synthesized by an adapted literature method.[45,46] [Cp*Rh(C_6Me_6)] was synthesized according to literature methods.[32] $[Cp^{3*Ph35}RhCl_2]_2$ was synthesized by an adapted literature procedure.[25] All commercial reagents and solvents were used as received. 1,2,3,4,5-Pentamethylcyclopentadiene (Cp*H), 2-ethylboronic acid pinacol ester, N-ethylpyrrole, and 2,2,4,6,6-pentamethylheptane were purchased from TCI America. 3,5-dimethylbenzaldehyde was purchased from AOBchem. (2,3,4,5)-Tetramethylcyclopent-2-enone and methyl boronic acid pinacol ester were purchased from Ark Pharm. Formic acid was purchased from EM Science. Lithium chloride was purchased from J.T. Baker Co. $CDCl_3$ and C_6D_6 were purchased from Cambridge Isotope Laboratories. Hydrochloric acid was purchased from Millipore. Cyclohexyl magnesium chloride (2 M in diethyl ether), *tert*-butyl lithium (1.7 M in pentane), isopropyl magnesium chloride lithium chloride complex (1.3 M in THF), 3-pentanone, cyclohexane, 4-fluoroiodobenzene, N-methylpyrrole-2-boronic acid pinacol ester, and isopropyl magnesium chloride (2 M in THF) were purchased from Aldrich. Isobutyraldehyde, ethyl magnesium bromide (3 M in in diethyl ether), hexamethylbenzene, chlorobenzene, 5-iodo-m-xylene, 1,5-cyclooctadiene, 4-fluoroanisole, N-methylpyrrole, and *n*-hexane were purchased from Acros. Ammonium hexafluorophosphate and 4-fluorotoluene were purchased from Matrix Scientific. Phosphorous pentoxide (P_2O_5) and furan-2-boronic acid pinacol ester were purchased from Alfa Aesar. Trifluoroacetic acid, 4-fluorobenzonitrile, 4-chlorofluorobenzene, 4-fluorobenzotrifluoride, and bis(pinacolato) diboron were purchased from Oakwood. 4-bromofluorobenzene was purchased from Apollo Scientific. Methane (ultra-high

purity) and ethane (99.0%) were purchased from Metro Welding/Cryogenic Gases. Ethanol (EtOH) was purchased from Koptec. Sulfuric acid and chloroform were purchased from BDH. Dichloromethane (DCM), 2-propanol (iPA), ethyl acetate (EtOAc), hexanes, sodium bicarbonate, sodium carbonate, sodium sulfate, phosphoric acid, and potassium hydroxide were purchased from Fisher Scientific. $RhCl_3•XH_2O$, lead(IV) oxide, and cobaltocene were purchased from Strem Chemicals, Inc. Methanol (MeOH) was purchased from VWR International. Diethyl ether (Et_2O) and pentane were purchased from Fisher Scientific and either used as received (stabilized) or purified by an Innovative Technologies solvent purification system consisting of a copper catalyst, activated alumina, and molecular sieves (see details below for which was used). Tetrahydrofuran (THF) was purchased from VWR International and purified by an Innovative Technologies solvent purification system consisting of a copper catalyst, activated alumina, and molecular sieves.

2.4.2. Experimental Procedures – Synthesis of Complexes

General Synthesis of $[Cp^RRhCl_2]_2$ in Ethanol

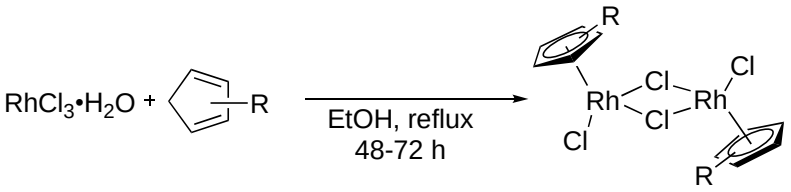

$RhCl_3•H_2O$ (38% Rh, 0.150 g, 0.55 mmol, 1 equiv) was added to a 10 mL two-neck flask containing a stir bar. The flask was fitted with a reflux condenser and a rubber septum then cycled with vacuum and N_2 (x 3). Ethanol (3 mL) added to the flask, and the resulting mixture was stirred until the solution became deep red (~1 min). Cp^R (0.69 mmol, 1.2 equiv) was added to this stirring solution followed by 3 drops of water. The resulting mixture was heated at reflux for 48-72 h,

during which time a precipitate was observed. The reaction was allowed to cool to room temperature, and then the flask placed in a freezer (–20 °C) for several hours, during which time additional precipitate formed. The solid was collected by filtration and washed with cold ethanol (2 x 5 mL) and pentane (4 x 5 mL). The solid was then dissolved in $CHCl_3$ (4 x 10 mL), and the solvent was removed under vacuum. The resulting solid was washed with diethyl ether (3 x 10 mL). Additional diethyl ether (3 x 15 mL) was added and then evaporated slowly under a stream of nitrogen to remove residual $CHCl_3$ from the solid. The solid was dried *in vacuo* overnight at 40 ºC to yield the product (typically as a mixture with the Rh–CO side product) as a red to orange solid.

X-ray quality crystals of $[(Cp^{*3iPr}RhCl_3)_2^+ Rh(CO)_2Cl_2^-]$ (**2**) were obtained by vapor diffusion of pentane into a chloroform solution of a mixture of **1** and **2**.

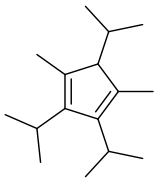

Cp^{*3iPr}

1974 cm^{-1}
2054 cm^{-1}

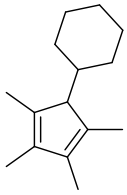

Cp^{*Cy}

1985 cm^{-1}
2057 cm^{-1}

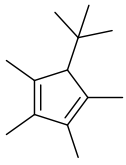

Cp^{*tBu}

1979 cm^{-1}
2055 cm^{-1}

Compound	**Reaction Yield in EtOH**	**CO stretch (cm^{-1})**
$[Cp^{*3iPr}RhCl_2]_2$	0-35%	1974, 2054
$[Cp^{*Cy}RhCl_2]_2$	76%	1985, 2057
$[Cp^{*tBu}RhCl_2]_2$	21-47%	1979, 2055

Table 2.10. Reaction yields in EtOH (products typically isolated as a mixture of $(Cp^{R}RhCl_2)_2$ and a CO-containing impurity that we assign as $[(Cp^{R}RhCl_3)_2^{+}\ Rh(CO)_2Cl_2^{-}]$) and the associated Rh–CO stretches

Figure 2.11. FTIR spectrum of isolated product from synthesis of $[Cp^{*3iPr}RhCl_2]_2$ in EtOH

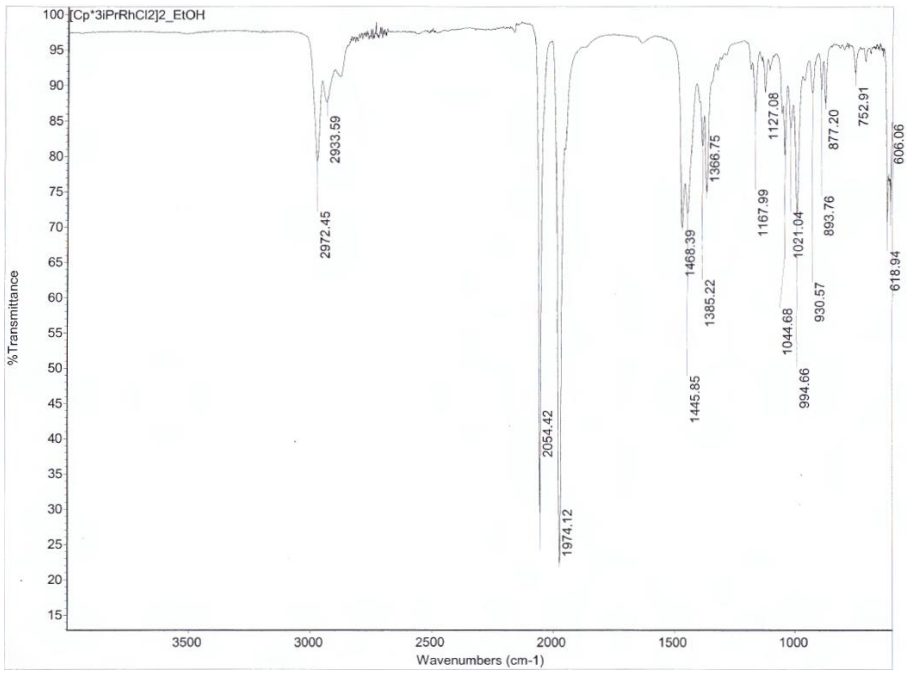

Figure 2.12. FTIR spectrum of isolated product from synthesis of $[Cp^{*Cy}RhCl_2]_2$ in EtOH

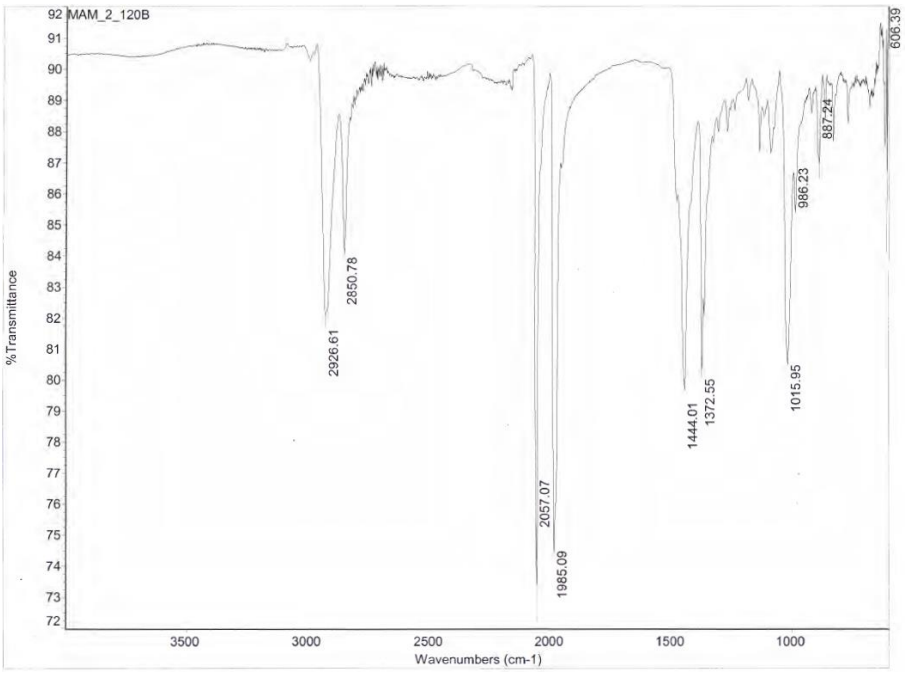

Figure 2.13. FTIR spectrum of isolated product from synthesis of $[Cp^{*tBu}RhCl_2]_2$ in EtOH

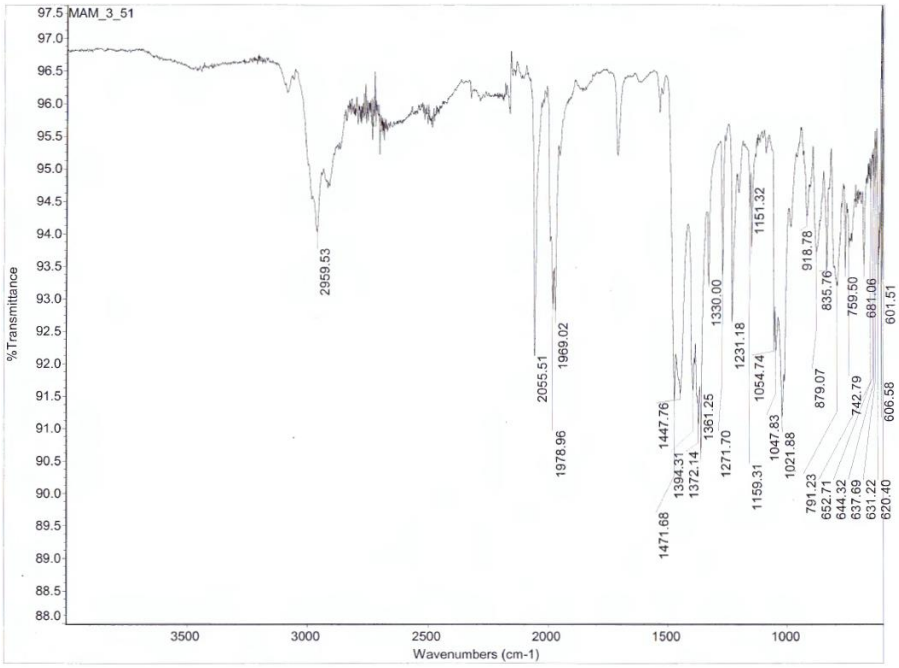

General Synthesis of $[Cp^{R}RhCl_2]_2$ in Isopropanol

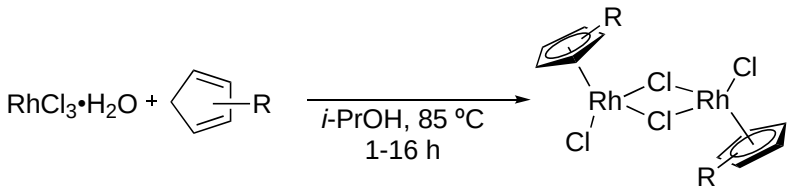

Under ambient atmosphere, $RhCl_3•H_2O$ (38% Rh, 0.150 g, 0.55 mmol, 1 equiv) was added to a 20 mL scintillation vial containing a stir bar. Isopropanol (iPrOH) (3 mL) added to vial, and the resulting mixture was stirred until the solution became deep red (~2 min). Cp^{R} (0.69 mmol, 1.2 equiv) was added to this stirring solution followed by 3 drops of water. The vial was sealed with a Teflon-lined cap, and the resulting mixture was heated at 85 ºC for 1-6 h, during which time a precipitate formed. The reaction was allowed to cool to room temperature, and then the vial placed in a freezer (–20 °C) for several hours, during which time additional precipitate formed. The solid was collected by filtration and washed with cold isopropanol (2 x 5 mL) and pentane (4 x 5 mL). The solid was then dissolved in $CHCl_3$ (4 x 10 mL), and the solvent was removed under vacuum. The resulting solid was washed with diethyl ether (3 x 10 mL). Additional diethyl ether (3 x 15 mL) was added and then evaporated slowly under a stream of nitrogen to remove residual $CHCl_3$ from solid. The solid was dried *in vacuo* overnight at 40 ºC to yield a red to orange solid.

X-ray quality crystals of $[Cp^{*3iPr}RhCl_2]_2$ and $[Cp^{*Ph35}RhCl_2]_2$ were obtained by slow growth in minimal cold (–20 °C) chloroform.

[Cp*^{3iPr}RhCl$_2$]$_2$

Reaction time: 16 h in iPrOH. Product obtained as a red-orange solid (0.1345 g, 60% yield).

^{1}H NMR (700 MHz, $CDCl_3$): δ 2.96 (hept, *J* = 7.2 Hz, 2H), 2.61 (hept, *J* = 7.2 Hz, 1H), 1.82 (s, 3H), 1.48 (d, *J* = 7.1 Hz, 3H), 1.33 (d, *J* = 7.2 Hz, 3H), 1.29 (d, *J* = 7.1 Hz, 3H).

^{13}C NMR (176 MHz, $CDCl_3$): δ 100.98, 99.72 (d, *J* = 7.9 Hz), 94.82, 25.00, 24.56, 22.09, 20.61, 20.44, 11.43.

Anal. Calc. for $C_{32}H_{54}Cl_4Rh_2$: C, 48.88, H, 6.92; Found: C, 49.01, H, 6.82.

[Cp*^{Cy}RhCl$_2$]$_2$

Reaction time: 16 h in iPrOH. Product obtained as a red-orange solid (0.1576 g, 76% yield).

^{1}H NMR (700 MHz, $CDCl_3$) δ 2.17 (t, *J* = 12.5 Hz, 1H), 2.00 (d, *J* = 12.5 Hz, 2H), 1.78 (d, *J* = 13.4 Hz, 2H), 1.72 (s, 6H), 1.69 (bs, 1H), 1.60 (s, 6H), 1.40 (q, *J* = 12.5 Hz, 2H), 1.31 (q, *J* = 13.4 Hz, 2H), 1.15 (m, 1H).

^{13}C NMR (176 MHz, $CDCl_3$) δ 97.91 (d, *J* = 8.3 Hz), 94.04 (d, *J* = 8.6 Hz), 93.81 (d, *J* = 9.7 Hz), 35.43, 30.80, 26.87, 26.16, 10.81, 9.69.

Anal. Calc. for $C_{30}H_{46}Cl_4Rh_2$: C, 47.77, H, 6.15; Found: C, 47.68, H, 6.21.

[Cp*^{tBu}RhCl$_2$]$_2$

Reaction time: 16 h in iPrOH. Product obtained as a red-orange solid (0.1024 g, 53% yield).

^{1}H NMR (700 MHz, $CDCl_3$) δ 1.86 (s, 6H), 1.62 (s, 6H), 1.42 (s, 9H).

^{13}C NMR (176 MHz, $CDCl_3$) δ 99.13 (d, J = 8.7 Hz), 95.02 (d, J = 9.0 Hz), 94.58 (d, J = 9.9 Hz), 33.49, 30.80, 13.31, 9.85.

Anal. Calc. for $C_{26}H_{42}Cl_4Rh_2$: C, 44.47, H, 6.03; Found: C, 44.81, H, 6.08.

[Cp^{4Me}RhCl$_2$]$_2$

Reaction time: 16 h in iPrOH. Product obtained as a red-orange solid (0.1331g, 79% yield).

^{1}H NMR (500 MHz, Chloroform-d) δ 5.00 (s, 1H), 1.70 (s, 6H), 1.64 (s, 6H).

^{13}C NMR (126 MHz, Chloroform-d) δ 98.61 (d, J = 8.8 Hz), 95.07 (d, J = 8.6 Hz), 76.84 (d, J = 9.6 Hz), 11.13, 9.29.

Anal. Calc. for $C_{18}H_{26}Cl_4Rh_2$: C, 36.64, H, 4.44; Found: C, 36.78, H, 4.50.

[Cp*^{dtBuPh}RhCl$_2$]$_2$

Reaction time: 16 h in iPrOH. Product obtained as a red-orange solid (0.1494g, 54.2% yield).

^{1}H NMR (500 MHz, Chloroform-d) δ 7.51 (s, 2H), 7.39 (s, 1H), 1.71 (s, 6H), 1.70 (s, 6H), 1.32 (s, 18H).

13C NMR (126 MHz, Chloroform-d) δ 127.15, 124.99, 122.36, 100.13 (d, *J* = 7.9 Hz), 93.01 (d, *J* = 8.9 Hz), 34.98, 31.42, 10.65, 9.55.

Anal. Calc. for $C_{46}H_{66}Cl_4Rh_2$: C, 57.16, H, 6.88; Found: C, 55.78, H, 6.88.

HRMS (EI+) calcd for $C_{46}H_{66}Cl_4Rh_2$: 964.2029, monomer: 482.1014 found: 482.1.

[Cp*RhCl$_2$]$_2$

Reaction time: 1 h in iPrOH. Product obtained as a red-orange solid (0.1321 g, 75% yield).

^{1}H NMR (700 MHz, $CDCl_3$) δ 1.61 (s, 15H).

^{13}C NMR (176 MHz, $CDCl_3$) δ 94.24 (d, *J* = 9.1 Hz), 9.53.

Anal. Calc. for $C_{20}H_{30}Cl_4Rh_2$: C, 38.87, H, 4.89; Found: C, 38.51, H, 4.65.

[Cp*^{Ph35}RhCl$_2$]$_2$

Reaction time: 16 h in iPrOH. Product obtained as a red solid.

^{1}H NMR (500 MHz, $CDCl_3$) δ 7.27 (s, 2H), 7.00 (s, 1H), 2.34 (s, 6H), 1.70 (s, 6H), 1.68 (s, 6H).

^{13}C NMR (126 MHz, Chloroform-*d*) δ 138.20, 130.86, 128.07, 99.49 (d, *J* = 8.1 Hz), 93.63 (d, *J* = 9.0 Hz), 91.75, 21.45, 10.83, 9.77.

General Procedure Synthesis of [Cp^{R}Rh(C$_6$Me$_6$)] Complexes

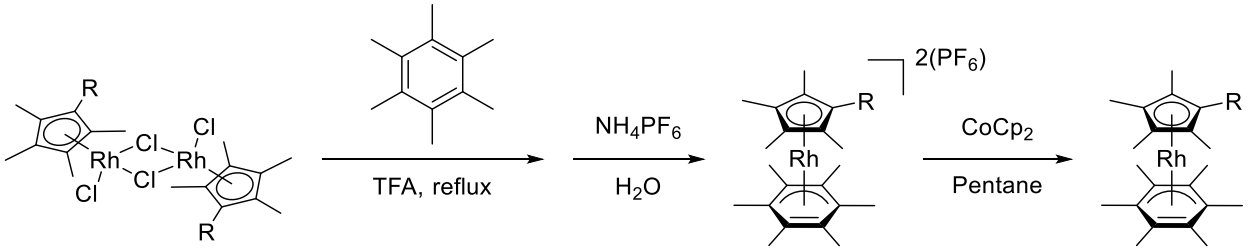

To a 10 mL round bottom flask was added [Cp^{R}RhCl$_2$]$_2$ (1 eq.) and a stir bar. To a 4 mL vial was added hexamethylbenzene (4.9 eq.) followed by trifluoroacetic acid (volume to 0.2 M concentration hexamethylbenzene). The vial was sonicated until mostly dissolved. The vial was then dumped in one motion into round bottom flask. The flask was fitted with a condenser and refluxed overnight. The mixture was allowed to cool to room temperature, then the solvent was removed on a rotary evaporator. Water (~3 mL) was added to the flask, then the mixture was transferred to a centrifuge tube. NH_4PF_6 (5 eq.) was added, then the mixture was gently shaken. The tube was centrifuged at 5000 rpm for 10 minutes, then the water was decanted off. Water was added to rinse the solid, then the tube was centrifuged again. The water was decanted off, then the solid was dried over P_2O_5 *in vacuo* overnight. The solid was transferred to a 20 mL vial then moved to a nitrogen filled glovebox. A stir bar was added to the vial followed by pentane (~3 mL). Cobaltocene (1.98 eq.) was added to the stirring solution, the vial was then capped and stirred for 1 h. The mixture was filtered through Celite, then dried *in vacuo*. The product was obtained as a purple solid. The complex was analyzed by NMR in C_6D_6.

X-Ray quality crystals of [Cp*^{Ph35}Rh(C_6Me_6)] were grown through slow growth in minimal cold (-35 °C) pentane.

[Cp*^{Ph35}Rh(C_6Me_6)]

^{1}H NMR (401 MHz, Benzene-d_6) δ 7.42 (s, 2H), 6.86 (s, 1H), 2.31 (s, 6H), 2.09 (s, 6H), 1.66 (s, 6H), 1.49 (s, 12H), 1.18 (s, 6H).

^{13}C NMR (176 MHz, Benzene-d_6) δ 136.53, 136.42, 133.99, 133.98, 131.36, 129.99, 105.65 (d, J = 7.3 Hz), 94.50 (d, J = 5.8 Hz), 92.79 (d, J = 4.0 Hz), 89.81 (d, J = 6.0 Hz), 64.66 (d, J = 16.4 Hz), 21.16, 17.85, 16.53, 13.81, 10.12, 9.02.

[Cp*^{3Ph35}Rh(C_6Me_6)]

^{1}H NMR (700 MHz, Benzene-d_6) δ 7.41 (s, 2H), 7.14 (s, 4H), 6.88 (s, 1H), 6.66 (s, 2H), 2.32 (s, 6H), 2.27 (s, 6H), 2.13 (s, 12H), 1.81 (s, 6H), 1.55 (s, 6H), 1.14 (s, 6H).

^{13}C NMR (126 MHz, Chloroform-d) δ 137.13, 136.60, 136.31, 135.62, 135.38, 130.15, 130.05, 108.38 (d, J = 5.8 Hz), 105.14, 93.67, 91.98 (d, J = 5.5 Hz), 65.83 (d, J = 16.3 Hz), 21.59, 21.39, 18.40, 14.75, 14.52, 11.85.

2.4.3. Experimental Procedures – Borylation Reactions

General Procedure for Methane Borylation

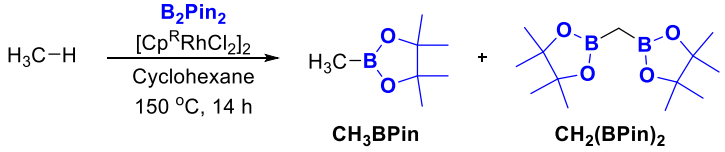

In a nitrogen filled glovebox, B_2Pin_2 (226 mg, 0.89 mmol, 1 eq.) and Cp^RRh catalyst (0.03 eq. Rh) were added to the well of a Parr reactor followed by a stir bar. Cyclohexane (7 mL) was added by graduated cylinder. The reactor was then sealed and removed from the glovebox. Methane (35 bar) was then added through the head, purging three times. The reactor was then inserted into an aluminum heating block pre-heated to 150 °C and left to stir for 14 h. The reactor was removed from the aluminum block and cooled for five minutes in a shallow pool of liquid nitrogen. After five minutes, the reactor was vented, removed from the liquid nitrogen, and allowed to come to room temperature open over the course of an hour. The reactor head was removed, and chlorobenzene (40 µL) added as standard along with additional cyclohexane (~2 mL). Reaction analyzed by GC-FID.

General Procedure for Methane Borylation Time Study

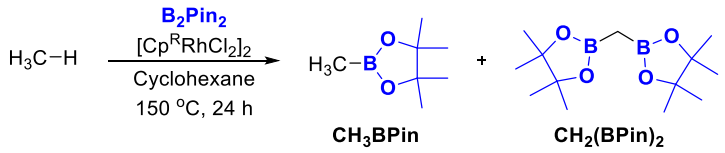

In a nitrogen filled glovebox, B_2Pin_2 (678 mg, 2.67 mmol, 1 eq.) and Cp^RRh catalyst (0.03 eq. Rh) were added the well of a Parr reactor followed by a stir bar. 2,2,4,6,6-pentmethylheptane

(40 mg) was weighed into a 4 mL vial. Cyclohexane (3 x 1 mL) added to the vial then transferred to the reactor well. Cyclohexane (18 mL) added to reactor well by graduated cylinder. The reactor was then sealed with an aliquot-taking head and removed from the glovebox. Methane (35 bar) was then added through the head, purging three times. The reactor was then inserted into an aluminum heating block pre-heated to 150 °C. Aliquots taken at the time points: 15 min, 30 min, 45 min, 1 h, 2 h, 4 h, 8 h, 24 h. Aliquots were analyzed by GC-FID.

Initial Rates Study

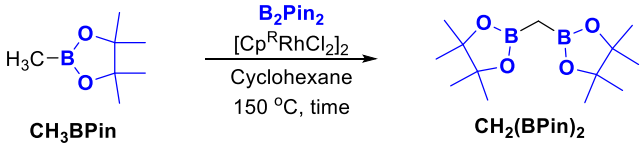

In a nitrogen filled glovebox, B_2Pin_2 (41 mg, 0.166 mmol, 1 eq.) and $[Cp^RRhCl_2]_2$ (0.0025 mmol, 0.015 eq.) were added to a 4 mL Schlenk tube followed by a stir bar. CH_3BPin (185 mg, 1.3 mmol) was weighed into a 10 mL volumetric flask. Cyclohexane was added to the line on the volumetric flask. The solution was shaken and transferred to a 20 mL vial. CH_3BPin stock solution (0.13 M, 1.3 mL, 0.169 mmol, 1 eq.) was added to the Schlenk tube. The Schlenk tube was sealed. These steps were repeated to make four identical tubes. The Schlenk tubes were removed from the glovebox then inserted into an oil bath preheated to 150 °C. The reactions were stirred for several minutes (Cp*: 10, 11, 12, 13 min) (Cp^{*Ph35}: 10, 15, 20, 25 min) then were removed from the oil bath and plunged into ice water to quench the reaction. Once cool, the tubes were opened and chlorobenzene (10 µL) was added, then the reaction was transferred to a vial, rinsing the tube twice with cyclohexane (~2 mL). Reactions were analyzed by GC-FID to find borylated product yields and ratios.

Initial Rates Study with Catalyst Activation

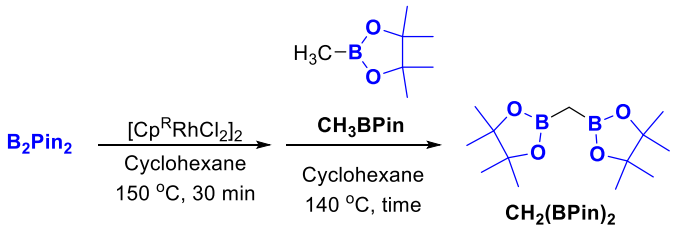

In a nitrogen filled glovebox, B_2Pin_2 (205 mg, 0.83 mmol) and $[Cp^RRhCl_2]_2$ (0.0125 mmol) were added to a 10 mL Schlenk tube followed by a stir bar. Cyclohexane (4 mL) was added to the tube, then the tube was sealed and removed from the glovebox. The tube was heated to 150 °C and stirred for 30 min. The tube was cooled in an ice bath and returned to the glovebox. CH_3BPin (2.5 mL of a 0.338 M solution in cyclohexane) was added to the tube, then mixed. Four Schlenk tubes were prepared, each containing 1.3 mL of the bulk solution. These tubes were sealed and removed from the glovebox, then inserted into an oil bath preheated to 140 °C. Reactions stirred for several minutes (Cp*: 3, 6, 9, 12 min) (Cp^{*Ph35}: 5, 10, 15, 20 min) then removed from the oil bath and plunged into ice water to quench the reaction. Once cool, the tubes were opened and chlorobenzene (10 µL) was added, then the reaction was transferred to a vial, rinsing the tube twice with cyclohexane (~2 mL). Reactions were analyzed by GC-FID to find borylated product yields and ratios.

Methane/Ethane Borylation Competition Studies

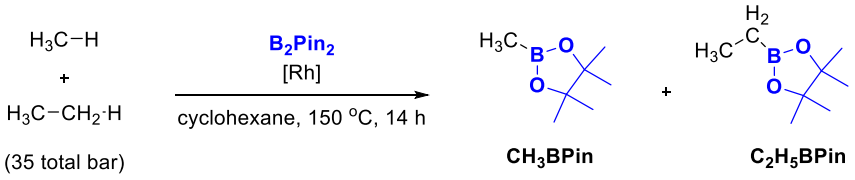

In a nitrogen filled glovebox, B_2Pin_2 (226 mg, 0.89 mmol, 1 eq.) and Cp^RRh catalyst (0.03 eq. Rh) were added to the well of the analog gage Parr reactor followed by a stir bar. Cyclohexane (7 mL) was added by graduated cylinder. The reactor was then sealed and removed from the glovebox and the reactor was massed. Reactor was pressurized with ethane (~14 bar) then rapidly massed on the same balance. The reactor was then pressurized with methane to 35 bar total pressure. The reactor was again weighed, then the reactor base was lowered into an oil bath preheated to 150 °C. Reactor heated and stirred for 14 h. The reactor was allowed to cool to room temperature over several hours, then vented. Chlorobenzene (40 µL) was added as standard, then transferred to a 20 mL vial, rinsing with cyclohexane (~2 mL). Reactions were analyzed by GC-FID to find borylated product yields and ratios.

Methane/Hexane Borylation Competition Studies

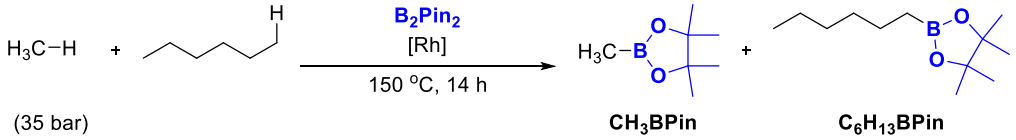

In a nitrogen filled glovebox, B_2Pin_2 (226 mg, 0.89 mmol, 1 eq.) and Cp^RRh catalyst (0.03 eq. Rh) were added to the well of a Parr reactor followed by a stir bar. *n*-Hexane (7 mL) was added by graduated cylinder. The reactor was then sealed and removed from the glovebox. Methane (35

bar) was then added through the head, purging three times. The reactor was then inserted into an aluminum heating block pre-heated to 150 °C and left to stir for 14 h. The reactor was removed from the aluminum block and cooled for five minutes in a shallow pool of liquid nitrogen. After five minutes, the reactor was vented, removed from the liquid nitrogen, and allowed to come to room temperature open over the course of an hour. The reactor head was removed, and chlorobenzene (40 μL) was added as standard along with additional cyclohexane (~2 mL). The reaction was analyzed by GC-FID to find borylated product yields and ratios.

Borylation of 1,4-disubstituted arenes

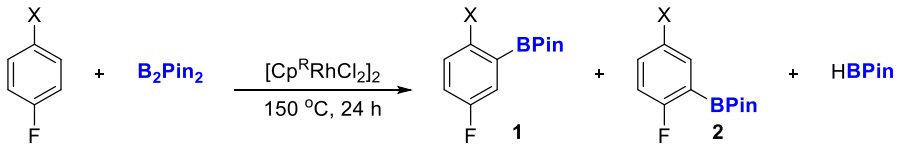

In a nitrogen filled glovebox B_2Pin_2 (127 mg, 0.5 mmol, 1 eq.) and $[Cp^RRhCl_2]_2$ (0.0075 mmol, 0.015 eq.) were added to a 4 mL Schlenk tube with a stir bar. 1,4-disubstituted arene (2 mmol, 4 eq.) was weighed into a 4 mL vial. THF (1 mL) was added to vial, then the solution was transferred to tube. The vial was rinsed with THF (1 mL), then transferred to tube. The tube was sealed and removed from glovebox. The tube was submerged in a preheated oil bath and heated at 150 °C for 24 h. The tube was removed from the bath and allowed to cool to room temperature before opening. The mixture was filtered through silica then analyzed by ^{19}F-NMR to determine the identity of the borylated products and ratios.

N-alkylpyrrole Borylation Studies

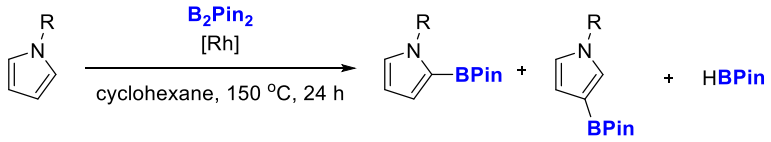

In a nitrogen filled glovebox B_2Pin_2 (127 mg, 0.5 mmol, 1 eq.) and $[Cp^RRhCl_2]_2$ (0.0075 mmol, 0.015 eq.) were added to a 4 mL Schlenk tube with a stir bar. N-alkylpyrrole (2 mmol, 4 eq.) was weighed into a 4 mL vial. Cyclohexane (1 mL) was added to vial, then the solution was transferred to tube. The vial was rinsed with cyclohexane (2x1 mL), then transferred to tube. The tube was sealed and removed from the glovebox. The tube was submerged in a preheated oil bath and heated at 150 °C for 24 h. The tube was removed from the bath and allowed to cool to room temperature before opening. The mixture as then filtered through celite. The filtered solution was diluted with DCM and washed with water to remove oxidized byproduct. The solution was analyzed by GC-FID to obtain borylated product ratios.

Furan Borylation Studies

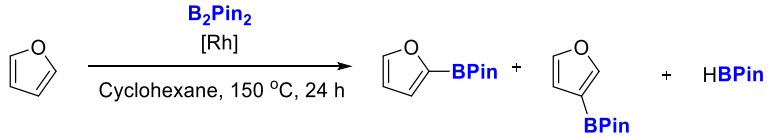

In a nitrogen filled glovebox, a stock solution of furan (2.5 M) in cyclohexane was prepared by adding furan (1.7 g) to a 10 mL volumetric flask then filling to the line with cyclohexane. The solution was then mixed and transferred to a 20 mL vial. B_2Pin_2 (127 mg, 0.5 mmol, 1 eq.) and $[Cp^RRhCl_2]_2$ (0.0075 mmol, 0.015 eq.) were added to a 4 mL Schlenk tube followed by a stir bar. Furan (2 mL, 2.5 M in cyclohexane, 5 mmol, 10 eq.) was added to the tube, then the tube was

sealed and removed from the glovebox. The tube was then submerged in an oil bath preheated to 150 °C and stirred for 24 h. The tube was removed from the oil bath and allowed to cool to room temperature before opening. The reaction mixture was then transferred to a 20 mL vial and the Schlenk tube was washed with cyclohexane (3x1 mL), transferring to the vial. The solution was analyzed by GC-FID to determine borylated product ratios.

2.4.4. X–Ray Crystallographic Data

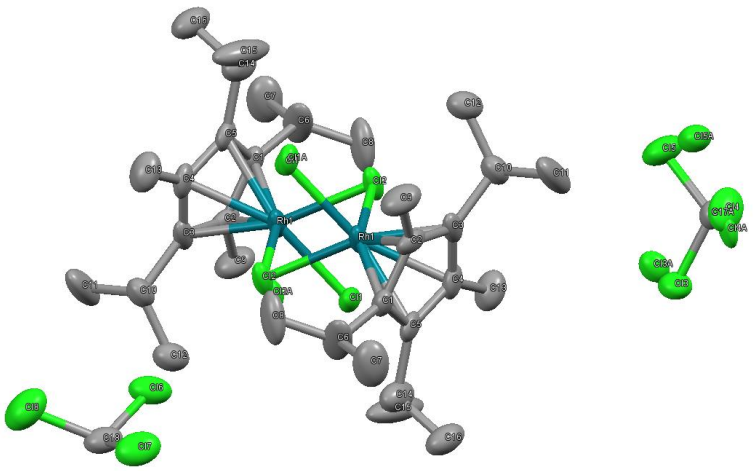

[Cp*^{3iPr}RhCl$_2$]$_2$

Structure Determination.

Orange blocks of **[Cp*^{3iPr}RhCl$_2$]$_2$** were obtained from a chloroform solution of the compound at 25 ºC. A crystal of dimensions 0.18 x 0.13 x 0.13 mm was mounted on a Rigaku AFC10K Saturn 944+ CCD-based X-ray diffractometer equipped with a low temperature device and Micromax-007HF Cu-target micro-focus rotating anode (λ = 1.54187 Å) operated at 1.2 kW power (40 kV,

30 mA). The X-ray intensities were measured at 85(1) K with the detector placed at a distance 42.00 mm from the crystal. A total of 2028 images were collected with an oscillation width of 1.0° in w. The exposure times were 1 sec. for the low angle images, 4 sec. for high angle. Rigaku d*trek images were exported to CrysAlisPro for processing and corrected for absorption. The integration of the data yielded a total of 19320 reflections to a maximum 2q value of 138.48° of which 4669 were independent and 4568 were greater than 2s(I). The final cell constants were based on the xyz centroids of 12102 reflections above 10s(I). Analysis of the data showed negligible decay during data collection. The structure was solved and refined with the Bruker SHELXTL (version 2016/6) software package, using the space group P1bar with Z = 1 for the formula $C_{36}H_{58}Cl_{16}Rh_2$. All non-hydrogen atoms were refined anisotropically with the hydrogen atoms placed in idealized positions. The chlorine atoms of the Rh-complex are disordered in two closely related positions. One chloroform solvate is also disordered. Full matrix least-squares refinement based on F2 converged at R1 = 0.0581 and wR2 = 0.1503 [based on I > 2sigma(I)], R1 = 0.0587 and wR2 = 0.1509 for all data. Additional details are avaiable in the CIF file (CCDC deposit number 1848432).

G.M. Sheldrick (2015) "Crystal structure refinement with SHELXL", Acta Cryst., C71, 3-8 (Open Access).

CrystalClear Expert 2.0 r16, Rigaku Americas and Rigaku Corporation (2014), Rigaku Americas, 9009, TX, USA 77381-5209, Rigaku Tokyo, 196-8666, Japan.

CrysAlisPro 1.171.38.41 (Rigaku Oxford Diffraction, 2015).

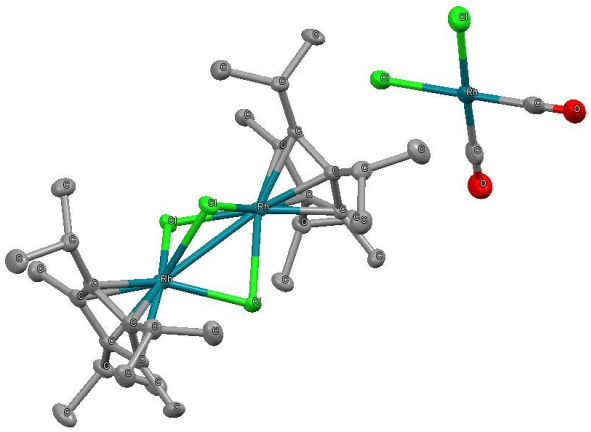

Structure Determination.

Orange plates of **(Cp^{*3iPr}_2 Rh_2Cl_3)($RhCl_2(CO_2)$)** were obtained by vapor diffusion of pentane into a chloroform solution of a mixture of **1** and **2** at –22 ºC. A crystal of dimensions 0.12 x 0.07 x 0.03 mm was mounted on a Rigaku AFC10K Saturn 944+ CCD-based X-ray diffractometer equipped with a low temperature device and Micromax-007HF Cu-target micro-focus rotating anode (λ = 1.54187 Å) operated at 1.2 kW power (40 kV, 30 mA). The X-ray intensities were measured at 85(1) K with the detector placed at a distance 42.00 mm from the crystal. A total of 2028 images were collected with an oscillation width of 1.0° in w. The exposure times were 1 sec. for the low angle images, 4 sec. for high angle. Rigaku d*trek images were exported to CrysAlisPro for processing and corrected for absorption. The integration of the data yielded a total of 58528 reflections to a maximum 2q value of 138.78° of which 7198 were independent and 6810 were greater than 2s(I). The final cell constants were based on the xyz centroids of 26176 reflections above 10s(I). Analysis of the data showed negligible decay during data collection. The structure was solved and refined with the Bruker SHELXTL (version 2016/6) software package, using the space group P2(1)/c with Z = 4 for the formula C34H54O2Cl5Rh3. All non-hydrogen atoms were refined anisotropically with the hydrogen atoms placed in idealized positions. Full matrix least-

squares refinement based on F2 converged at R1 = 0.0310 and wR2 = 0.0830 [based on I > 2sigma(I)], R1 = 0.0327 and wR2 = 0.0851 for all data. Additional details are avaiable in the CIF file (CCDC deposit number 1848431).

G.M. Sheldrick (2015) "Crystal structure refinement with SHELXL", Acta Cryst., C71, 3-8 (Open Access).

CrystalClear Expert 2.0 r16, Rigaku Americas and Rigaku Corporation (2014), Rigaku Americas, 9009, TX, USA 77381-5209, Rigaku Tokyo, 196-8666, Japan.

CrysAlisPro 1.171.38.41 (Rigaku Oxford Diffraction, 2015).

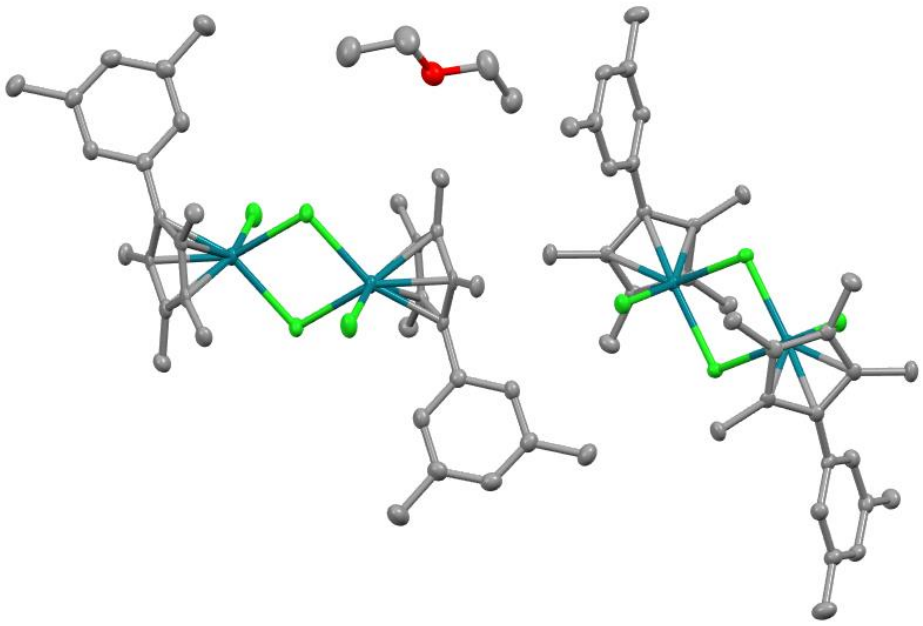

Structure Determination.

Orange needles of **[Cp*^{Ph35}RhCl$_2$]$_2$** were grown from a chloroform/diethyl ether solution of the compound at 23 deg. C. A crystal of dimensions 0.15 x 0.05 x 0.02 mm was mounted on a Rigaku AFC10K Saturn 944+ CCD-based X-ray diffractometer equipped with a low temperature device and Micromax-007HF Cu-target micro-focus rotating anode (l = 1.54187 A) operated at 1.2 kW power (40 kV, 30 mA). The X-ray intensities were measured at 85(1) K with the detector placed at a distance 42.00 mm from the crystal. A total of 2028 images were collected with an oscillation width of 1.0° in w. The exposure times were 1 sec. for the low angle images, 3 sec. for high angle. Rigaku d*trek images were exported to CrysAlisPro for processing and corrected for absorption. The integration of the data yielded a total of 28264 reflections to a maximum 2q value of 138.71° of which 6757 were independent and 6372 were greater than 2s(I). The final cell constants were based on the xyz centroids of 14182 reflections above 10s(I). Analysis of the data showed negligible decay during data collection. The structure was solved and refined with the Bruker SHELXTL (version 2016/6) software package, using the space group P1bar with Z = 2 for

the formula $C_{38}H_{52}OCl_4Rh_2$. All non-hydrogen atoms were refined anisotropically with the hydrogen atoms placed in idealized positions. Full matrix least-squares refinement based on F^2 converged at R1 = 0.0331 and wR2 = 0.0915 [based on I > 2sigma(I)], R1 = 0.0348 and wR2 = 0.0942 for all data. Acknowledgement is made for funding from NSF grant CHE-0840456 for X-ray instrumentation.

G.M. Sheldrick (2015) "Crystal structure refinement with SHELXL", Acta Cryst., C71, 3-8 (Open Access).

CrystalClear Expert 2.0 r16, Rigaku Americas and Rigaku Corporation (2014), Rigaku Americas, 9009, TX, USA 77381-5209, Rigaku Tokyo, 196-8666, Japan.

CrysAlisPro 1.171.38.41 (Rigaku Oxford Diffraction, 2015).

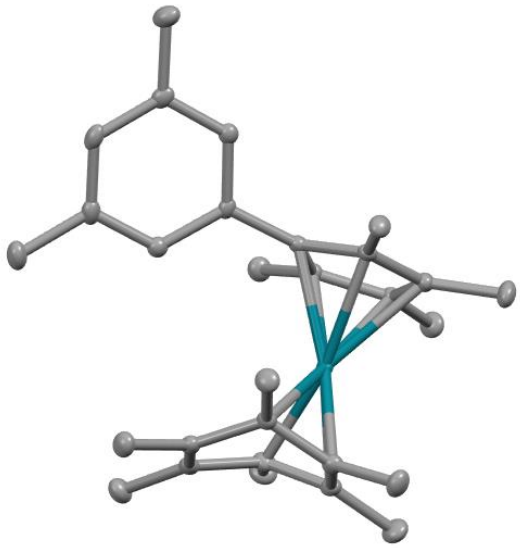

Structure Determination.

Brown plates of **[Cp*^{Ph35}Rh(C_6Me_6)]** were grown from a pentane solution of the compound at -35 deg. C. A crystal of dimensions 0.18 x 0.18 x 0.17 mm was mounted on a Rigaku AFC10K Saturn 944+ CCD-based X-ray diffractometer equipped with a low temperature device and Micromax-007HF Cu-target micro-focus rotating anode (l = 1.54187 A) operated at 1.2 kW power (40 kV, 30 mA). The X-ray intensities were measured at 85(1) K with the detector placed at a distance 42.00 mm from the crystal. A total of 2028 images were collected with an oscillation width of 1.0° in w. The exposure times were 1 sec. for the low angle images, 4 sec. for high angle. Rigaku d*trek images were exported to CrysAlisPro for processing and corrected for absorption. The integration of the data yielded a total of 71195 reflections to a maximum 2q value of 138.48° of which 4512 were independent and 4504 were greater than 2s(I). The final cell constants were based on the xyz centroids of 52844 reflections above 10s(I). Analysis of the data showed negligible decay during data collection. The structure was solved and refined with the Bruker SHELXTL (version 2018/3) software package, using the space group Pbca with Z = 8 for the formula $C_{29}H_{39}Rh$. All non-hydrogen atoms were refined anisotropically with the hydrogen atoms

placed in idealized positions. Full matrix least-squares refinement based on F^2 converged at R1 = 0.0244 and wR2 = 0.0244 [based on I > 2sigma(I)], R1 = 0.0669 and wR2 = 0.0669 for all data. Acknowledgement is made for funding from NSF grant CHE-0840456 for X-ray instrumentation.

G.M. Sheldrick (2015) "Crystal structure refinement with SHELXL", Acta Cryst., C71, 3-8 (Open Access).

CrystalClear Expert 2.0 r16, Rigaku Americas and Rigaku Corporation (2014), Rigaku Americas, 9009, TX, USA 77381-5209, Rigaku Tokyo, 196-8666, Japan.

CrysAlisPro 1.171.38.41 (Rigaku Oxford Diffraction, 2015).

2.5. References

[1] Chen, H.; Schlecht, S.; Semple, T. C.; Hartwig, J. F. Thermal, catalytic, regiospecific functionalization of alkanes. *Science* **2000**, *287*, 1995-1997.
[2] Cho, J.; Iverson, C. N.; Smith, M. R. Steric and chelate directing effects in aromatic borylation. *J. Am. Chem. Soc.* **2000**, *122*, 12868-12869.
[3] Cho, J.; Tse, M. K.; Holmes, D.; Maleczka, R. E.; Smith, M. R. Remarkably selective iridium catalysts for the elaboration of aromatic C–H bonds. *Science* **2002**, *295*, 305-308.
[4] Ishiyama, T.; Takagi, J.; Hartwig, J. F.; Miyaura, N. A stoichiometric aromatic C–H borylation catalyzed by iridium(I)/2,2'bipyridine complexes at room temperature. *Angew. Chem. Int. Ed.* **2002**, *41*, 3056-3058.
[5] Ishiyama, T.; Takagi, J.; Ishida, K.; Miyaura, N.; Anastasi, N. R.; Hartwig, J. F. Mild iridium-catalyzed borylation of arenes. High turnover numbers, room temperature reactions, and isolation of a potential intermediate. *J. Am. Chem. Soc.* **2002**, *124*, 390-391.
[6] Chotana, G. A.; Rak, M. A.; Smith, M. R. Sterically directed functionalization of aromatic C–H bonds: Selective borylation ortho to cyano groups in arenes and heterocycles *J. Am. Chem. Soc.* **2005**, *127*, 10539-10544.
[7] Tse, M. K.; Cho, J.; Smith, M. R. Regioselective aromatic borylation in an inert solvent. *Org. Lett.* **2001**, *3*, 2831-2833.
[8] Wei, C. S.; Jiménez-Hoyos, C. A.; Videa, M. F.; Hartwig, J. F.; Hall, M. B. Origins of the selectivity for borylation of primary over secondary C–H bonds catalyzed by Cp*-rhodium complexes. *J. Am. Chem. Soc.* **2010**, *132*, 3078-3091.
[9] Cook, A. K.; Schimler, S. D.; Matzger, A. J.; Sanford, M. S. Catalyst controlled selectivity in the C–H borylation of methane and ethane. *Science* **2016**, *351*, 1421-1424.
[10] Smith, K. T.; Berritt, S.; González-Moreiras, M.; Ahn, S.; Smith, M. R.; Baik, M.; Mindiola, D. J. Catalytic borylation of methane. *Science* **2016**, *351*, 1424-1427.

[11] Gunslaus, N. J.; Konnick, M. M.; Hashiguchi, B. G.; Periana, R. A. Discrete molecular catalysts for methane functionalization. *Isr. J. Chem*. **2014**, *54*, 1467–1480.
[12] Schwarz, H. Chemistry with methane: concepts rather than recipes. *Angew. Chem. Int. Ed*. **2011**, *50*, 10096–10115.
[13] Hartwig, J. F.; Cook, K. S.; Hapke, M.; Incarvito, C. D.; Fan, Y.; Webster, C. E.; Hall, M. B. Rhodium boryl complexes in the catalytic, terminal functionalization of alkanes. *J. Am. Chem. Soc.* **2005**, *127*, 2538-2552.
[14] Hyster, T. K.; Dalton, D. M.; Rovis, T. Ligand design for Rh(III)-catalyzed C–H activation: an unsymmetrical cyclopentadienyl group enables a regioselective synthesis of dihydroisoquinolones. *Chem. Sci.* **2015**, *6*, 254–258.
[15] Semakul, N.; Jackson, K. E.; Paton, R. S.; Rovis, T. Heptamethylindenyl (Ind*) enables diastereoselective benzamidation of cyclopropenes *via* Rh(III)-catalyzed C–H activation. *Chem. Sci.* **2017**, *8*, 1015–1020.
[16] Umeda, N.; Hirano, K.; Satoh, T.; Miura, M. Rhodium-catalyzed mono- and divinylation of 1-phenylpyrazoles and related compounds via regioselective C−H bond cleavage. *J. Org. Chem.* **2009**, *74*, 7094–7099.
[17] Wencel-Delord, J.; Nimphius, C.; Patureau, F. W.; Glorius, F. [Rh^{III}Cp*]-catalyzed dehydrogenative aryl–aryl bond formation. *Angew. Chem. Int. Ed.* **2012**, *51*, 2247–2251.
[18] Piou, T.; Rovis, T. Rhodium-catalysed *syn*-carboamination of alkenes via a transient directing group *Nature* **2015**, *527*, 86–90.
[19] (a) Shi, Z.; Boultadakis-Arapinis, M.; Koester, D. C.; Glorius, F. Rh(III)-catalyzed intramolecular redox-neutral cyclization of alkenes *via* C–H activation. *Chem. Commun.* **2014**, *50*, 2650-2652. (b) Zhao, D.; Vásquez-Céspedes, S.; Glorius, F. Rhodium(III)-catalyzed cyclative capture approach to diverse 1-aminoindoline derivatives at room temperature. *Angew. Chem. Int. Ed.* **2015**, *54*, 1657–1661. (c) Hong, S. Y.; Jeong, J.; Chang, S. [4+2] or [4+1] annulation: Changing the reaction pathway of a rhodium-catalyzed process by tuning the Cp ligand. *Angew. Chem. Int. Ed.* **2017**, *56*, 2408–2412. (d) Park, Y.; Park, K. T.; Kim, J. G.; Chang, S. Mechanistic studies on the Rh(III)-mediated amido transfer process leading to robust C–H amination with a new type of amidating reagent. *J. Am. Chem. Soc.* **2015**, *137*, 4534–4542. (e) Otley, K. D.; Ellman, J. A. An efficient method for the preparation of styrene derivatives via Rh(III)-catalyzed direct C–H vinylation. *Org. Lett.* **2015**, *17*, 1332–1335. (f) Brasse, M.; Cámpora, J.; Ellman, J. A.; Bergman, R. G. Mechanistic study of the oxidative coupling of styrene with 2-phenylpyridine derivatives catalyzed by cationic rhodium(III) via C–H activation. *J. Am. Chem. Soc.* **2013**, *135*, 6427–6430. (g) Morioka, R.; Nobushige, K.; Satoh, T.; Hirano, K.; Miura, M. Synthesis of indolo[1,2-*a*][1,8]naphthyridines by rhodium(III)-catalyzed dehydrogenative coupling via rollover cyclometalation. *Org. Lett.* **2015**, *17*, 3130–3133.
[20] (a) Hyster, T. K.; Rovis, T. An improved catalyst architecture for rhodium(III) catalyzed C–H activation and its application to pyridone synthesis. *Chem. Sci.* **2011**, *2*, 1606–1610. (b) Bosch, W. H.; Englert, U.; Pfister, B.; Stauber, R.; Salzer, A. Transition-metal complexes of the optically active cyclopentadienyl ligand PinCp*: Crystal structure of (S_{Re})-(η^5-PinCp*)Re(NO)(PPh_3)[$CONHCH(CH_3)C_{10}H_7$]. *Eur. J. Inorg. Chem.* **1999**, 1497–1505.
[21] White, C.; Yates, A.; Maitlis, P. M.; (η_5-Pentamethylcyclopentadienyl)rhodium and -iridium compounds. *Inorg. Syn.* **1992**, *29*, 228–234.
[22] Piou, T.; Romanov-Michailidis, F.; Romanova-Michaelides, M.; Jackson, K. E.; Semakul, N.; Taggart, T. D.; Newell, B. S.; Rithner, C. D.; Paton, R. S.; Rovis, T. Correlating reactivity and selectivity to cyclopentadienyl ligand properties in Rh(III)-catalyzed C–H activation reactions: An experimental and computational study. *J. Am. Chem. Soc.* **2017**, *139*, 1296–1310.
[23] Shimogawa, R.; Takao, T.; Suzuki, H.; Half-sandwich cyclopentadienyl iridium dichloride monomer $Cp^{‡}IrCl_2$ ($Cp^{‡}$: 1,2,4-tri-tert-butylcyclopentadienyl). *Chem. Lett.* **2017**, *46*, 197–199.
[24] Chizhevsky, I. T.; Rastova, N. V.; Kolobova, N. E.; Petrovskii, P. V.; Vinogradova, L. E. Cationic products from *O*-protonation reaction of 2-acylnorbornadiene complexes of rhodium with hydrogen chloride in ether: structure, reactivity and nature of hydrogen bond. *J. Organomet. Chem.* **1987**, *335*, 109–123.
[25] Brown, L. C.; Ressegue, E.; Merola, J. S. Rapid access to derivatized, dimeric, ring-Substituted dichloro(cyclopentadienyl)rhodium(III) and iridium(III) complexes. *Organometallics* **2016**, *35*, 4014–4022.
[26] Xu, Y.-F.; Pang, Z.; Chen, M.-Q. Preparation, crystal structure and spectroscopic studies of mixed valence compound [$(Cp^{4i}Rh)_2(\mu\text{-}Cl)_3$] [$Rh(CO)_2Cl_2$]. *Chin. J. Chem.* **2001**, *19*, 356–361.
[27] (a) Samouei, H.; Grushin, V. V.; New, highly efficient, simple, safe, and scalable synthesis of [$(Ph_3P)_3Ru(CO)(H)_2$]. *Organometallics* **2013**, *32*, 4440–4443. (b) Chatt, J.; Shaw, B. L.; Field, A. E. The Formation of hydrido- and carbonyl complexes of ruthenium by reaction of certain of its complexes with alcohols. *Chem. Ind.* **1960**, 931. (c) Vaska, L.; DiLuzio, J. W.; Complex carbonyl hydrides of osmium and ruthenium. *J. Am. Chem. Soc.* **1961**, *83*, 1262–1263. (d) Vaska, L.; DiLuzio, J. W. Carbonyl and hydrio-carbonyl complexes of iridium by reaction with alcohols. Hydrido complexes by reaction with acid. *J. Am. Chem. Soc.* **1961**, *83*, 2784–2785.
[28] (a) Kim, J. H.; Park, H.; Chung, Y. K. Rhodium-catalyzed synthesis of esters from aryl iodides and alcohols: use of alcohols with/without the assistance of aldehydes as carbon monoxide and nucleophile sources. *RSC Adv.* **2017**, *7*, 190–194. (b) Chatt, J.; Shaw, B. L. Rhodium(I) and rhodium(III) carbonyl complexes containing tertiary phosphines

or tertiary arsines and halogen formed by the decarbonylation of alcohols and by the direct use of carbon monoxide. *J. Chem. Soc. A* **1966**, 1437–1442. (c) Masters, C.; McDonald, W. S.; Raper, G.; Shaw, B. L. Some novel complexes including very active hydrogenation catalysts formed from rhodium trichloride and tertiary t-butylphosphines. *J. Chem. Soc. D* **1971**, 210–211.
[29] Park, J. H.; Cho, Y.; Chung, Y. K. Rhodium-catalyzed Pauson–Khand-type reaction using alcohol as a source of carbon monoxide. *Angew. Chem. Int. Ed.* **2010**, *49*, 5138–5141.
[30] Notably, Suzuki has reported the use of ^{t}BuOH as a solvent to "prevent the over-reduction of the metal halides" in the synthesis of Cp^RIrCl_2 and $[Cp^RRhCl]_2$ complexes. However, the exact nature of the reduced side products was not characterized in this paper. See ref. 11.
[31] Habtemariam, A.; Liu, Z.; Soldevila, J. J.; Pizarro, A. M.; Sadler, P. J., Novel iridium/rhodium anti-cancer Compounds. US9408853 (B2), Aug. 8, 2016.
[32] Bowyer, J.; Merkert, J. W.; Geiger, W. E.; Rheingold, A. L;.Structural consequences of electron-transfer reactions. Part 18. Redox-induced hapticity changes: Effect of substituents on arene bending in a series of rhodium complexes. *Organometallics* **1989**, *8*, 191– 198.
[33] Lee, C.; Yang, W.; Parr, R. G. Development of the Colle-Salvetti correlation-energy formula into a functional of the electron density. *Phys. Rev. B* **1988**, *37*, 785-789.
[34] Vosko, S. H.; Wilk, L.; Nusair, M. Accurate spin-dependent electron liquid correlation energies for local spin density calculations: A critical analysis. *Can. J. Phys.* **1980**, *58*, 1200-1211.
[35] Hay, P. J.; Wadt, W. R. Ab initio effective core potentials for molecular calculations. Potentials for the transition metal atoms Sc to Hg. *J. Chem. Phys.* **1985**, *82*, 270-283.
[36] Hay, P. J.; Wadt, W. R. Ab initio effective core potentials for molecular calculations. Potentials for main group elements Na to Bi. *J. Chem. Phys.* **1985**, *82*, 284-298.
[37] Hay, P. J.; Wadt, W. R. Ab initio effective core potentials for molecular calculations. Potentials for K to Au including the outermost core orbitals. *J. Chem. Phys.* **1985**, *82*, 299-310.
[38] Shao, Y.; Gan, Z.; Epifanovsky, E.; Gilbert, A. T. B.; Wormit, M.; Kussman, J.; Lange, A. W.; Behn, A.; Deng, J.; Feng, X.; et al. Advances in molecular quantum chemistry contained in the Q-Chem 4 program package. *Mol. Phys.* **2015**, *113*, 184-215.
[39] Zimmerman, P. Reliable Transition state searches integrated with the growing string method. *J. Chem. Theory Comput.* **2013**, *9*, 3043-3050.
[40] Zimmerman, P. Growing string method with interpolation and optimization in internal coordinates: Method and examples. *J. Chem. Phys.* **2013**, *138*, 184102.
[41] Zimmerman, P. Single-ended transition state finding with the growing string method. *J. Comput. Chem.* **2015**, *36*, 601-611.
[42] Morris, D. M.; McGeagh M.; De Peña, D.; Merola, J. S. *Polyhedron* **2014**, *84*, 120-135.
[43] Lukešová, L.; Gyepes, R.; Pinkas, J.; Horáček, M.; Kubišta, J.; Čejka, J.; Mach, K. *Collect. Czech. Chem. Commun.* **2005**, *70*, 1589-1603.
[44] Davies, A. G.; Goddard, J. P. Lusztyk, E.; Lusztyk, J.; The electron spin resonance spectra of the penta-alkylcyclopentadienyl radicals MeR_4C_5 (R = Et, Pr, and Bu) and 1,3,5-Me_3-2,4-Et_2C_5: Relative substituent effects of the alkyl groups. *J. Chem. Soc. Perkin. Trans. II* **1982**, 737-743.
[45] Quindt, V.; Saurenz, D.; Schmitt, O.; Schär, M.; Dezember, T.; Wolmershäuser, Gotthelf Sitzmann, H. *J. Organomet. Chem.* **1999**, *579*, 376-384.
[46] Braude, E. A.; Coles, J. A. *J. Chem. Soc.* **1952**, 1430-1433.

CHAPTER 3

Photocatalyzed Pyridination of Electron-Rich Arenes

3.1. Introduction

Aromatic and heteroaromatic amines are ubiquitous in the pharmaceutical and agrochemical industries. As such, synthetic methods for the formation of C(sp^2)–N bonds are in high demand.[1,2,3] One of the most common approaches to C(sp^2)–nitrogen bond construction involves the S_NAr reaction between an aryl electrophile (aryl–X) and a nitrogen nucleophile (R_2NH) (**Figure 3.1.a.**).[4] These transformations proceed efficiently with arene substrates bearing resonance electron withdrawing groups, which stabilize negative charge build-up in the key Meisenheimer intermediate **A** (**Figure 3.1.a.**). In contrast, aryl–X substrates bearing electron donating substituents (e.g., FG = OR^1 in Figure 3.1.a.) typically show low reactivity via this pathway.

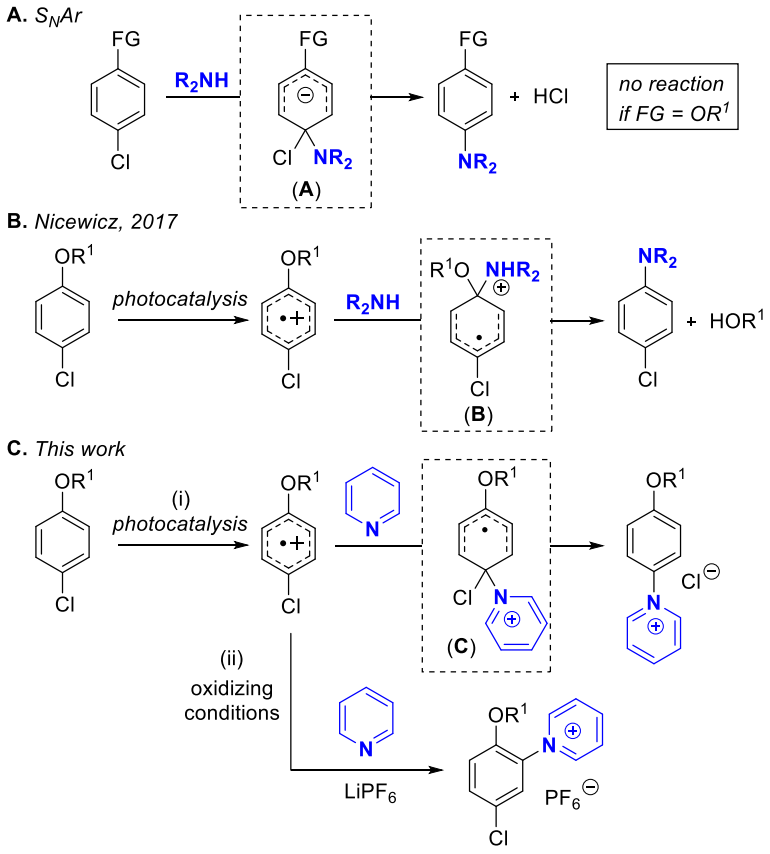

Figure 3.1. a. Traditional S_NAr reaction. **b.** Photocatalytic radical cation S_NAr reaction with R_2NH; selective for C(sp^2)–O cleavage (Nicewitz). **c.** (i) Proposed photocatalytic radical cation S_NAr reaction with pyridine; selective for C(sp^2)–Cl cleavage. (ii) C(sp^2)–H pyridination under complementary oxidizing conditions.

Recently, Nicewitz achieved the formal S_NAr amination of electron rich aromatic substrates by accessing an alternative mechanistic manifold (**Figure 3.1.b.**).[5] Here, an aryl electrophile is photocatalytically oxidized to the corresponding arene radical cation.[5,6,7,8,9] Under appropriate conditions, this renders the substrate susceptible to nucleophilic attack *ispo* to an C(sp^2)–OR^1 group (forming intermediate **B**). Loss of HOR^1 then enables the formation of aromatic amines where HNR_2 = imidazoles, pyrazoles, and triazoles. In contrast to traditional S_NAr amination reactions, this transformation is most effective with electron rich substrates (which are most easily

oxidized to the radical cations). Furthermore, it proceeds with high selectivity for the amination of C(sp^2)–OR^1 bonds relative to C(sp^2)–halide bonds. A more recent report by Lambert accessed a related pathway for the photoelectrocatalytic reaction of aryl fluoride electrophiles with analogous R_2NH nucleophiles.[10]

In this work, we expand this cation radical S_NAr-type reaction to pyridine-based nucleophiles (**Figure 3.1.c.**, i). This transformation yields aryl pyridinium products, which can serve as versatile precursors to anilines and piperidines.[11] At the outset, we noted that pyridine is distinct from the nucleophiles used in previous reports, because it does not contain an N–H bond.[5,10] As such, the leaving group in the S_NAr reaction is not HX (where HX = HOR^1 or HCl) but instead X^- (R^1O^- or Cl^-), which then serves as the charge balancing anion for the pyridinium product. We hypothesized that this key change could potentially reverse the selectivity for halide versus alkoxide substitution in these transformations (**Figure 3.1.c.**, i). This chapter describes the successful development, optimization, and scope of photocatalytic S_NAr type reactions between electron rich aryl electrophiles and pyridine. As predicted, high selectivity is observed for C(sp^2)–halide versus C(sp^2)–OR^1 pyridination.

Additionally, in an earlier study, Nicewicz demonstrates that the use of photocatalyst in the presence of a strong oxidant, 2,2,6,6-teteramethylpiperidine 1-oxyl (TEMPO) in an oxygen atmosphere, is able to drive C–H amination of electron rich arenes through generation of an aryl radical cation intermediate followed by nucleophilic attack by HNR_2 nucleophiles.[6] The presence of the strong oxidant allows H-atom abstraction upon reversible nucleophilic attack of the *ortho* and *para* carbons, allowing re-aromatization to aminated product. Substitution at the *ipso*- carbon is not reported in the presence of TEMPO. We predict that, under complementary conditions, the

putative radical cation intermediate can be intercepted to achieve selective photocatalytic C–H pyridination of analogous electron rich arene substrates (**Figure 3.1.c.**, ii).[12,13,14]

3.2. Results and Discussion

3.2.1. Substitution Results

Our initial studies subjected 4-chloroanisole to Nicewitz's photocatalytic S_NAr conditions, but using pyridine as the nitrogen nucleophile in place of imidazole. The reactions were carried out using blue LEDs at room temperature for 24 h under a nitrogen atmosphere with 1 : 1 dichloroethane (DCE) : trifluoroethanol (TFE) as the solvent. As shown in Scheme 1, the use of pyridine as the nucleophile resulted in a complete reversal in selectivity. Rather than high-yielding and selective substitution of the methoxy group with imidazole (Scheme 1a), the pyridine reaction afforded 1-(4-methoxyphenyl)pyridin-1-ium chloride (**2-Cl**) as the sole detectable pyridium-containing product. **2-Cl** was isolated in 37% yield, with the remaining mass balance being unreacted 4-chloroanisole. We reasoned that this reaction could be driven to completion by sequestration of the chloride leaving group. Indeed, as shown in Scheme 3.1.iii., the use of 3 equivalents of lithium hexafluorophosphate ($LiPF_6$) under otherwise identical conditions resulted in a dramatic increase in the yield (83% of **2-PF_6**) along with the precipitation of a white solid (likely LiCl).

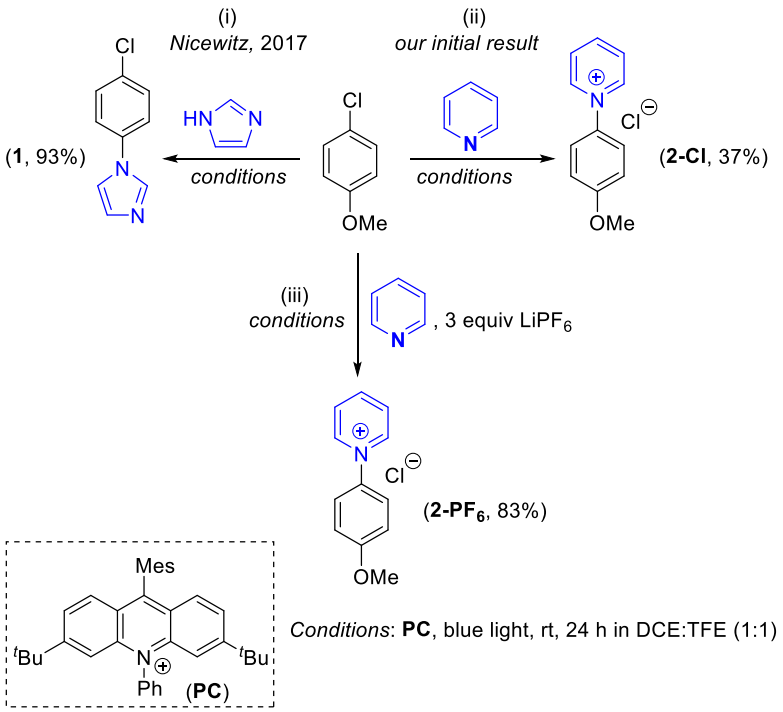

Scheme 3.1. (i) Photocatalytic radical cation S_NAr reaction between 4-chloroanisole and imidazole (Nicewitz). (ii) Change is selectivity for photocatalytic radical cation S_NAr reaction between 4-chloroanisole and pyridine. (iii) Impact of $LiPF_6$ on yield of pyridine reaction.

A variety of aryl halide electrophiles were investigated in this photocatalytic S_NAr reaction (**Table 3.1.**). The impact of changing the halide was first examined in a series of 4-haloanisole derivatives. All of the halogens (fluoride, chloride, bromide, and iodide) served as leaving groups and led to the selective formation of pyridinium product **1-PF$_6$**. However, the highest yields were obtained with the chloride (83%) and fluoride (38%) derivatives. Comparison between 4-, 3-, and 2-chloroanisole revealed that the 4-chloro shows significantly higher reactivity than 2-chloro (83% versus 38% yield, respectively), and that 3-chloro produces only trace product. This preference is also reflected in an intramolecular competition experiment with 2,4-dichloroanisole. Here, substitution at the 4-position is favored with 2.3 : 1 selectivity for **5-PF$_6$**. Additionally, this

preference is reflected without regard for the halogen in the 4-position, as there is a preference for **5-PF$_6$** and **11-PF$_6$** when either Cl or Br occupy the 4-position.

Other relatively electron rich aryl chlorides were also effective substrates for this transformation. For example, 4-chlorobiphenyl reacted to afford **6-PF$_6$** in 99% yield. Similar to the anisole derivatives, the 2-substituted analogue proved significantly less reactive, affording just trace **7-PF$_6$**. 2-Chlorothiophene reacted to afford the pyridinium product **12-PF$_6$** in 36% yield. In contrast, other electron rich heterocycles (e.g., 4-chloro-*N,N*-dimethylaniline and 5-chloro-benzothiophene) did not afford the desired products. This reaction also proved applicable to the bioactive molecule clofibrate, a cholesterol control pharmaceutical, in 61% yield of **12-PF$_6$**.

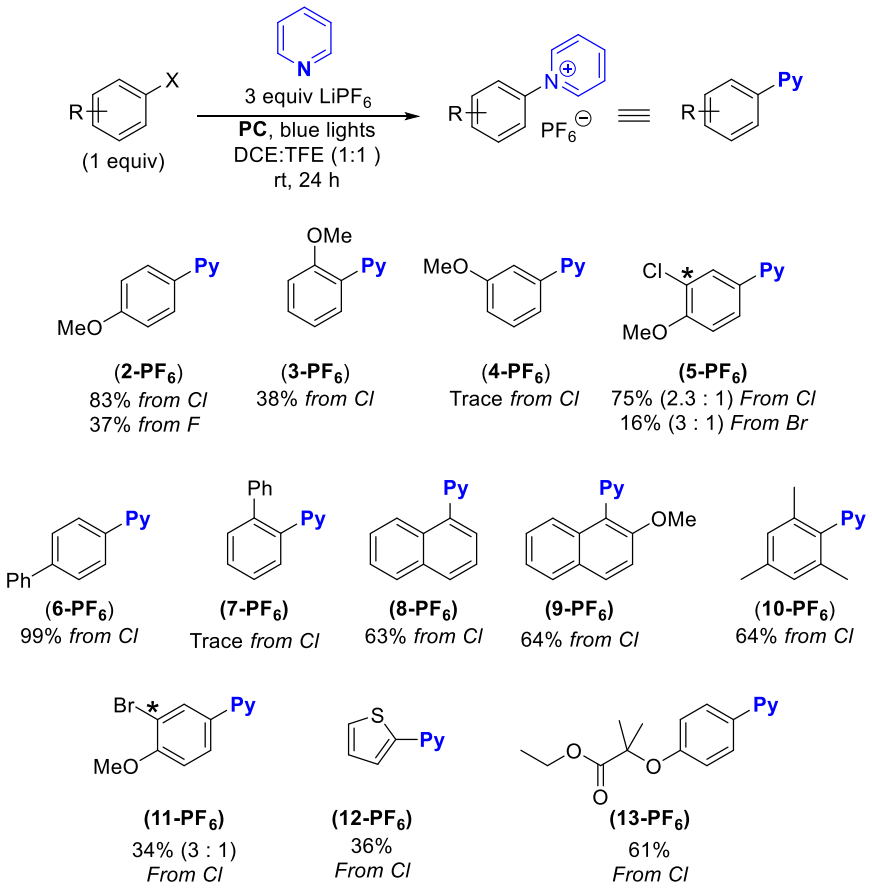

Table 3.1. Substrate scope of photocatalytic C(sp^2)–H amination of electron rich aryl halides with pyridine.

The substrate 4-chlorophenyl ether offers an interesting test case for the impact of leaving group on this transformation. Each aromatic ring in his substrate bears both a chloride and a *para*-chloro phenoxide substituent. Due to the relative electron deficiency of the 4-chlorophenyl ring, the 4-chlroophenoxy- group becomes a competent leaving group following excitation to the radical cation, forming products **14-PF6** and **15-PF6** in a 12 : 1 ratio respectively (**Scheme 3.2.a.**). The substrate 4-chlorophenyl phenyl ether provides complementary results. Substitution at the 4-chloro is still the preferred product, but as the electron rich phenyl ring is more likely to be oxidized to

the radical cation it produces relatively more product from substitution at the 4-chlorophenoxy-position, forming products **16-PF$_6$** : **17-PF$_6$** in a 7 : 1 ratio respectively (**Scheme 3.2.b.**).

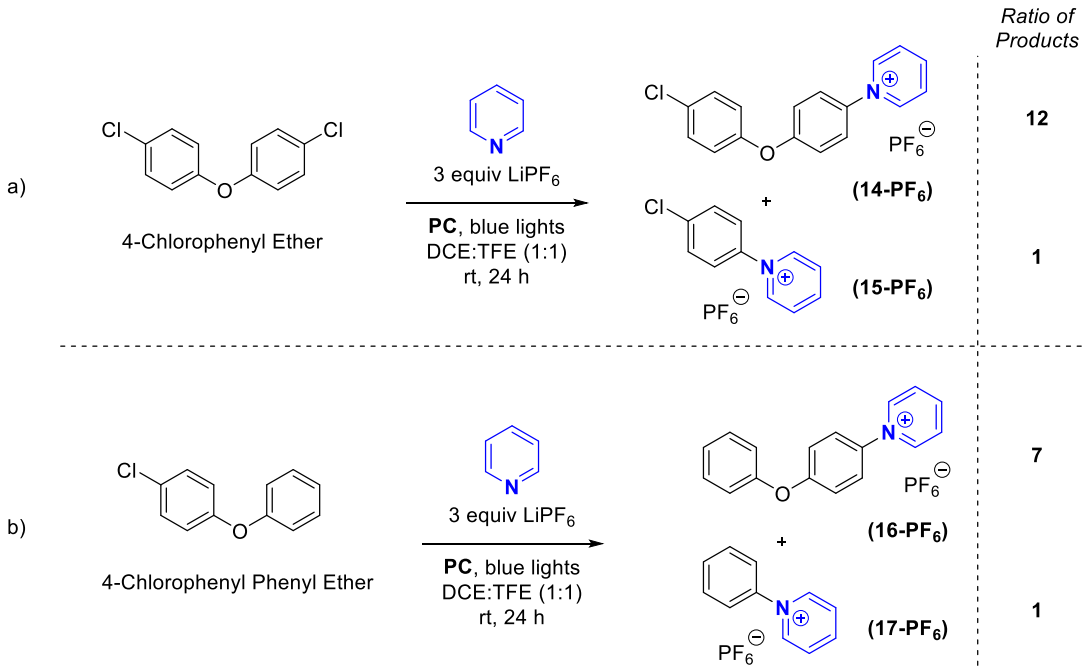

Scheme 3.2. Photocatalytic C(sp^2)–H pyridination of diaryl ethers.

3.2.2. C–H Pyridination Results

Literature reports suggest that the putative radical cation intermediate in this reaction could potentially participate in C(sp^2)–H functionalization processes with pyridine nucleophiles.[6,13,14] No C(sp^2)–H functionalization by-products were detected under the anaerobic conditions in **Scheme 3.1.**, ii or iii. However, when the reaction was conducted under an atmosphere of air in the presence of 20 mol % of TEMPO, a 1 : 1.5 mixture of the C–H functionalization product **18-PF$_6$** and the substitution product **2-PF$_6$** was formed. Furthermore, **18-PF$_6$** was the major product when the solvent was changed from 1: 1 DCE : TFE to 100% DCE (5 : 1 ratio of products, 50%

yield of **18-PF$_6$**). As shown in **Table 3.2.**, other halogen-containing substrates also produce a mixture of C–H and substitution products.

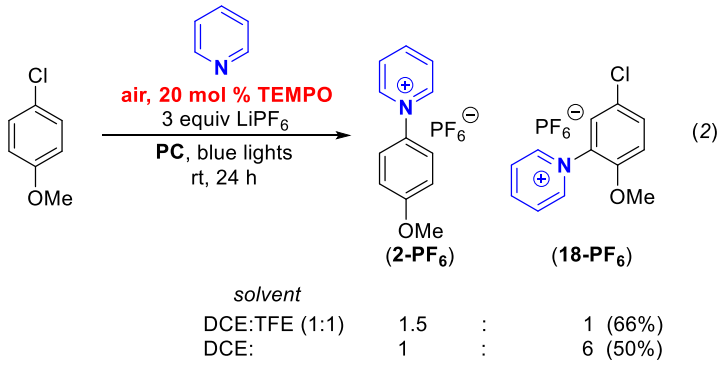

Scheme 3.3. Comparison of initial results of photocatalyzed C–H pyridination with DCE : TFE and pure DCE as solvent.

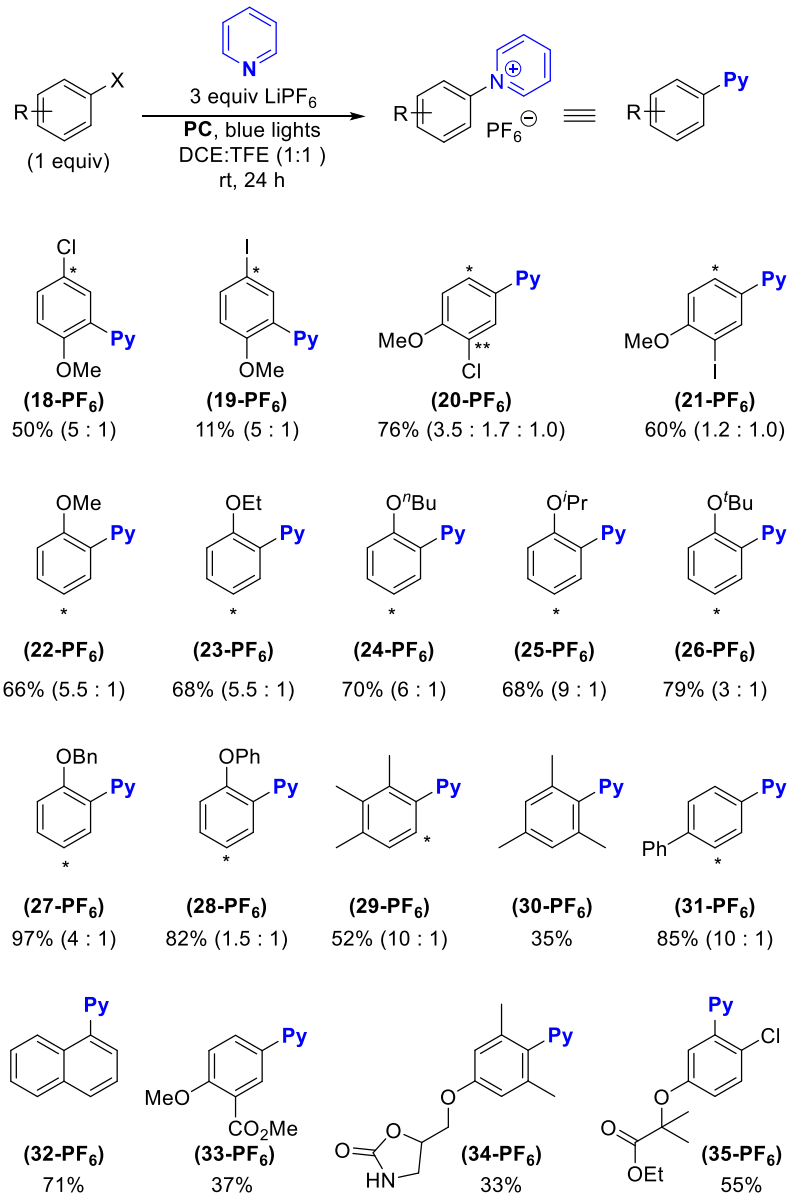

Table 3.2. Substrate scope of photocatalytic C(sp^2)–H amination of electron rich arenes with pyridine.

A series of aryl ethers were next evaluated as substrates. These reacted to afford pyridinium products **22-PF$_6$-28-PF$_6$** in isolated yields ranging from 68 to 97%. Interestingly, the *ortho*-isomer is favored in all of these systems, with selectivities ranging from 1.5: 1 (for OPh) to 9:1 (for O^{i}Pr). The steric parameters of the ether substituent have minimal impact on *ortho*-selectivity. For

instance, the relatively small OMe and much larger O^{t}Bu afforded similar *ortho* : para ratios of 5.1 : 1 and 3 : 1, respectively. Instead, electronic effects appear to dominate. For example, the lowest selectivity in the series (1.5 : 1 *ortho* : *para*) was observed with the OPh group, which is significantly less electron donating than the alkyl-substituted ether analogues. Furthermore, moving from an ether to a phenyl substituent resulted in a reversal in selectivity in favor of the *para* isomer (producing **31-PF$_6$** as a 10 : 1 *para* : *ortho* mixture). Notably, the *ortho*-selectivity observed in our reactions stands in contrast to the high *para* selectivity reported by Nicewitz with R_2NH (NR_2 = imidazoles, pyrazoles, and triazoles) nucleophiles under closely analogous conditions.[6] Similarly, high *para* selectivity has been reported in the electrochemical C(sp^2)–H pyridination of the anisole radical cation and derivatives thereof.[14] Notably, one very recent report observed *ortho*-selectivity in a photoelectrocatalytic C–H aminations of aryl ethers.[13] However, their explanation for this selectivity relates to a hydrogen bonding network formed between the solvent (hexafluoroisopropanol) and the ether and pyrazole substrates, an effect that is not feasible in our system.

This transformation was also proved effective for other electron rich substrates including trimethylbenzene isomers, and naphthalene (products **29-PF$_6$**, **30-PF$_6$**, and **32-PF$_6$**). In these systems, the observed site selectivity is analogous to that reported in the literature. Finally, the bioactive molecules metaxalone (product **34-PF$_6$**) and clofibrate (product **35-PF$_6$**) underwent C–H pyridination in moderate isolated yield under these conditions.

3.2.3. C–H Functionalization Mechanistic Investigation

Given the unique selectivity we observe in our aryl ether systems, we investigated the cause of the enhanced *ortho* selectivity. First, it was prudent to ensure that the reaction is *ortho* selective at all time points in the reaction, as we hypothesized that it would possible for the reaction proceed reversibly in the nucleophilic attack. Calculations performed in studies by both Nicewicz and Yoshida show that the site most susceptible to nucleophilic attack should be the *para*-position after radical cation formation.[5,14] If reversibility of nucleophilic attack was important in determining selectivity, early time points may indicate initial formation of the *para*-product as a kinetic product. Our studies showed that even at the earliest time points of reaction, *ortho*- product is the predominant product, indicating that the reaction is likely not reversible after H-atom abstraction. To further prove this conclusion, a reaction using **22-PF$_6$** as substrate and excess 4-methylpyridine as nucleophile showed no shuffling of the pyridinium group between pyridine and 4-methylpyridine, confirming that formation of the final product is not reversible.

We next sought to probe the effects on selectivity from evaluating the various components of the reaction. During these studies, we were surprised to find that removal of all TEMPO from the reaction led to a reversal of selectivity; now giving a combined yield of 51% and selectivity of 1 : 2 *ortho* : *para* (**Table 3.3**. entry 1). Following this result, we ran a screen of different loadings of TEMPO, finding that inclusion of <1 mol% TEMPO caused the reaction to shift back to *ortho* selectivity. This implies that TEMPO is critical to the mechanism that forms predominantly *ortho*-product (entry 2). Further probing of TEMPO loading showed that inclusion of 1 eq. TEMPO gave similar results to the catalytic 20 mol% loading (entry 5), while a large excess of TEMPO drastically cut the combined yield of the reaction while remaining *ortho*- selective (entry 6).

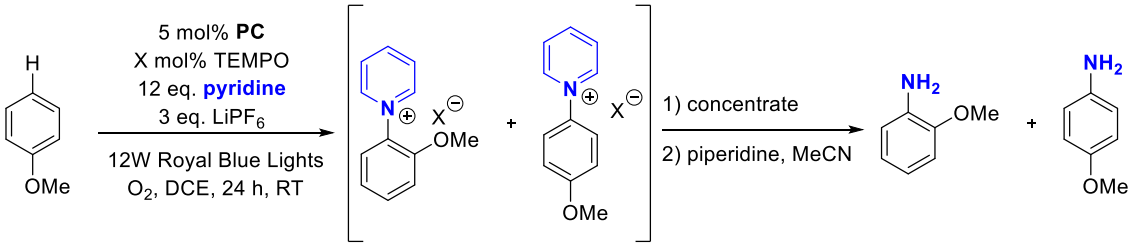

Entry	Loading TEMPO (mol %)	Combined Yield (%)	Selectivity (*ortho*:*para*)
1	0	51	1 : 2
2	<1	65	7 : 1
3	10	92	9 : 1
4	20	94	9 : 1
5	100	99	5 : 1
6	500	30	2 : 1

Table 3.3. Results of the TEMPO loading screen.

To determine if there is a mechanistic difference between the reactions that include or exclude TEMPO, initial rate experiments were investigated to look for a large difference in early stages of the reaction. If the reactions proceed at the same initial rate, it is likely that they also proceed by the same mechanism. In our system, we observe that the rate of the TEMPO-free reaction is slower than that with TEMPO, implying that there is possibly a difference in mechanism (**Figure 3.2.**).

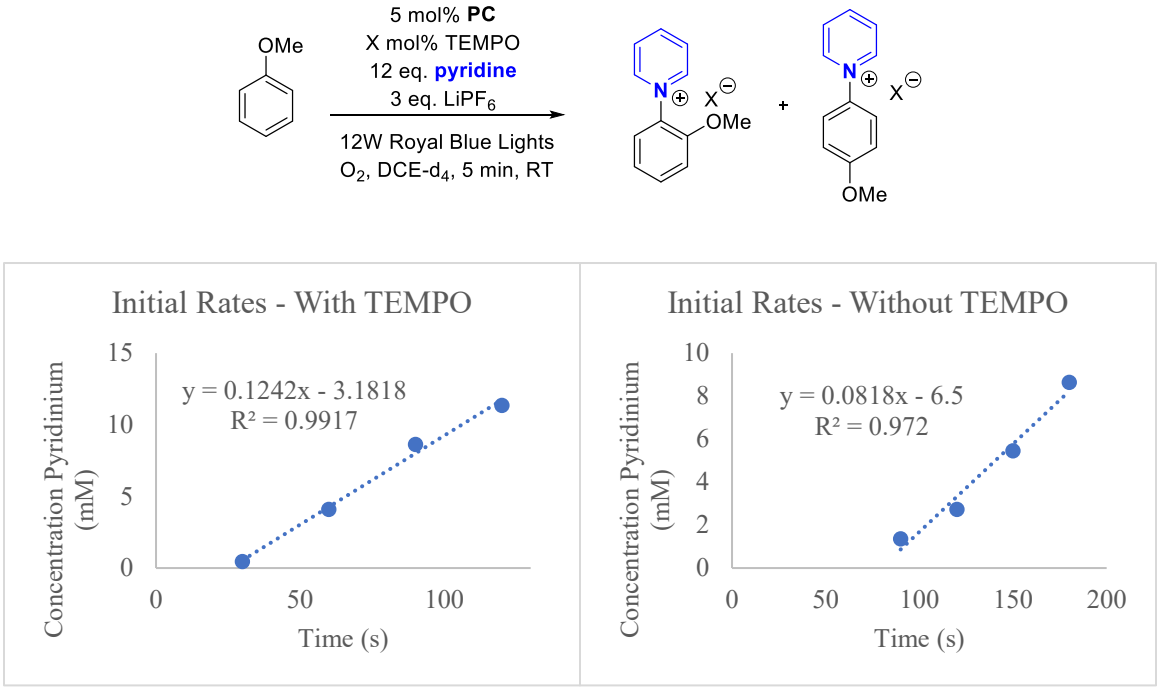

Figure 3.2. Initial rate studies of the photocatalyzed pyridination of anisole in DCE-d_4, both with and without catalytic TEMPO (20 mol%).

To better elucidate the role of TEMPO in this reaction, alternative oxidants were evaluated to determine their effect on selectivity. First, several oxidants tested by Nicewicz were applied to this reaction, using 1 equivalent of oxidant in addition to the O_2 atmosphere. Common oxidants iodosobenzenediacetate ($PhI(OAc)_2$) and potassium persulfate ($K_2S_2O_8$) give moderate combined yields of product and are either *para*-selective or unselective (**Table 3.4.** entries 1-2). We hypothesized that this indicates that *ortho*-selectivity is not tied to merely inclusion of an oxidant, but that the N-oxyl radical character of TEMPO may be tied to this reactivity. We therefore tested N-hydroxyphthalimide (NHPI) and N,N-dihydroxypyromellitimide (NDHPI), which are able to form N-oxyl radicals in solution.[15] These oxidants were tested at 20 mol% loading akin to TEMPO, but were found to give completely unselective mixtures of products (entries 3-4).

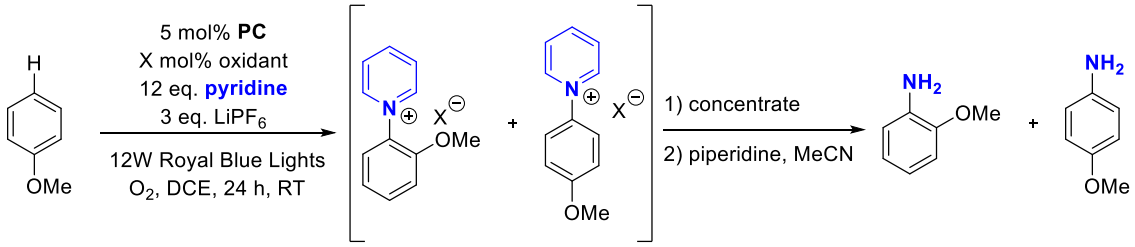

Entry	Oxidant	Loading oxidant (mol %)	Combined Yield (%)	Selectivity (*ortho*:*para*)
1	$PhI(OAc)_2$	100	38	1 : 2
2	$K_2S_2O_8$	100	48	1 : 1
3	NHPI	20	45	1 : 1
4	NDHPI	20	36	1 : 1

Table 3.4. Results of the non-TEMPO type oxidant screen.

As our selectivity seemed tied specifically to inclusion of TEMPO-type N-oxyl radicals, we then investigated a screen of alternative TEMPO derivatives. We hypothesized that adjusting the electronics of the radical could lead to large changes in selectivity for the pyridination by affecting the ability of TEMPO to interact with the substrate. The screen encompassed several TEMPO-type molecules derivatized in the 4-position of the piperidine ring. The effects observed by adjusting these electronics were minimal. (**Table 3.5.** entries 1-5) We next hypothesized that there may be a direct interaction between TEMPO and the substrate, which could lead to ortho selectivity. If such an interaction were occurring, it could potentially be prevented by blocking access to the N-oxyl radical through increased steric bulk. We therefore sought to test cyclohexane-substituted (4-acetamidopiperidin-1-yl)oxyl (CHAMPO), which bears extreme steric bulk around the N-oxyl site.[16] Use of CHAMPO in place of TEMPO had no effect on selectivity or yield of the reaction,

indicating that there was likely not a direct interaction taking place between the TEMPO N-oxyl and the substrate (entry 6).

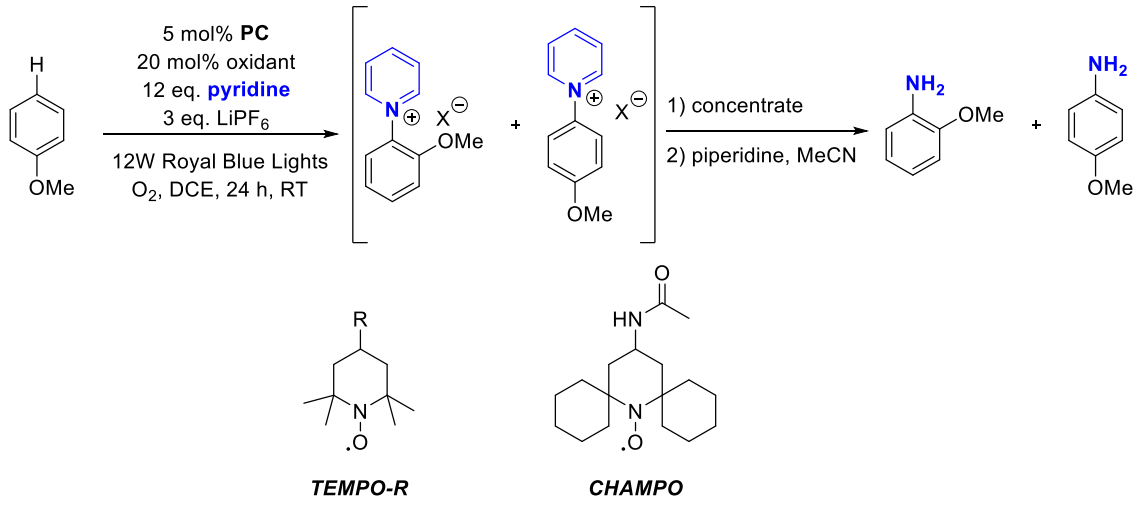

Entry	Oxidant	Combined Yield (%)	Selectivity (*ortho*:*para*)
1	TEMPO-OMe	86	13 : 1
2	TEMPO-OH	90	12 : 1
3	TEMPO-NH_2	81	11 : 1
4	TEMPO=O	87	11 : 1
5	TEMPO-NHAc	92	11 : 1
6	CHAMPO	96	9 : 1

Table 3.5. Results of the TEMPO-type oxidant screen.

Although these mechanistic investigations have given some insight into the role of TEMPO in the C–H functionalization reaction, the role of TEMPO in this reactivity is still not fully understood, and investigations are still underway to determine the source of observed *ortho*-selectivity.

3.3. Conclusion

This chapter describes two methods for the amination of electron rich arenes. The key change to these systems is the use of pyridine, a non-HNR_2 nucleophile to form the C–H bond, which changes the product distribution of this reaction relative to other similar processes. The first method describes a SNAr-type substitution method wherein C–Cl bonds are cleaved following nucleophilic attack on a photochemically derived radical cation by pyridine. The second method describes a method by which C–H bonds are cleaved following nucleophilic attack on a radical cation by pyridine in the presence of an oxidant that can perform H-atom abstraction. The C–H process produces selectivity for *ortho* products which is largely unique for this class of reactions. Investigations are still underway to determine the source of this unique selectivity.

3.4. Experimental Procedures and Characterization

3.4.1. General Experimental

General Experimental

NMR spectra were recorded at room temperature on a Varian Inova 500 (500 MHz for ^1H) NMR spectrometer with the residual solvent peak (CD_3CN: ^1H: δ = 1.94 ppm) as the internal reference. Chemical shifts are reported in parts per million (ppm, δ) relative to tetramethylsilane as an external reference at 0.00 ppm. Multiplicities are reported as follows: s (singlet), d (doublet), t (triplet), q (quartet), hept (heptet), m (multiplet). Coupling constants (*J*) are reported in Hz. Yields in the substrate scope were determined by isolation and concentrations of product in crude reaction mixtures were determined by ^1H NMR. Yields for standard C–H pyridination reactions of anisole were determined by GC-FID using 1,2-dichlorobenzene as standard.

Materials

PC was both purchased from Aldrich and synthesized using a reported synthesis.[17] Compound **14** was synthesized by a reported synthesis.[18] Pyridinium product standards were synthesized using a reported synthesis.[19] Reagents were purchased and used without further purification. $LiPF_6$ (battery grade) was purchased from Oakwood. TEMPO was purchased from TCI. DCE was purchased from Millipore sigma. Pyridine and TFE were purchased from Acros. Substrates and other compounds were purchased from Sigma, Acros, Oakwood, and TCI. DCM, pentane, diethyl ether, and ethanol were purchased from Fisher chemicals. CHAMPO was graciously donated by the group of Song Lin.

Photoreactor

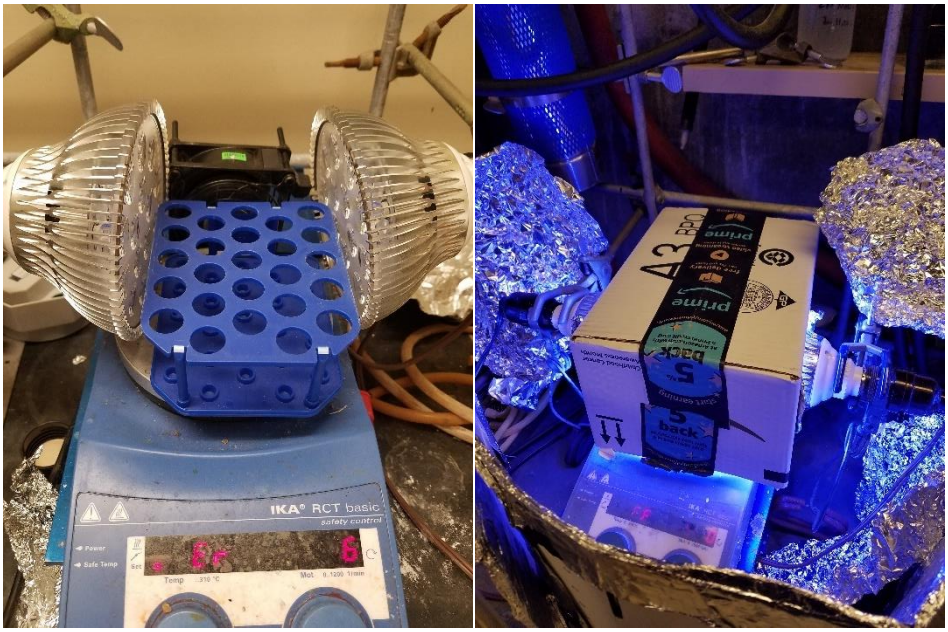

Figure 3.3. Photos of the photochemical setup used in this study displayed with the lights on and with the lights off.

Pictured photoreactor used in all photocatalytic reactions. “ABI 12W Blue LED PAR38 Grow Light for Aquarium and Plant Growth (450-460nm)” lights purchased from Amazon. “AC Infinity AXIAL 8025, Muffin Fan, 120V AC 80mm x 25mm High Speed, for DIY Cooling Ventilation Exhaust Projects” fan purchased from Amazon.

3.4.2. Experimental Procedures

General Procedure for Substitution Reactions

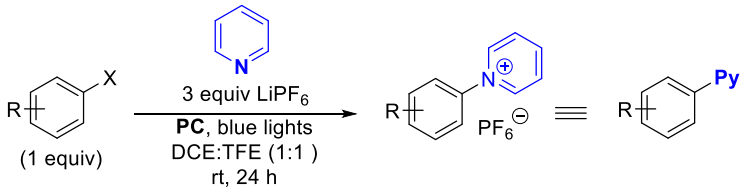

To a 4 mL vial was added **PC** (2.9 mg, 0.005 mmol, 0.05 eq.) followed by $LiPF_6$ (45.6 mg, 0.3 mmol, 3 eq.). A mixture of 1 : 1 DCE:TFE (1 mL) was added followed by pyridine (0.1 mL, 1.24 mmol, 12.4 eq.) then substrate (0.1 mmol, 1 eq.) and a stir bar. The vial was sealed with a septa cap and N_2 was bubbled through the reaction for 2 min. The vial was irradiated with blue light while stirring for 24 h. The reaction mixture was transferred to a 20 mL vial washing with dichloromethane (DCM). The solvent was removed by rotary evaporator, then pentane (7 mL) and water (7 mL) were then added to the vial, then the vial was capped. The vial was then vigorously shaken, breaking up solid by sonication if needed, until a film of solid accumulated at the boundary between the solvents. The mixture was then filtered, washing with copious water and pentane. The solid was then washed through the filter with DCM. This solution was then dried under a stream of nitrogen, adding pentane as the drying occurred to ensure a powdery product. If the product was highly yellow, the solid was re-dissolved in DCM, then triturated with Et_2O. The products were then dried *in vacuo* overnight and were analyzed by ^{1}H-NMR.

Characterization of Substitution Substrate Scope

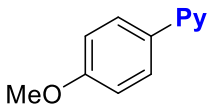

(**2-PF$_6$**)

Product obtained as an off-white solid from the chloride (27.5 mg, 83% yield) and from the fluoride (12.2 mg, 37% yield).

^{1}H NMR (500 MHz, Acetonitrile-d_3) δ 8.86 (d, J = 5.7 Hz, 2H), 8.63 (t, J = 7.9 Hz, 1H), 8.15 (t, J = 7.1 Hz, 2H), 7.63 (d, J = 9.0 Hz, 2H), 7.21 (d, J = 9.1 Hz, 2H), 3.91 (s, 3H).

^{13}C NMR (176 MHz, CD_3CN) δ 165.42, 161.90, 146.18, 144.54, 128.31, 125.80, 115.39, 55.76.

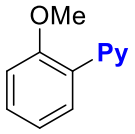

(**3-PF$_6$**)

Product obtained as an off-white solid from the chloride (12.6 mg, 38% yield).

^{1}H NMR (500 MHz, Acetonitrile-d_3) δ 8.82 – 8.74 (m, 2H), 8.67 (tt, J = 7.9, 1.4 Hz, 1H), 8.16 (t, J = 7.1 Hz, 2H), 7.69 (ddd, J = 8.5, 7.5, 1.6 Hz, 1H), 7.55 (dd, J = 7.9, 1.7 Hz, 1H), 7.34 (dd, J = 8.4, 1.2 Hz, 1H), 7.24 (td, J = 7.7, 1.2 Hz, 1H), 3.86 (s, 3H).

^{13}C NMR (176 MHz, cd_3cn) δ 152.12, 147.02, 146.27, 133.31, 131.19, 128.00, 126.41, 121.34, 113.35, 56.26.

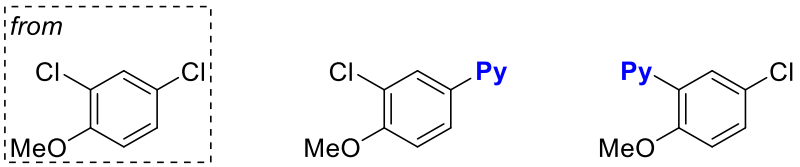

(5-PF_6)

Product obtained in a mixture of products from compound **12** as an off-white solid (27.6 mg, 75% yield, 2.3 : 1 *ortho* **:** *para*). Products matched to independently synthesized standard.

^{1}H NMR (500 MHz, Acetonitrile-d_3) δ 8.86 (d, J = 5.5 Hz, 2H, **10a**), 8.77 (d, J = 5.4 Hz, 2H, **12a**), 8.67 (m, J = 20.4, 7.9 Hz, 1H, **Overlapping**), 8.20 – 8.13 (m, 2H, **Overlapping**), 7.80 (d, J = 2.8 Hz, 1H, **10a**), 7.70 (d, J = 9.0 Hz, 1H, **12a**), 7.63 (d, J = 9.0 Hz, 1H, **Overlapping**), 7.35 – 7.29 (m, 1H, **Overlapping**), 4.01 (s, 3H, **10a**), 3.85 (s, 3H, **12a**).

^{13}C NMR (176 MHz, cd_3cn) δ 157.41, 151.32, 147.58, 146.74, 146.22, 144.68, 135.67, 132.94, 128.39, 128.14, 126.58, 126.29, 125.25, 124.56, 123.06, 114.88, 113.27, 56.70.

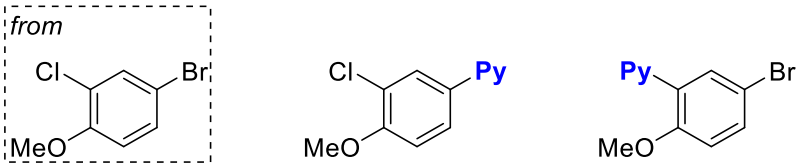

(5-PF_6)

Products obtained as a mixture from as an off-white solid (6 mg, 16%, 3 : 1 Br : Cl). Carbon peaks reported for 4-pyridinated product. Products matched to independently synthesized standard.

^{1}H NMR (500 MHz, Acetonitrile-d_3) δ 8.86 (d, J = 5.4 Hz, 2H, **Br**), 8.76 (d, J = 5.1 Hz, 2H, **Cl**), 8.67 (m, J = 18.6, 7.9, 1.4 Hz, 1H, **Overlapping**), 8.17 (dt, J = 7.8, 6.1 Hz, 2H, **Overlapping**),

7.83 (dd, *J* = 9.0, 2.4 Hz, 1H, **Cl**), 7.80 (d, *J* = 2.8 Hz, 1H, **Br**), 7.75 (d, *J* = 2.4 Hz, 1H, **Cl**), 7.63 (dd, *J* = 9.0, 2.9 Hz, 1H, **Br**), 7.33 (d, *J* = 9.0 Hz, 1H, **Br**), 7.26 (d, *J* = 9.0 Hz, 1H, **Cl**), 4.01 (s, 3H, **Br**), 3.84 (s, 3H, **Cl**).

^{13}C NMR (176 MHz, cd$_3$cn) δ 146.74, 144.68, 135.90, 129.34, 128.38, 128.12, 126.30, 124.55, 113.26, 56.70.

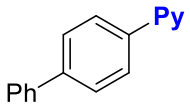

(6-PF$_6$)

Product obtained as an off-white solid from the chloride (39 mg, 99 %).

^{1}H NMR (500 MHz, Acetonitrile-*d*$_3$) δ 8.97 (d, *J* = 5.1 Hz, 2H), 8.69 (tt, *J* = 7.9, 1.5 Hz, 1H), 8.21 (t, *J* = 7.1 Hz, 2H), 7.99 (d, *J* = 8.7 Hz, 2H), 7.81 – 7.74 (m, 4H), 7.55 (t, *J* = 7.6 Hz, 2H), 7.48 (t, *J* = 7.3 Hz, 1H).

^{13}C NMR (176 MHz, cd$_3$cn) δ 146.80, 144.57, 144.19, 141.96, 138.53, 129.22, 128.81, 128.72, 128.46, 127.28, 124.94.

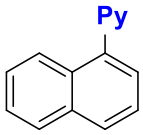

(8-PF$_6$)

Product obtained as an off-white solid from the chloride (22.2 mg, 63 %).

^{1}H NMR (500 MHz, Acetonitrile-*d*$_3$) δ 8.92 (d, *J* = 5.1 Hz, 2H), 8.81 (tt, *J* = 7.9, 1.5 Hz, 1H), 8.29 (dd, *J* = 12.3, 7.9 Hz, 3H), 8.17 (d, *J* = 8.2 Hz, 1H), 7.83 – 7.71 (m, 3H), 7.67 (ddd, *J* = 8.3, 6.8, 1.3 Hz, 1H), 7.31 (dd, *J* = 8.6, 1.1 Hz, 1H).

^{13}C NMR (176 MHz, CD_3CN) δ 147.61, 146.32, 138.77, 134.08, 132.22, 129.08, 128.76, 128.68, 127.98, 127.11, 125.32, 124.47, 120.41.

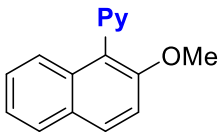

(9-PF_6)

Product obtained as an off-white solid from the chloride (24.5 mg, 64%).

^{1}H NMR (500 MHz, Acetonitrile-d_3) δ 8.84 – 8.76 (m, 3H), 8.33 – 8.26 (m, 3H), 8.07 (d, J = 7.5 Hz, 1H), 7.66 (d, J = 9.3 Hz, 1H), 7.58 (dddd, J = 23.0, 8.1, 6.9, 1.2 Hz, 2H), 7.09 (d, J = 8.4 Hz, 1H), 3.94 (s, 3H).

^{13}C NMR (176 MHz, CD_3CN) δ 151.44, 147.78, 147.54, 133.74, 129.54, 129.00, 128.62, 128.47, 128.40, 125.31, 123.95, 119.02, 113.54, 56.91.

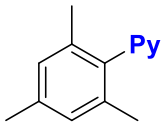

(10-PF_6)

Product obtained as an off-white solid from the chloride (22.0 mg, 64 %).

^{1}H NMR (500 MHz, Acetonitrile-d_3) δ 8.75 (tt, J = 7.9, 1.4 Hz, 1H), 8.70 – 8.66 (m, 2H), 8.29 – 8.21 (m, 2H), 7.19 (s, 2H), 2.39 (s, 3H), 1.96 (s, 6H).

^{13}C NMR (176 MHz, cd_3cn) δ 147.43, 145.96, 141.84, 139.26, 132.77, 129.80, 129.23, 20.13, 16.22.

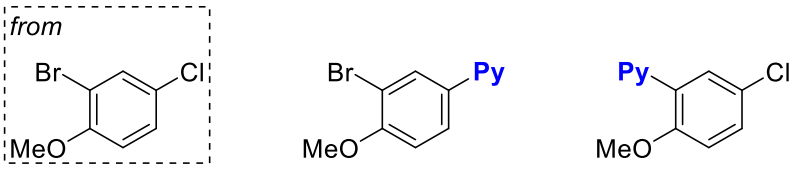

(11-PF_6)

Product obtained as an off-white solid (13.5 mg, 3 : 1 Cl : Br). Carbon peaks reported for 4-pyridinated product. Products matched to similar independently synthesized standard.

^{1}H NMR (500 MHz, Acetonitrile-d_3) δ 8.90 (d, J = 5.1 Hz, 2H, **Cl**), 8.81 (d, J = 5.3 Hz, 2H, **Br**), 8.77 – 8.66 (m, 1H, **Overlapping**), 8.25 – 8.17 (m, 2H, **Overlapping**), 7.99 (d, J = 2.8 Hz, 1H, **Br**), 7.84 (d, J = 2.9 Hz, 1H, **Cl**), 7.73 (ddd, J = 10.8, 9.0, 2.7 Hz, 1H, **Cl**), 7.70 – 7.64 (m, 1H, **Br**), 7.39 – 7.31 (m, 1H, **Overlapping**), 4.04 (d, J = 3.7 Hz, 3H, **Cl**), 3.89 (s, 3H, **Br**).

^{13}C NMR (176 MHz, cd_3cn) δ 158.34, 157.41, 151.32, 147.58, 146.74, 146.22, 144.68, 132.94, 129.26, 128.36, 128.13, 126.58, 126.29, 125.22, 124.55, 114.88, 113.27, 112.97, 56.81, 56.70.

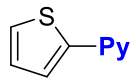

(12-PF_6)

Product obtained as a solid from the chloride (11.2 mg, 36%).

^{1}H NMR (500 MHz, Acetonitrile-d_3) δ 8.93 (dd, J = 6.7, 1.5 Hz, 2H), 8.64 (tt, J = 7.9, 1.4 Hz, 1H), 8.18 – 8.12 (m, 2H), 7.70 (dd, J = 5.5, 1.5 Hz, 1H), 7.59 (dd, J = 3.9, 1.5 Hz, 1H), 7.22 (dd, J = 5.5, 3.9 Hz, 1H).

^{13}C NMR (176 MHz, cd_3cn) δ 149.26, 147.20, 145.01, 128.58, 128.33, 127.35, 125.53.

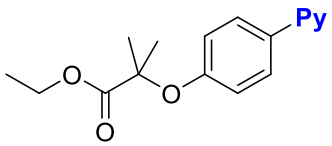

(13-PF$_6$)

Product obtained as an off-white solid from the chloride (26.2 mg, 61%).

^{1}H NMR (500 MHz, Acetonitrile-d_3) δ 8.85 (d, J = 5.3 Hz, 2H), 8.63 (tt, J = 7.8, 1.4 Hz, 1H), 8.18 – 8.11 (m, 2H), 7.58 (d, J = 9.0 Hz, 2H), 7.08 (d, J = 9.0 Hz, 2H), 4.22 (q, J = 7.1 Hz, 2H), 1.65 (s, 6H), 1.23 (t, J = 7.1 Hz, 3H).

^{13}C NMR (176 MHz, cd$_3$cn) δ 172.99, 158.00, 146.33, 144.54, 136.58, 128.36, 125.60, 119.42, 79.82, 61.65, 24.65, 13.32.

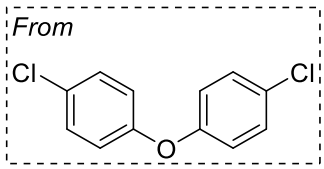

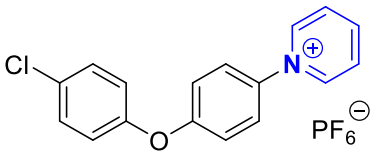

(14-PF$_6$)

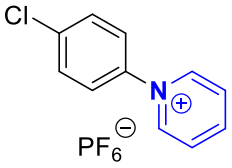

(15-PF$_6$)

Product obtained as an off-white solid (23.3 mg, 12 : 1 **14-PF$_6$** : **15-PF$_6$**)

^{1}H NMR (500 MHz, Acetonitrile-d_3) δ 8.95 (d, J = 5.3 Hz, 2H, **15-PF$_6$**), 8.95 – 8.89 (m, 2H, **14-PF$_6$**), 8.77 – 8.66 (m, 1H, **Overlapping**), 8.26 – 8.18 (m, 2H, **Overlapping**), 7.82 – 7.75 (m, 2H, **15-PF$_6$**), 7.75 – 7.68 (m, 2H, **14-PF$_6$**), 7.54 – 7.49 (m, 2H, **14-PF$_6$**), 7.45 – 7.42 (m, 2H, **15-PF$_6$**), 7.33 – 7.28 (m, 2H, **14-PF$_6$**), 7.20 – 7.15 (m, 2H, **14-PF$_6$**).

^{13}C NMR (176 MHz, cd$_3$cn) δ 159.86, 154.41, 147.14, 146.60, 144.63, 137.91, 137.35, 130.48, 130.26, 129.52, 128.51, 128.42, 126.76, 126.40, 126.32, 121.59, 120.55, 119.17.

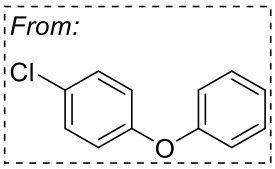

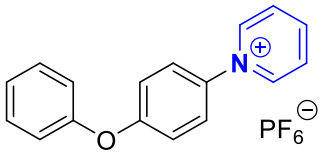

(16-PF$_6$)

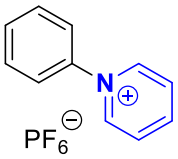

(17-PF$_6$)

Product obtained as an off-white solid (40.3 mg, 99 %, 7.5 : 1 Cl : O(4-ClPh)) Products identified by ^{1}H NMR ratio compared to HRMS(ESI+). ^{13}C reported for **16-PF$_6$**.

^{1}H NMR (500 MHz, Acetonitrile-d_3) δ 8.91 (d, J = 5.5 Hz, 2H, **17-PF$_6$**), 8.87 (d, J = 5.5 Hz, 2H, **16-PF$_6$**), 8.65 (m, J = 7.9 Hz, 1H, **Overlapping**), 8.21 – 8.12 (m, 2H, **Overlapping**), 7.71 (m, J = 20.3 Hz, 4H, **17-PF$_6$**), 7.66 (d, J = 9.0 Hz, 2H, **16-PF$_6$**), 7.51 – 7.45 (m, 2H, **16-PF$_6$**), 7.29 (t, J = 7.4 Hz, 1H, **16-PF$_6$**), 7.24 (d, J = 9.0 Hz, 2H, **16-PF$_6$**), 7.15 (d, J = 7.7 Hz, 2H, **16-PF$_6$**).

^{13}C NMR (176 MHz, Acetonitrile-d_3) δ 160.33, 155.47, 146.51, 144.62, 130.40, 128.40, 126.31, 125.05, 124.48, 120.04, 118.92.

General Procedure for C–H functionalization Reactions

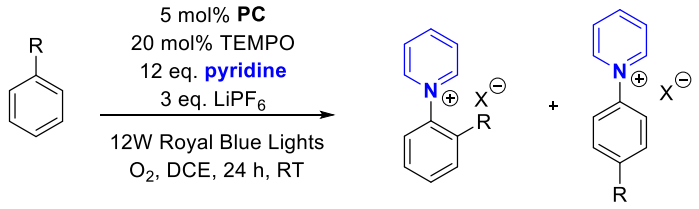

To a 4 mL vial was added TEMPO (3.1 mg, 0.02 mmol, 0.2 eq.), then **PC** (2.9 mg, 0.005 mmol, 0.05 eq.), then $LiPF_6$ (45.6 mg, 0.3 mmol, 3 eq.). DCE (1 mL) was added, followed by pyridine (0.1 mL, 1.24 mmol, 12.4 eq.) then substrate (0.1 mmol, 1 eq.) and a stir bar. The vial was sealed with a septa cap, and O_2 was bubbled through the solution for 1 min. The reaction was then irradiated by blue lights while stirring for 24 h. The reaction was then transferred to a 20 mL vial washing with DCM, then the solvent was removed by rotary evaporator, and a crude ^{1}H NMR was taken to find the selectivity of the reaction. The NMR sample was recombined with the bulk solution and the solvent was again removed by rotary evaporator. Pentane (7 mL) and water (7 mL) were then added to the vial, then the vial was capped. The vial was then vigorously shaken, breaking up solid by sonication if needed, until a film of solid accumulated at the boundary between the solvents. The mixture was then filtered, washing with copious water and pentane. The solid was then washed through the filter with DCM. This solution was then dried under a stream of nitrogen, adding pentane as the drying occurred to ensure a powdery product. If the product was highly yellow, the solid was re-dissolved in DCM, then triturated with Et_2O. The products were then dried *in vacuo* overnight and were analyzed by ^{1}H-NMR.

Characterization of C–H Substrate Scope

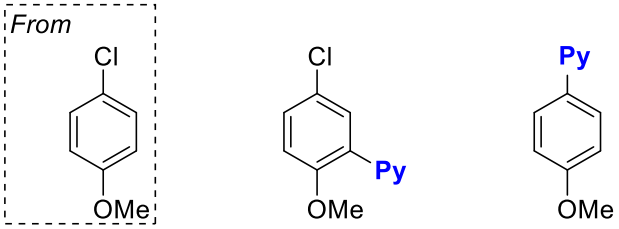

(18-PF_6)

Product mixture was obtained as an off-white powder (18.4 mg, 50%, 5.0 : 1.0). Substitution product observed only in crude reaction mixture.

^{1}H NMR (500 MHz, Acetonitrile-d_3) δ 8.79 – 8.75 (m, 2H), 8.69 (tt, J = 7.9, 1.4 Hz, 1H), 8.20 – 8.15 (m, 2H), 7.70 (dd, J = 9.0, 2.6 Hz, 1H), 7.63 (d, J = 2.6 Hz, 1H), 7.31 (d, J = 9.0 Hz, 1H), 3.85 (s, 3H).

^{13}C NMR (176 MHz, cd$_3$cn) δ 151.31, 147.58, 146.22, 132.94, 131.40, 128.13, 126.58, 125.25, 114.88, 56.71.

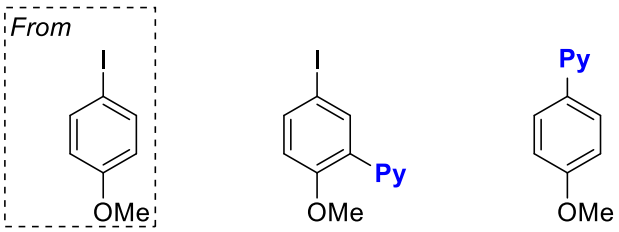

(19-PF_6)

Product mixture was obtained as a mixture as a yellow powder (4.9 mg, 11%, 5 : 1). ^{13}C reported for **C–H product**.

^{1}H NMR (500 MHz, Acetonitrile-d_3) δ 8.87 – 8.85 (m, 2H, **I**), 8.77 – 8.73 (m, 2H, **C–H**), 8.68 (tt, J = 7.9, 1.4 Hz, 1H, **C–H**), 8.62 (t, J = 7.9 Hz, 1H, **I**), 8.16 (dd, J = 7.9, 6.6 Hz, 2H, **Both**), 8.00

(dd, *J* = 8.9, 2.1 Hz, 1H, **C–H**), 7.88 (d, *J* = 2.2 Hz, 1H, **C–H**), 7.65 – 7.59 (m, 2H, **I**), 7.22 – 7.19 (m, 2H, **I**), 7.13 (d, *J* = 8.9 Hz, 1H, **C–H**), 3.91 (d, *J* = 1.9 Hz, 3H, **I**), 3.83 (s, 3H, **C–H**).

^{13}C NMR (176 MHz, cd$_3$cn) δ 152.41, 147.48, 146.18, 141.88, 138.35, 134.90, 128.08, 115.59, 80.97, 56.55.

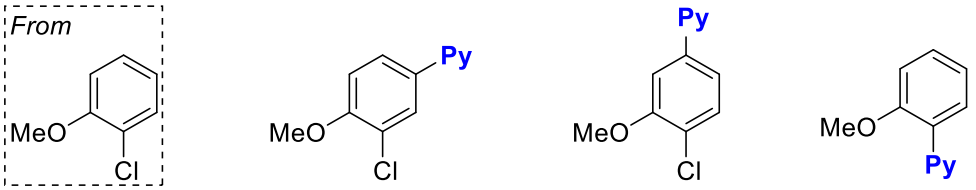

(20-PF$_6$)

Mixture of products obtained as an off-white powder (27.9 mg, 76.4% yield, 3.5 : 1.7 : 1.0 ***p*-OMe : *p*-Cl : Cl**).

^{1}H NMR (500 MHz, Acetonitrile-*d*$_3$) δ 8.92 – 8.89 (m, 2H, ***p*-Cl**), 8.89 – 8.84 (m, 2H, ***p*-OMe**), 8.78 (d, *J* = 5.7 Hz, 2H, **Cl**), 8.72 – 8.59 (m, 1H, **Overlapping**), 8.16 (m, 2H, **Overlapping**), 7.80 (d, *J* = 2.9 Hz, 1H, ***p*-OMe**), 7.70 (dd, *J* = 12.9, 7.8 Hz, 1H, **Overlapping**), 7.63 (dd, *J* = 9.0, 2.9 Hz, 1H, ***p*-OMe**), 7.56 – 7.53 (m, 1H, **Cl**), 7.38 (d, *J* = 2.6 Hz, 1H, ***p*-Cl**), 7.33 (d, *J* = 9.0 Hz, 1H, ***p*-OMe, Cl**), 7.27 – 7.22 (m, 1H, **Overlapping**), 7.16 (dd, *J* = 8.5, 2.6 Hz, 1H, ***p*-Cl**), 7.08 (d, *J* = 8.5 Hz, 1H, ***p*-Cl**).

^{13}C NMR (176 MHz, cd$_3$cn) δ 157.41, 152.12, 147.17, 147.02, 146.74, 146.27, 146.14, 144.73, 144.68, 144.60, 133.31, 131.30, 128.38, 128.22, 128.00, 126.41, 126.29, 124.55, 123.06, 121.34, 115.47, 115.08, 114.93, 113.35, 113.27, 109.45, 108.30, 56.76, 56.70, 56.26.

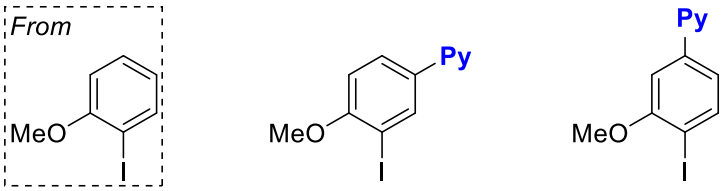

(21-PF_6)

Product mixture was obtained as a mixture as an off-white powder (27.6 mg, 60%, 1.2 : 1.0).

^{1}H NMR (500 MHz, Acetonitrile-d_3) δ 8.93 – 8.88 (m, 2H, ***p*-I**), 8.87 – 8.82 (m, 2H, ***p*-OMe**), 8.69 (t, J = 7.9 Hz, 1H, ***p*-I**), 8.64 (t, J = 7.8 Hz, 1H, ***p*-I**), 8.21 – 8.09 (m, 2H, 1H, **Overlapping**), 7.70 (dd, J = 8.9, 2.9 Hz, 1H, ***p*-OMe**), 7.23 (d, J = 2.5 Hz, 1H, ***p*-I**), 7.19 (d, J = 8.9 Hz, 1H, ***p*-OMe**), 7.07 (dd, J = 8.3, 2.5 Hz, 1H, ***p*-I**), 3.98 (s, 3H, ***p*-OMe**), 3.96 (s, 3H, ***p*-I**).

^{13}C NMR (176 MHz, cd$_3$cn) δ 160.65, 159.53, 147.16, 146.62, 144.65, 144.62, 144.09, 140.73, 136.41, 135.12, 128.40, 128.32, 126.08, 117.96, 111.60, 107.92, 89.06, 85.59, 56.94, 56.94.

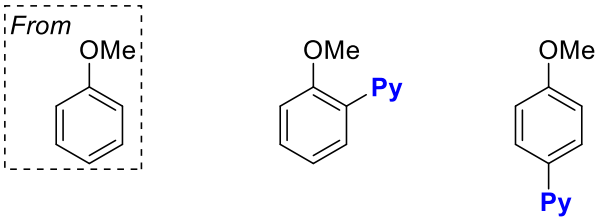

(22-PF_6)

Product mixture obtained as a mixture as an off-white powder. (21.8 mg, 66%, 5.5 : 1 ***ortho*** : ***para***). ^{13}C reported for ***ortho***.

^{1}H NMR (500 MHz, Acetonitrile-d_3) δ 8.88 – 8.85 (m, 2H, ***para***), 8.80 – 8.75 (m, 2H, ***ortho***), 8.67 (tt, J = 7.9, 1.4 Hz, 1H, ***ortho***), 8.65 – 8.60 (m, 1H, ***para***), 8.16 (t, J = 7.1 Hz, 2H, **Both**), 7.69 (ddd, J = 8.8, 7.7, 1.6 Hz, 1H, ***ortho***), 7.64 – 7.60 (m, 2H, ***para***), 7.55 (dd, J = 7.9, 1.6 Hz, 1H,

ortho), 7.34 (d, *J* = 8.4 Hz, 1H, ***ortho***), 7.26 – 7.20 (m, 1H, 2H, **Overlapping**), 3.91 (s, 3H, ***para***), 3.85 (s, 3H, ***ortho***).

^{13}C NMR (176 MHz, cd$_3$cn) δ 152.12, 147.02, 146.27, 133.32, 129.73, 128.00, 126.41, 121.34, 113.35, 56.26.

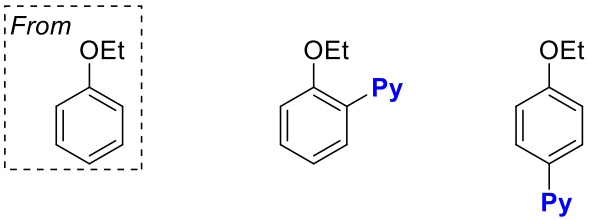

(23-PF$_6$)

Products obtained as a mixture as an off-white solid (23.4 mg, 68%, 5.5 : 1 ***ortho*** : ***para***).

^{1}H NMR (500 MHz, Acetonitrile-*d*$_3$) δ 8.86 (d, *J* = 6.7 Hz, 2H, ***para***), 8.79 (d, *J* = 6.5 Hz, 2H, ***ortho***), 8.67 (td, *J* = 7.9, 1.5 Hz, 1H, ***ortho***), 8.62 (t, *J* = 8.1 Hz, 1H, ***para***), 8.16 (t, *J* = 7.1 Hz, 2H, **Both**), 7.67 (ddd, *J* = 8.9, 7.6, 1.6 Hz, 1H, ***ortho***), 7.61 (d, *J* = 9.1 Hz, 2H, ***para***), 7.55 (dd, *J* = 7.9, 1.6 Hz, 1H, ***ortho***), 7.31 (dd, *J* = 8.5, 1.2 Hz, 1H, ***ortho***), 7.22 (td, *J* = 7.8, 1.2 Hz, 1H, ***ortho***), 7.18 (d, *J* = 9.1 Hz, 2H, ***para***), 4.16 (q, *J* = 6.9 Hz, 2H, **Both**), 1.24 (t, *J* = 7.0 Hz, 3H, **Both**).

^{13}C NMR (176 MHz, cd$_3$cn) δ 151.44, 147.06, 146.97, 146.27, 146.15, 133.26, 131.31, 128.32, 127.93, 127.84, 126.37, 125.78, 121.20, 115.80, 114.10, 65.21, 64.36, 13.90, 13.54.

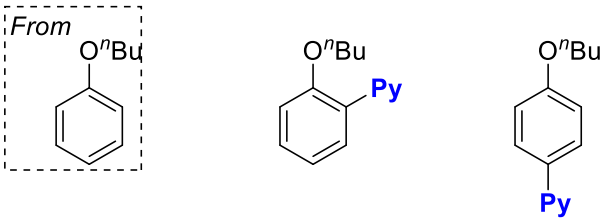

(24-PF$_6$)

Product mixture obtained as a mixture as an off-white powder (26.2 mg, 70%, 6 :1 ***ortho*** : ***para***).

^{13}C reported for ***ortho*** product only.

^{1}H NMR (500 MHz, Acetonitrile-d_3) δ 8.87 – 8.84 (m, 2H, ***para***), 8.80 – 8.75 (m, 2H, ***ortho***), 8.67 (tt, J = 7.9, 1.4 Hz, 1H, ***ortho***), 8.64 – 8.60 (m, 1H, ***para***), 8.16 (t, J = 7.2 Hz, 2H, **Both**), 7.67 (ddd, J = 8.4, 7.6, 1.6 Hz, 1H, ***ortho***), 7.63 – 7.58 (m, 2H, ***para***), 7.55 (dd, J = 7.9, 1.6 Hz, 1H, ***ortho***), 7.31 (dd, J = 8.5, 1.1 Hz, 1H, ***ortho***), 7.22 (td, J = 7.8, 1.2 Hz, 1H, ***ortho***), 7.20 – 7.17 (m, 2H, ***para***), 4.09 (t, J = 6.3 Hz, 2H, **Both**), 1.64 – 1.56 (m, 2H, **Both**), 1.26 (dt, J = 14.8, 7.4 Hz, 2H, **Both**), 0.84 (t, J = 7.4 Hz, 3H, **Both**).

^{13}C NMR (126 MHz, cd$_3$cn) δ 151.63, 147.01, 146.29, 133.27, 127.90, 126.29, 121.16, 114.06, 69.09, 30.42, 18.74, 12.90.

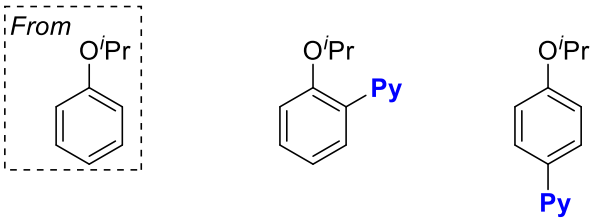

(25-PF$_6$)

Product mixture obtained as a mixture as an off-white powder (24.5 mg, 68%, 9 : 1 ***ortho*** : ***para***).

^{1}H NMR (500 MHz, Acetonitrile-d_3) δ 8.85 (d, J = 6.1 Hz, 2H, ***para***), 8.78 – 8.73 (m, 2H, ***ortho***), 8.67 (tt, J = 7.9, 1.5 Hz, 1H, ***ortho***), 8.62 (t, J = 7.9 Hz, 1H, ***para***), 8.15 (t, J = 7.1 Hz, 2H, **Both**),

7.68 – 7.63 (m, 1H, ***ortho***), 7.61 – 7.57 (m, 2H, ***para***), 7.54 (dd, *J* = 8.0, 1.7 Hz, 1H, ***ortho***), 7.32 (d, *J* = 8.4 Hz, 1H, ***ortho***), 7.21 (td, *J* = 7.8, 1.1 Hz, 1H, ***ortho***), 7.18 – 7.15 (m, 2H, ***para***), 4.74 (hept, *J* = 6.1 Hz, 1H, **Both**), 1.36 (d, *J* = 6.0 Hz, 6H, ***para***), 1.22 (d, *J* = 6.0 Hz, 6H, ***ortho***).

^{13}C NMR (176 MHz, cd$_3$cn) δ 168.61, 151.88, 150.50, 146.94, 146.25, 133.17, 128.31, 127.89, 126.51, 125.80, 121.08, 115.18, 72.26, 71.37, 21.02, 20.84.

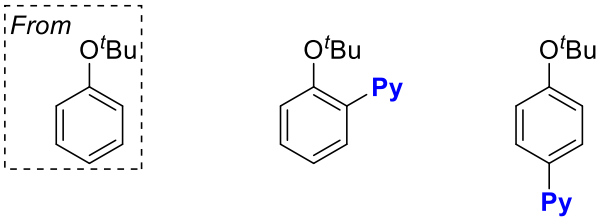

(26-PF$_6$)

Product obtained as a mixture as an off-white powder (29.4 mg, 79% ***ortho*** : ***para***).

^{1}H NMR (500 MHz, Acetonitrile-d_3) δ 8.88 – 8.85 (m, 2H, ***para***), 8.82 – 8.77 (m, 2H, ***ortho***), 8.67 (tt, *J* = 7.9, 1.4 Hz, 1H, ***ortho***), 8.63 (dt, *J* = 7.8, 1.4 Hz, 1H, ***para***), 8.16 (dt, *J* = 8.0, 6.5 Hz, 2H, 2H, **Overlapping**), 7.64 (ddd, *J* = 8.4, 7.5, 1.7 Hz, 1H, ***ortho***), 7.59 (dd, *J* = 8.1, 1.7 Hz, 1H, 2H, **Overlapping**), 7.47 (dd, *J* = 8.4, 1.2 Hz, 1H, ***ortho***), 7.34 (td, *J* = 7.8, 1.3 Hz, 1H, ***ortho***), 7.30 – 7.25 (m, 2H, ***para***), 1.43 (s, 9H, ***para***), 1.20 (s, 9H, ***ortho***).

^{13}C NMR (126 MHz, CD$_3$CN) δ 148.70, 147.10, 146.26, 144.54, 132.61, 128.37, 127.91, 126.46, 125.29, 124.11, 123.45, 122.79, 82.43, 79.32, 27.96, 27.71.

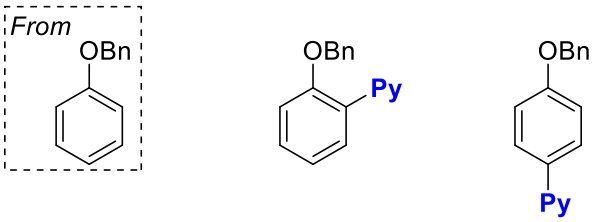

(27-PF_6)

Product mixture obtained as a mixture as an off-white powder (39.3 mg, 97%, 3 : 1 ***ortho*** : ***para***).

^{1}H NMR (500 MHz, Acetonitrile-d_3) δ 8.88 – 8.84 (m, 2H, ***para***), 8.82 – 8.77 (m, 2H, ***ortho***), 8.68 – 8.60 (m, 1H, 1H, **Overlapping**), 8.14 (ddd, J = 8.0, 6.7, 1.9 Hz, 2H, **Both**), 7.69 (ddd, J = 9.0, 7.7, 1.6 Hz, 1H, ***ortho***), 7.64 – 7.60 (m, 2H, ***para***), 7.57 (dd, J = 8.0, 1.6 Hz, 1H, ***ortho***), 7.51 – 7.47 (m, 2H, ***para***), 7.46 – 7.37 (m, **Overlapping**), 7.37 – 7.31 (m, **Overlapping**), 7.29 – 7.23 (m, **Overlapping**), 5.22 (s, 2H, ***para***), 5.19 (s, 2H, ***ortho***).

^{13}C NMR (176 MHz, cd$_3$cn) δ 162.24, 160.90, 151.23, 147.11, 146.28, 146.22, 144.54, 136.46, 135.74, 133.31, 131.70, 128.66, 128.63, 128.34, 128.32, 128.27, 127.96, 127.82, 127.48, 126.50, 125.85, 121.80, 116.25, 114.89, 71.18, 70.30.

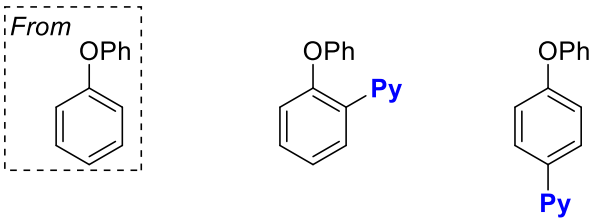

(28-PF_6)

Products obtained as a mixture as an off-white solid (32.1 mg, 82%, 1.5 : 1 ***ortho*** : ***para***).

^{1}H NMR (500 MHz, Acetonitrile-d_3) δ 8.93 – 8.89 (m, 2H, ***ortho***), 8.89 – 8.86 (m, 2H, ***para***), 8.66 (tdt, J = 7.9, 6.4, 1.4 Hz, 1H, **Both**), 8.16 (ddd, J = 7.9, 6.4, 1.3 Hz, 2H, **Both**), 7.66 (dddd, J =

15.2, 8.3, 6.3, 1.6 Hz, 2H, 2H, **Overlapping**), 7.51 – 7.46 (m, 2H, ***para***), 7.44 – 7.38 (m, 3H, ***ortho***), 7.31 – 7.26 (m, 1H, ***para***), 7.26 – 7.22 (m, 1H, 2H, **Overlapping**), 7.17 – 7.13 (m, 2H, ***para***), 7.11 (dd, *J* = 8.4, 1.2 Hz, 1H, ***ortho***), 7.07 – 7.04 (m, 1H, ***ortho***).

^{13}C NMR (176 MHz, CD_3CN) δ 160.33, 155.47, 150.51, 147.38, 146.51, 146.20, 144.62, 133.37, 130.37, 128.40, 128.23, 127.08, 126.31, 125.32, 125.05, 124.12, 120.04, 119.57, 118.92, 118.51.

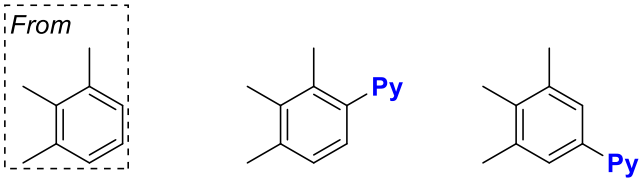

(29-PF_6)

Product was obtained as a mixture as an off-white powder (17.8 mg, 52%, 10 : 1 ***ortho*** : ***para***). ^{13}C reported for ***ortho*** **product**.

^{1}H NMR (500 MHz, Acetonitrile-d_3) δ 8.87 (d, *J* = 6.1 Hz, 2H, ***para***), 8.73 – 8.65 (m, 3H, ***ortho***), 8.63 (t, *J* = 7.8 Hz, 1H, ***para***), 8.18 (t, *J* = 7.1 Hz, 2H, **Both**), 7.34 (s, 2H, ***para***), 7.30 (d, *J* = 8.1 Hz, 1H, ***ortho***), 7.21 (d, *J* = 8.2 Hz, 1H, ***ortho***), 2.41 (s, 3H, **Both**), 2.31 (s, 3H, ***ortho***), 2.30 (s, 3H, ***ortho***), 1.97 (s, 3H, **Both**).

^{13}C NMR (126 MHz, CD_3CN) δ 146.89, 145.82, 140.61, 138.14, 130.82, 128.39, 128.34, 128.31, 122.60, 19.96, 15.36, 13.88.

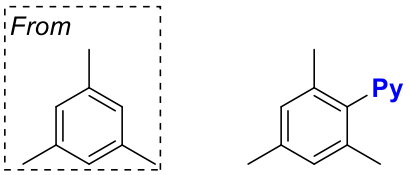

(30-PF_6)

Product obtained as an off-white powder (12.1 mg, 35%).

^{1}H and ^{13}C NMR match reported compound **10-PF_6** above.

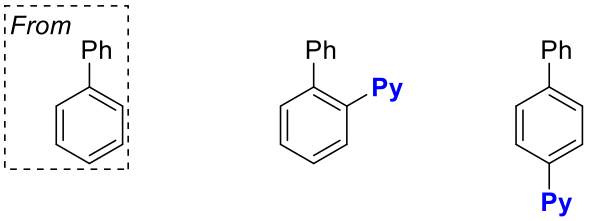

(31-PF_6)

Product obtained as a mixture as an off-white powder (32.1 mg, 85%, 1 : 10 ***ortho*** : ***para***). ^{13}C reported for ***para*** **product**.

^{1}H NMR (401 MHz, Acetonitrile-d_3) δ 9.00 – 8.93 (m, 2H, **Both**), 8.69 (tt, J = 7.8, 1.4 Hz, 1H, ***para***), 8.55 (t, J = 7.8 Hz, 1H, ***ortho***), 8.25 – 8.16 (m, 1H, **Both**), 8.02 – 7.94 (m, 2H, ***para***), 7.83 – 7.73 (m, 2H, **Overlapping**), 7.69 (d, J = 7.5 Hz, 1H, ***ortho***), 7.58 – 7.51 (m, 2H, ***para***), 7.51 – 7.45 (m, 1H, ***para***), 7.33 (t, J = 7.9 Hz, 1H, ***ortho***), 7.14 – 7.09 (m, 1H, ***para***).

^{13}C NMR (126 MHz, cd_3cn) δ 146.80, 144.58, 144.23, 144.19, 138.53, 129.22, 128.81, 128.72, 128.46, 127.28, 124.95.

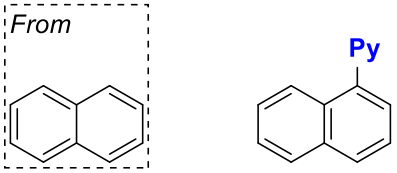

(32-PF_6)

Product obtained as a brown powder. (24.8 mg, 71%).

^{1}H and ^{13}C NMR matches reported compound **8-PF_6** above.

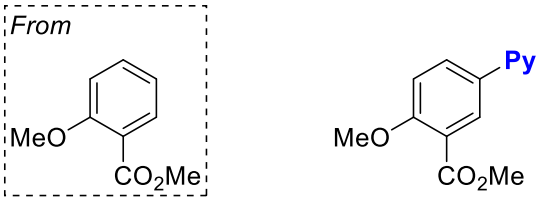

(33-PF_6)

Product obtained as an off-white powder (14.5 mg, 37%).

^{1}H NMR (500 MHz, Acetonitrile-d_3) δ 8.89 – 8.84 (m, 2H), 8.65 (tt, J = 7.9, 1.4 Hz, 1H), 8.16 (t, J = 7.2 Hz, 2H), 8.03 (d, J = 3.0 Hz, 1H), 7.82 (dd, J = 9.0, 3.0 Hz, 1H), 7.38 (d, J = 9.1 Hz, 1H), 3.98 (s, 3H), 3.88 (s, 3H).

^{13}C NMR (176 MHz, cd_3cn) δ 164.90, 160.57, 146.62, 144.70, 135.13, 129.22, 128.39, 127.28, 121.71, 114.05, 56.49, 52.17.

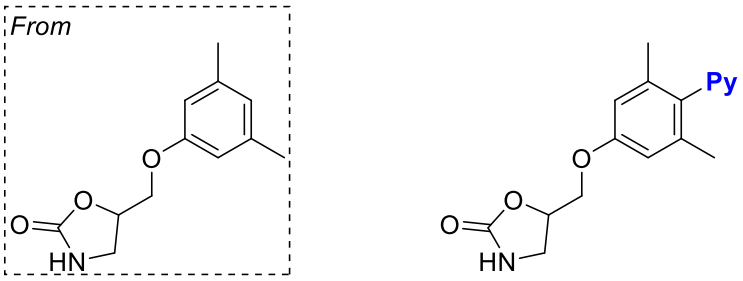

(34-PF_6)

Product obtained as an off-white powder (14.5 mg, 33%).

^{1}H NMR (700 MHz, Acetonitrile-d_3) δ 8.71 (tt, J = 8.0, 1.4 Hz, 1H), 8.66 (d, J = 6.1 Hz, 1H), 8.62 (d, J = 6.2 Hz, 1H), 8.22 – 8.14 (m, 2H), 6.96 (d, J = 7.0 Hz, 2H), 5.24 (s, 1H), 4.72 (ddt, J = 8.9, 5.8, 3.0 Hz, 1H), 4.21 (dd, J = 10.8, 2.6 Hz, 1H), 4.08 (dd, J = 10.8, 3.5 Hz, 1H), 3.48 (t, J = 9.1 Hz, 1H), 3.11 (dd, J = 8.9, 5.5 Hz, 1H), 2.42 (s, 3H), 2.05 (s, 3H).

^{13}C NMR (176 MHz, cd_3cn) δ 158.23, 151.52, 147.37, 146.61, 143.43, 133.97, 128.74, 128.62, 124.02, 111.71, 73.15, 69.38, 41.10, 20.75, 16.01.

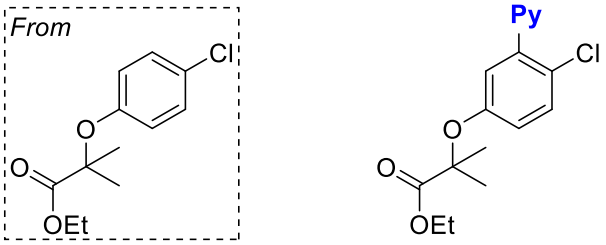

(35-PF_6)

Product obtained as an off-white powder (25.8 mg, 55%).

^{1}H NMR (500 MHz, Acetonitrile-*d*3) δ 8.78 (d, *J* = 5.4 Hz, 2H), 8.71 (t, *J* = 7.9 Hz, 1H), 8.22 – 8.17 (t, 2H), 7.67 (d, *J* = 2.6 Hz, 1H), 7.60 (dd, *J* = 9.1, 2.6 Hz, 1H), 7.10 (d, *J* = 9.1 Hz, 1H), 4.17 (q, *J* = 7.1 Hz, 2H), 1.48 (s, 6H), 1.18 (t, *J* = 7.1 Hz, 3H).

^{13}C NMR (176 MHz, cd_3cn) δ 171.98, 147.72, 147.64, 146.20, 133.55, 132.41, 128.13, 126.99, 126.59, 119.48, 81.91, 61.97, 24.54, 13.25.

General Procedure for C–H functionalization Reactions with Cleavage to Aniline

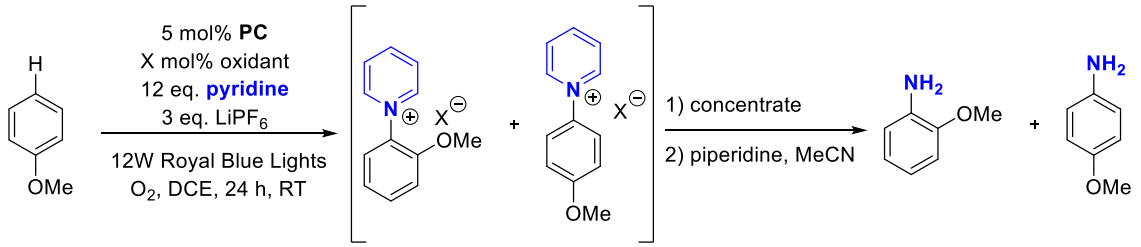

To a 4 mL vial was added TEMPO (3.1 mg, 0.02 mmol, 0.2 eq.), then **PC** (2.9 mg, 0.005 mmol, 0.05 eq.), then $LiPF_6$ (45.6 mg, 0.3 mmol, 3 eq.). DCE (1 mL) was added, followed by pyridine (0.1 mL, 1.24 mmol, 12.4 eq.) then substrate (0.1 mmol, 1 eq.) and a stir bar. The vial was sealed with a septa cap, and O_2 was bubbled through the solution for 1 min. The reaction was then irradiated by blue lights while stirring for 24 h. The reaction was then transferred to a 20 mL vial washing with MeCN, then the solvent was removed by rotary evaporator. The residue was then taken up in MeCN and transferred back to the original reaction vial, at which point piperidine (0.3 mL) was added. The vial was again capped and heated to 80 °C overnight with stirring. The vial was then allowed to cool to room temperature before adding 1,2-dichlorobenzene (10 µL) as standard. The mixture was then passed through a small silica plug, washing with ethyl acetate. The mixture was then analyzed by GC-FID.

Reversibility Experiment Procedure

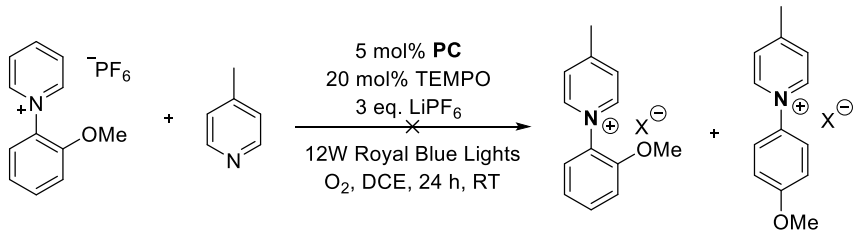

To a 4 mL vial was added TEMPO (3.1 mg, 0.02 mmol, 0.2 eq.), then **PC** (2.9 mg, 0.005 mmol, 0.05 eq.), then $LiPF_6$ (45.6 mg, 0.3 mmol, 3 eq.). DCE (1 mL) was added, followed by pyridine (0.1 mL, 1.24 mmol, 12.4 eq.) then *o*-methoxyphenylpyridinium PF_6 (33.1 mg, 0.1 mmol, 1 eq.) and a stir bar. The vial was sealed with a septa cap, and O_2 was bubbled through the solution for 1 min. The reaction was then irradiated by blue lights while stirring for 24 h. The reaction was then analyzed by mass spectrometry, where no product was observed.

Procedure for Initial Rates Study

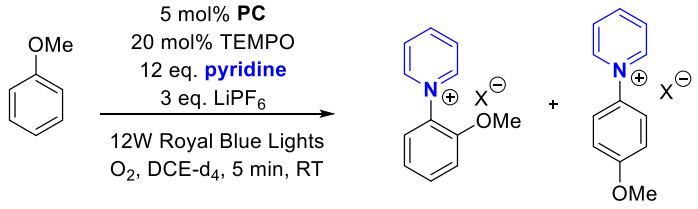

To a 4 mL vial was added TEMPO (3.1 mg, 0.02 mmol, 0.2 eq. or 0 mg, 0 eq.), then **PC** (2.9 mg, 0.005 mmol, 0.05 eq.), then $LiPF_6$ (45.6 mg, 0.3 mmol, 3 eq.). DCE-d_4 (1 mL) was added, followed by pyridine (0.1 mL, 1.24 mmol, 12.4 eq.) then substrate (11 µL, 0.1 mmol, 1 eq.). 1,3,5-trifluorobenzene (10.5 µL) was added as standard. The mixture was then sonicated until maximal solubility of $LiPF_6$ was achieved. Reaction solution (~600 µL) was added to a dry screw-top NMR tube, then capped with a septa cap. O_2 was bubbled through the solution for 1 min, then a ^1H NMR

was taken. The tube was then irradiated with blue light for 30 s, after which a ^{1}H NMR was taken. This process was repeated over the course of 5 minutes of irradiation.

3.5. Reference

[1] Bariwal, J.; Van der Eycken, E. C–N bond forming cross-coupling reaction; an overview. *Chem. Soc. Rev.* **2013**, *42*, 983-9303.

[2] Luo, J.; Wie, W-T. Recent advances in the construction of C–N bonds through coupling reactions between carbon radicals and nitrogen radicals. *Adv. Synth. Catal.* **2018**, *360*, 2076-2086.

[3] Cho, S. H.; Kim, J. Y.; Kwak, J.; Chang, S. Recent advances in the transition metal-catalyzed twofold oxidative C–H bond activation strategy for C–C and C–N bond formation. *Chem. Soc. Rev.* **2011**, *40*, 5068-5083.

[4] Carey, F. A.; Sundberg, R. J. *Advanced Organic Chemistry*, 5th ed.; Springer, 2008.

[5] Tay, N. E. S.; Nicewicz, D. A. Cation radical accelerated nucleophilic aromatic substitution via organic photoredox catalysis. *J. Am. Chem. Soc.* **2017**, *139*, 16100-16104.

[6] Romero, N. A.; Margrey, K. A.; Tay, N. E.; Nicewicz, D. A. Site-selective arene C-H amination via photoredox catalysis. *Science* **2015**, *349*, 1326-1330.

[7] Prier, C. K.; Rankic, D. A.; MacMillan, D. W. C.; Visible light photoredox catalysis with transition metal complexes: applications in organic synthesis. *Chem. Rev.* **2013**, *113*, 5322-5363.

[8] Ohkubo, K.; Mizushima, K.; Iwata, R.; Fukuzumi, S.; Selective photocatalytic aerobic bromination with hydrogen bromide via an electron-transfer state of 9-mesityl-10-methylacridinium ion. *Chem. Sci.* **2010**, *2*, 715-722.

[9] Ohkubu, K.; Fujimoto, A.; Fukuzumi, S.; Photocatalytic monofluorination of benzene by fluoride via photoinduced electron transfer with 3-Cyano-1-methylquinolinium. *J. Phys. Chem. A* **2013**, *117*, 10719-10725.

[10] Lambert

[11] (a) Rössler, S. L.; Jelier, B. J.; Tripet, P. F.; Shemet, A.; Jeschke, G.; Togni, A.; Carreira, E. M.; Pyridyl radical cation for C−H amination of arenes. *Angew. Chem. Int. Ed.* **2018**, *58*, 526-531. (b) Ham, W. S.; Hillenbrand, J.; Jacq, J.; Genicot, C.; Ritter, T. Divergent late-stage (hetero)aryl C−H amination by the pyridinium radical cation. *Angew. Chem. Int. Ed.* **2018**, *58*, 532-536.

[12] Huang, H.; Strater, Z. M.; Rauch, M.; Shee, J.; Sisto, T. J.; Nuckolls, C.; Lambert, T. H.; Electrophotocatalysis with a trisaminocyclopropenium radical dication. *Angew. Chem.* **2019**, *131*, 13452-13456.

[13] Zhang, L.; Liardet, L.; Luo, J.; Ren, D.; Grätzel, M.; Hu, X.; Photoelectrocatalytic arene C–H amination. *Nat. Catal.* **2019**, *2*, 366-373.

[14] For electrochemical C(sp^2)–H pyridination of electron rich arenes, see: Morofuji, T.; Shimizu, A.; Yoshida, J.; Electrochemical C–H amination: synthesis of aromatic primary amines via N-arylpyridinium ions. *J. Am. Chem. Soc.* **2013**, *135*, 5000-5003.

[15] Chen, K.; Jia, L.; Dao, R.; Yao, J.; Wang, C.; Chen, Z.; Li, H.; Theoretical studies on muti-hydroxyimides as highly efficient catalysts for aerobic oxidation. *ChemPhysChem* **2013**, *14*, 179-184.

[16] Siu, J. C.; Parry, J. B.; Lin, S.; Aminoxyl-catalyzed electrochemical diazidation of alkenes mediated by a metastable charge-transfer complex. *J. Am. Chem. Soc.* **2019**, *141*, 2825-2831.

[17] White, A. R.; Wang, L.; Nicewicz, D. A.; Synthesis and Characterization of Acridinium Dyes for Photoredox Catalysis. *Synlett* **2019**, *30*, 827-832.

[18] Ting, R. J.; Milcent, T.; Crousse, B.; Regioselective halogenation of arenes and heterocycles in hexafluoroisopropanol. *J. Org. Chem.* **2018**, *83*, 930-938.

[19] Zeghbib, N.; Thelliere, P,; Rivard, M.; Martens, T.; Microwaves and aqueous solvents promote the reaction of poorly nucleophilic anilines with a Zincke salt. *J. Org. Chem.* **2016**, *81*, 3256-3262.

CHAPTER 4

Formation of Aryl–Isocyanate Bonds by Dehydrogenation and Copper-Mediated Coupling

4.1. Introduction

Aryl isocyanates represent an important class of functional groups and intermediates in both organic synthesis and materials chemistry. Further functionalization from these compounds leads to the formation of ureas and carbamates, which serve as common motifs in pharmaceuticals, agrichemicals, and in polyurethane polymers.[1,2,3] Traditional syntheses of aryl isocyanates rely on forcing reaction conditions and/or extremely toxic reagents such as phosgene.[4] Thus, there is a driving interest in developing new methods to form aryl isocyanates. We aimed to develop a new approach to isocyanate formation that does not rely on these toxic reagents through two avenues: metal-catalyzed dehydrogenation of formanilides and metal-catalyzed isocyanation through discrete copper(I) complexes.

4.1.1. Background: Metal Catalyzed Dehydrogenation

Metal catalyzed dehydrogenation is a useful technique for atom economical conversion from alkanes to alkenes, alcohols to ketones and aldehydes, and amines to imines. These reactions produce minimal waste, as they form only the desired product and hydrogen gas as the by-product.

To develop an effective catalyst for forming isocyanates from formanilides, we took inspiration from catalysts used for the dehydrogenation of related classes of substrates (**Figure 4.1.**).

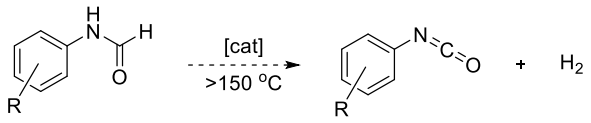

Figure 4.1. Desired dehydrogenative transformation from formanilides to aryl isocyanates.

Early examples of alkane dehydrogenation described iridium– or rhenium–phosphine based complexes to dehydrogenate linear and cyclic alkanes to their respective alkenes.[5,6,7] These reactions were not catalytic, but were some of the first to describe the necessity of including a hydrogen acceptor to help drive the dehydrogenation through transfer hydrogenation. More modern examples utilize iridium catalysts bearing pincer ligands, which operate at low catalyst loadings, but are still driven by inclusion of hydrogen acceptor molecules to provide a sink for the hydrogen.[8] Common pincer ligand scaffolds include PCP and POCOP ligands (**Figure 4.2.**), which bear tunable steric bulk on their phosphine components. Work by Goldman, Jensen, and others has illustrated their efficacy while driving the development of a wide variety of pincer ligands.[9,10,11,12]

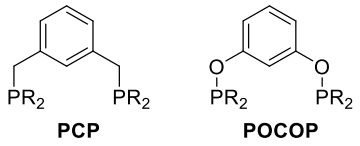

Figure 4.2. General structure of PCP and POCOP ligands.

The dehydrogenation of alcohols to ketones has also been well studied. These reactions often rely on ruthenium-based catalysts at low catalyst loadings, many of which require the use of a base to promote an initial deprotonation event. However, some examples have been reported that avoid this requirement.[13] Early examples used simple catalysts such as $RuCl_2(PPh_3)_3$, which operated

base free but required the use of temperatures as high as 150 °C.[14] Another example is work by Shvo and coworkers, who describe a unique di-ruthenium bridged complex capable of efficient alcohol dehydrogenation.[15] Modern examples of ruthenium-catalyzed alcohol dehydrogenation rely on pincer-type ligands, described by Beller and coworkers to generate over 8000 turnovers per hour (**Figure 4.3.**).[16] Beller also describes the use of several other effective ruthenium and iridium catalysts bearing pincer ligands for the acceptorless dehydrogenation of alcohols in this study.

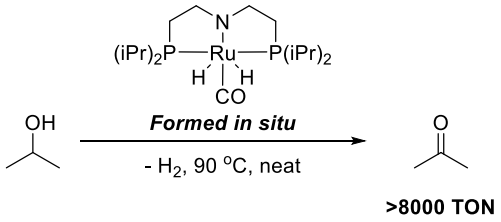

Figure 4.3. Conditions described by Beller and coworkers for alcohol dehydrogenation.

Dehydrogenation of amines to form imines is the closest in concept to our overall goal of synthesizing aryl isocyanates from formanilides, as these studies also detail formation of a C–N double bond. Iridium catalysts are commonly reported for these transformations, both bearing pincer ligands and cyclopentadienyl (Cp) ligands.[17] Jensen describes an iridium pincer catalyst capable of dehydrogenation of amines to imines in high yields, although it is limited to alkyl amines (**Figure 4.4.**).[18] Generally, these reports do not target imines as the final product, but rather propose imines derived from dehydrogenation as intermediates in transamination reactions.[19] We took inspiration from each of these types of dehydrogenation reactions to guide our catalyst selection for formanilide dehydrogenation.

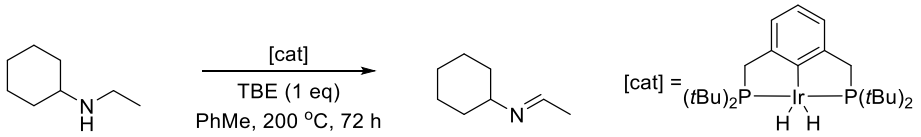

Figure 4.4. Amine dehydrogenation conditions described by Jensen and coworkers.

4.1.2. Background: Metal Catalyzed Isocyanation

One proven method of installing the isocyanate group is through metal catalysis, generally through a cross-coupling type mechanism. These reactions use cyanate salts to form aryl isocyanates *in situ,* but all rely on further reaction to generate either a carbamate or urea to stabilize the highly reactive product. Early work by Baghersad and coworkers detailed the copper-catalyzed coupling of aryl boronic acids and potassium cyanate to form aryl carbamates.[20] Later work by Ma and coworkers expanded this methodology to couple aryl halides with potassium cyanate to form either carbamates or ureas.[21,22] These studies report high yields of their respective products and utilize a cyanate starting material, but do not undertake any mechanistic investigation to confirm the presence of an isocyanate in solution. Contrary to the lack of mechanistic investigation in copper catalysis, Buchwald and coworkers describe a palladium-catalyzed system for the coupling of aryl (pseudo)halides and sodium cyanate, ultimately leading to unsymmetrical ureas.[23] Buchwald independently synthesized a discrete Pd–NCO complex, which then stoichiometrically coupled with an aryl halide to form the isocyanate. We aim to synthesize discrete Cu–NCO complexes to investigate the mechanism of the copper-catalyzed coupling, and to design new copper catalysts that are more efficient for the transformation.

We selected N-heterocyclic carbene (NHC) type and cyclic alkyl amino carbene (CAAC) type ligands to target discrete Cu–NCO complexes, as Cu(I)–carbene complexes have been shown to be stable and can also be applied under catalytic conditions.[24] One example from our lab detailed the copper-catalyzed difluoromethylation of aryl halides, where the copper catalysts bear NHC ligands.[25] By independently synthesizing discrete copper difluoromethyl complexes and studying their reactivity both stoichiometrically and catalytically, they were able to propose a reasonable mechanism for functional group installation. We aim to synthesize similar complexes for our study of isocyanation.

4.2. Results and Discussion

4.2.1. Dehydrogenation

Our early reactions were inspired by the conditions originally described by Porzi and coworkers. The reactions were conducted in neat substrate, originally 4-methoxyformanilide, with 3 mol % $RuCl_2(PPh_3)_3$ at 150 °C (**Figure 4.5.**). Unlike the work by Porzi, our substrate is a solid, and although the substrate melted at this temperature, crystallization of unreacted substrate at the top of the vial proved a consistent challenge. To rectify this, reactions were run fully submerged in a sand bath at 150 °C, at which point product was observable by GC-FID analysis.

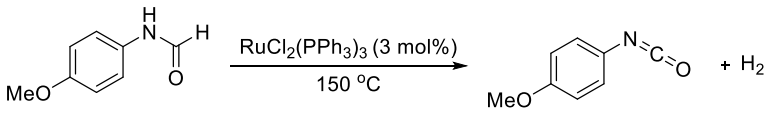

Figure 4.5. Reaction conditions used for initial dehydrogenation reactions.

GC-MS analysis of our product mixture showed the formation of a significant amount of aniline product along with isocyanate, and it was determined that these products of the reaction with 4-methoxyformanilide are inseparable by GC-FID. We therefore switched to 4-*t*-butylformanilide, whose products separated on GC-FID, to determine the product distribution. Analysis of the product mixtures from the new substrate showed a nearly 1 : 1 ratio of isocyanate to aniline product. Other catalysts were tested to determine if aniline formation could be reduced through alternative ligands or by switching to an iridium-based catalyst. We evaluated this new set of catalysts at low loadings, as some reports of alcohol dehydrogenation showed enhanced yields at low concentrations of catalyst. None of the catalysts tested here afforded less aniline relative to $RuCl_2(PPh_3)_3$, with two ruthenium catalysts, Ru-MACHO-BH and $RuH_2(PPh_3)_4$ producing significantly more aniline (**Table 4.1.**, entries 4-5).

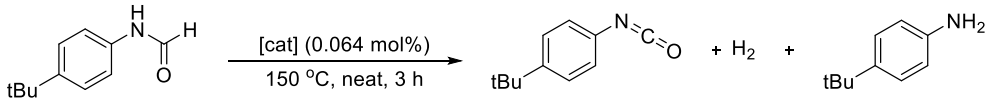

Entry	Catalyst	TON Isocyanate	TON Aniline
1	$RuCl_2(PPh_3)_3$	6.0	5.9
2	$(^{iPr}POCOP)IrH_2$	4.7	8.4
3	$(^{iPr}POCOP)Ir(CO)$	4.5	13.9
4	Ru-MACHO-BH	4.8	21.2
5	$RuH_2(PPh_3)_4$	4.7	18.0
6	$[RuCl_2(C_6H_6)]_2$ + dppe	3.0	4.7

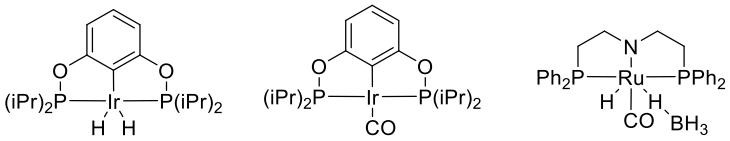

$(^{iPr}POCOP)IrH_2$ $(^{iPr}POCOP)IrCO$ Ru-MACHO-BH

Table 4.1. Dehydrogenation of 4-t-butylformanilide at low catalyst loading.

We next attempted stoichiometric studies to better understand the catalytic cycle, and importantly to understand the source of the aniline product. Generally, isocyanates are unstable to water, which promotes hydrolysis of the isocyanate to aniline. In our case, however, the aniline was observable even in dry solvent and under an inert atmosphere, precluding hydrolysis as the source of aniline. An initial reaction conducted with stoichiometric $RuCl_2(PPh_3)_3$ showed a large shift in the ^{31}P NMR spectrum, from a single singlet peak representing the three equivalent phosphines to a spectrum showing two doublets corresponding to two bound phosphines and a singlet peak corresponding to free PPh_3 (**Figure 4.6.**). This result suggests that the Ru center has lost one phosphine and that a new ligand is likely filling that open site. Analysis of the reaction

solution by IR spectroscopy showed the presence of a Ru–CO bond, suggesting that decarbonylation is likely the source of aniline product.

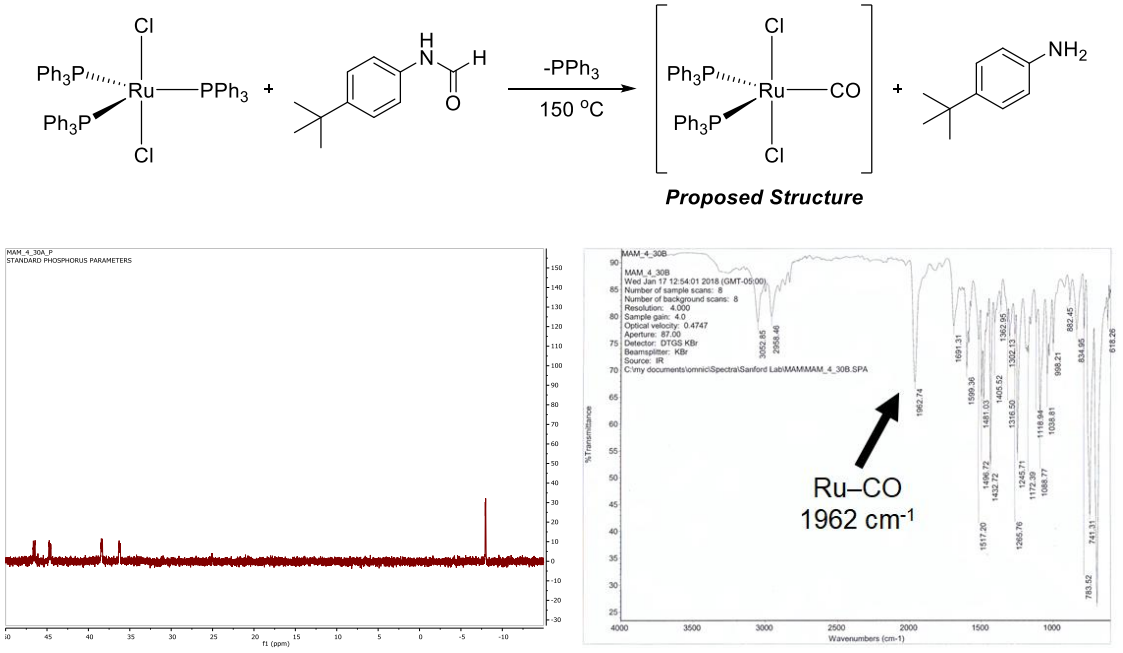

Figure 4.6. ^{31}P NMR and FTIR spectra from the stoichiometric study.

With the knowledge that decarbonylation is a likely avenue of undesired reactivity, we changed the conditions from a neat reaction to one using mesitylene as solvent, hypothesizing that further reducing the concentration of catalyst in solution could help to prevent decomposition. While we found that inclusion of mesitylene did not change the yield of the reaction significantly, we still opted to include it in further reactions. Next, reactions were run under reflux rather than a closed vial to give the CO formed a chance to escape, rather than permanently binding to the ruthenium center. Running the reaction in an open system had a small positive effect on the yield, but decarbonylation to aniline was still observed.

We next sought to evaluate a larger array of catalysts based upon those applied in the literature. This new set of catalysts was tested at 1 mol % catalyst under reflux conditions in

mesitylene. None of the tested catalysts resulted in less aniline formation relative to isocyanate (**Table 4.2.**), and Ru-MACHO-BH was found to be extremely active for decarbonylation chemistry (**Table 4.2.** entry 4). The addition of strong base, which is commonly used throughout the dehydrogenation literature, was also tested with several of the catalysts listed in **Table 4.2.**, but only decomposition of starting material was observed. No catalyst tested proved more effective than $RuCl_2(PPh_3)_3$, and therefore further experimentation continued its use.

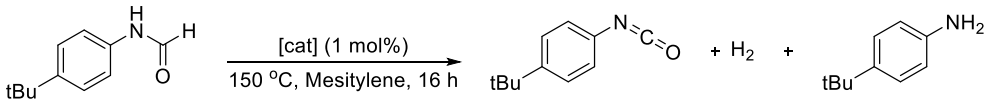

Entry	Catalyst	Yield Isocyanate (%)	Yield Aniline (%)
1	$RuCl_2(PPh_3)_3$	7.2	3.6
2	Ru(triphos)(OAc)Cl	4.7	5.6
3	$RuCl_2(CO)_2(phen)$	0.1	1.0
4	Ru-MACHO-BH	0.0	45.9
5	Ru-^{iPr}MACHO-BH	3.9	1.3
6	Ru-^{Cy}MACHO-BH	2.4	1.8
7	Cp*Ir(py-O)Cl	2.6	7.9

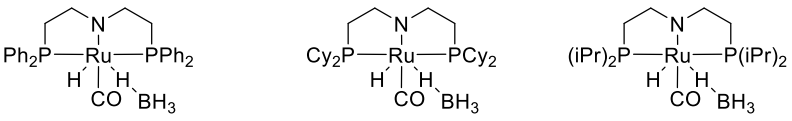

Ru-MACHO-BH Ru-^{Cy}MACHO-BH Ru-^{iPr}MACHO-BH

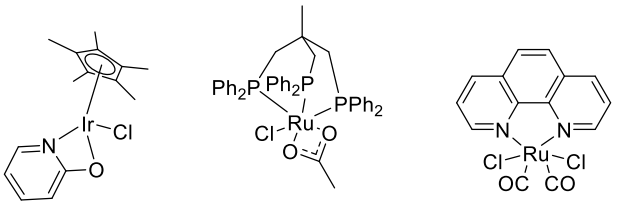

Cp*Ir(py-O)Cl Ru(triphos)(OAc)Cl $RuCl_2(CO)_2(phen)$

Table 4.2. Catalysts tested for dehydrogenation of 4-*t*-butylformanilide under reflux conditions.

Next, the effect of added carbon monoxide gas (CO) was examined on the system. We hypothesized that one of two outcomes may occur: either the added CO will disfavor the decarbonylation process through Le Chatelier's principle, or the added CO will more quickly deactivate the catalyst, leading to a loss of reactivity. Reactions were run both under reflux conditions and in closed vials, where CO was bubbled through the solution. When CO was added to the reaction, we observed that the solution, which is normally yellow in color, quickly changed to colorless at which time all reaction ceased. Ru-MACHO-BH was also tested, as it contains a CO already occupying a site on the Ru center and therefore may not deactivate upon CO addition, but the inclusion of CO in the reaction only had the effect of enhancing decarbonylation further. We therefore determined that if a catalyst was at all active in decarbonylation, it would likely not be appropriate for dehydrogenation of formanilides.

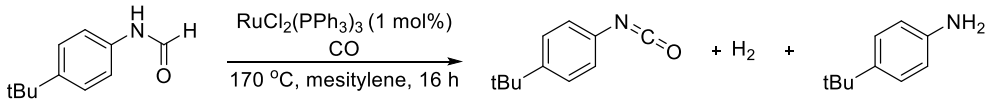

Entry	CO Addition	Yield Isocyanate (%)	Yield Aniline (%)
1	Bubbled, closed vial	0.4	0.5
2	Balloon, closed vial	1.1	0.6
3	Balloon, reflux	5.4	2.4

Table 4.3. Results of dehydrogenation reactions performed in the presence of CO.

4.2.2. Copper Coupling Results

Initial efforts to synthesize (carbene)Cu–NCO complexes targeted the commercially available 1,3-bis(2,6-diisopropylphenyl)imidazol-2-ylidene (IPr) ligand. Work by our lab has

demonstrated the synthesis of unique IPrCu(CHF_2) complexes starting from IPrCuCl, which served as a template for our synthesis.[25] Following an ion exchange with NaO^tBu, transmetallation of the resultant $IPrCuO^tBu$ with trimethylsilylisocyanate (TMSNCO) afforded the desired IPrCuNCO complex. Due to the lack of diagnostic nuclei for NMR spectroscopic characterization, we turned instead to FTIR to confirm the presence of the –NCO functional group. After observing a strong sharp stretch at 2228 cm^{-1}, indicative of an isocyanate, an x-ray quality crystal was obtained to confirm the structure of this new complex (**Figure 4.7.a**).

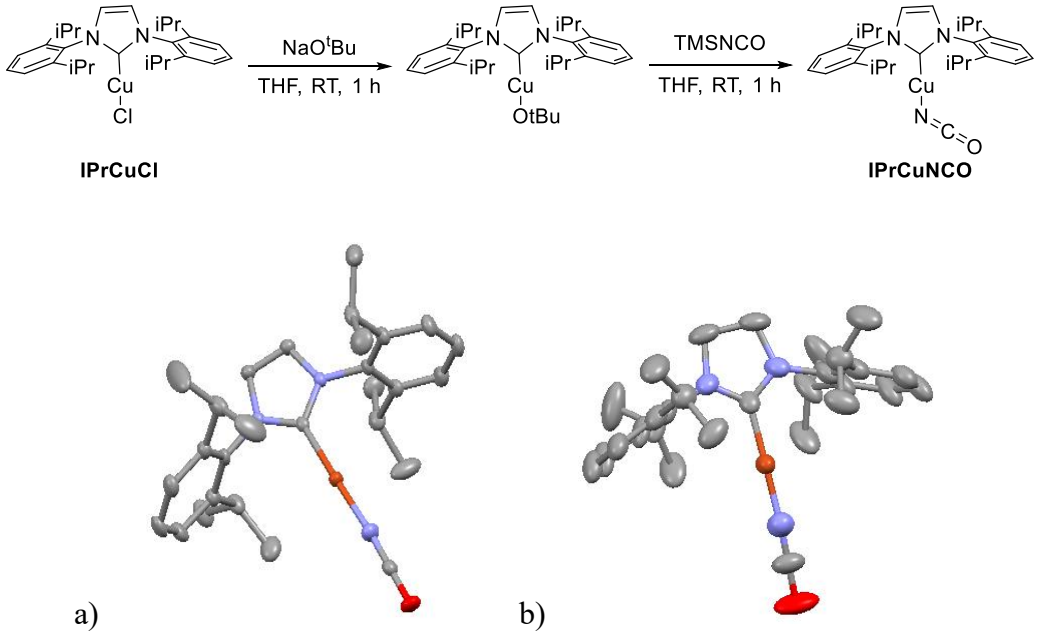

Figure 4.7. Synthesis of IPrCuNCO and the crystal structures obtained after synthesis of a) IPrCuNCO and b) SIPrCuNCO.

With this new complex in hand, stoichiometric cross-coupling chemistry was attempted with aryl iodides using a method similar to the previous difluoromethylation study. Initial tests were attempted by heating a slight excess of IPrCuNCO with 4-iodobenzonitrile in toluene at 90 °C overnight. Under these conditions, no coupling was observed. Even when the solvent was changed to mesitylene or MeCN, or when temperature was increased, no coupling was observed.

As IPrCuNCO appeared to be unreactive with aryl iodides, we next sought to change the ligand to an NHC that was either more electron donating or less sterically demanding. Therefore, Cu–NCO complexes bearing 1,3-bis(2,6-diisopropylphenyl)-4,5-dihydroimidazol-2-ylidene (SIPr) and 1,3-bis(2,4,6-trimethylphenyl)imidazol-2-ylidene (IMes) were synthesized. An x-ray quality crystal was obtained of SIPrCuNCO (**Figure 4.7.b**), while the other complex was analyzed solely by FTIR. SIPrCuNCO was found to be the most electron rich example with an –NCO stretch of 2220 cm^{-1}, while IMesCuNCO was found to be intermediate, with an –NCO stretch of 2223 cm^{-1}. These electronic and steric differences between the compounds were not found to have any effect on reactivity, as cross coupling was not observed with aryl iodides under any conditions for any NHC bearing complex, yielding only unreacted starting material.

We hypothesized that because of the similarity of the complexes to the difluoromethylation study, the desired coupling reaction would likely follow a similar mechanism. This mechanism would require initial oxidative addition of the aryl iodide to the Cu^{I} center, producing (NHC)Cu^{III}(NCO)(Ar)(I). To drive this addition, we hypothesized that we would need an extremely electron rich copper center. To achieve this, we next targeted a Cu–NCO complex bearing [2-[2,6-bis(1-methylethyl)phenyl]-3,3-dimethyl-2-azaspiro[4.5]dec-1-ylidene] (^{Cy}CAAC), which is considerably more electron donating than IPr or SIPr.[26] Synthesis and purification of this compound proceeded similarly to the IPr variant (**Figure 4.8.**), and FTIR showed that this complex was indeed much more electron rich, with an –NCO stretch of 2210 cm^{-1}. An x-ray quality crystal of (^{Cy}CAAC)CuNCO was obtained, and this confirmed its structure and similarity to the NHC complexes.

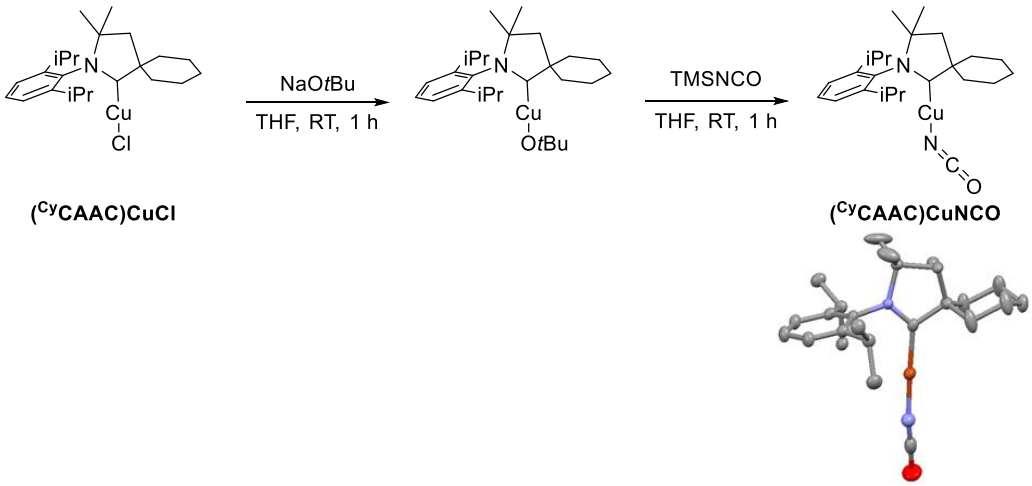

(CyCAAC)CuCl (CyCAAC)CuNCO

Figure 4.8. Synthesis of (^{Cy}CAAC)CuNCO and its crystal structure.

Use of this new complex under all of the previously examined isocyanation conditions originally showed no formation of isocyanated product. Even when the reaction was attempted with directed substrate 2-(2-bromophenyl)pyridine, no product was observed. Coupling reactions using (^{Cy}CAAC)CuNCO in alcohol solvent (used in an attempt to trap any transient isocyanates as carbamates) were also unsuccessful. The alcohol solvent promoted decomposition of the copper complex, and oxidized ^{Cy}CAAC was observable in solution by GC-MS.

As no reactivity was observed in more traditional copper mediated two-electron cross-coupling conditions, a one-electron method was next examined. In a study by Bao and coworkers, bisbenzoyl peroxides were used in the formation of allyl C–O bonds through thermal cracking of the peroxide to generate benzoyl radicals. These radicals then bound to a Cu^{I} center along with an allyl radical to oxidize the metal to Cu^{III}. This Cu^{III} then underwent reductive elimination to yield the desired C–O bond and Cu^{I}. Additionally, in a previous study, our lab reported that bis(4-fluorobenzoyl) peroxide can undergo thermolytic decarboxylative decomposition to relesae aryl radicals that add to a Ni^{III} center.[27] We sought to use this concept to oxidize our Cu^{I} to Cu^{II} while retaining –NCO and –Ar bonds. We hypothesized that this complex could then be further oxidized

to Cu^{III}, which would then undergo reductive elimination to form Ar–NCO. We first aimed to observe the Cu^{II} intermediate through reaction with just one equivalent of the peroxide (**Figure 4.9.**).

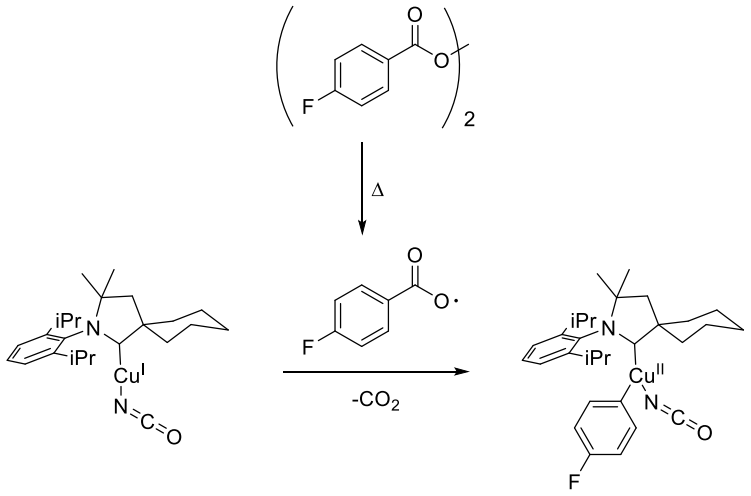

Figure 4.9. Proposed reaction of (^{Cy}CAAC)Cu(NCO) with bis(4-fluorophenyl) peroxide.

Reaction of (^{Cy}CAAC)CuNCO and bis(4-fluorobenzoyl) peroxide proved fruitful in oxidizing the metal center to Cu^{II}, as we observed a color change from colorless to blue upon heating of the mixture. ^{19}F NMR spectroscopic analysis of this blue solution revealed the formation of a new fluorinated product along with starting material and homo-coupled arene product, which indicated the formation of aryl radicals. ^{1}H NMR spectroscopy, which would normally show paramagnetic broadening in the presence of Cu^{II}, displayed peaks more consistent with a diamagnetic sample. This observation led us to hypothesize that a symmetric dimer complex was being formed, which could produce a diamagnetic NMR spectrum. An X-ray quality crystal was obtained to determine the structure of this complex. As shown in **Figure 4.10.**, this revealed the formation of a Cu paddlewheel structure.

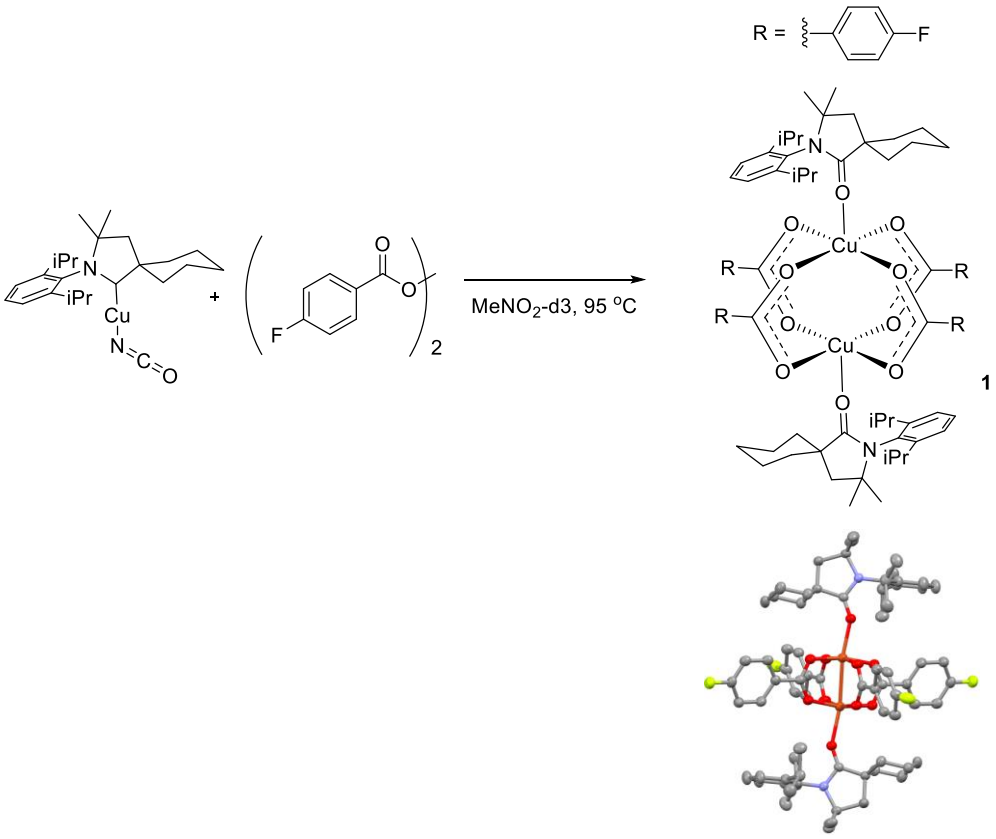

Figure 4.10. Resultant complex of the oxidation of (^{Cy}CAAC)CuNCO with bis(4-fluorobenzoyl) peroxide.

The X-ray structure shows loss of –NCO from the copper centers. Additionally, an oxygen atom has been inserted between the copper centers and ^{Cy}CAAC ligands. We hypothesize that the peroxide promotes CAAC oxidation to generate a cyclic amide that serves as an L–type ligand by binding through a carbonyl oxygen. The related oxidation of carbene ligands has been studied by Ollevier and coworkers, who observed the conversion of NHC ligands to their oxidized form in the presence of Cu^{I} and oxidant.[28] To confirm the binding mode of these ligands, excess pyridine was added to the solution of **1** in an effort to displace the oxidized ^{Cy}CAAC ligands. Crystal growth of the resultant solution yielded complex **2** (**Figure 4.11.**), showing that the pyridine was indeed able to displace the oxidized ^{Cy}CAAC. Notably, the oxidized CAAC was observed in solution by

GC-MS. Reaction of IPrCuNCO under analogous conditions yielded a similar blue solution, leading us to the conclusion that these (carbene)CuNCO complexes are not stable to peroxides.

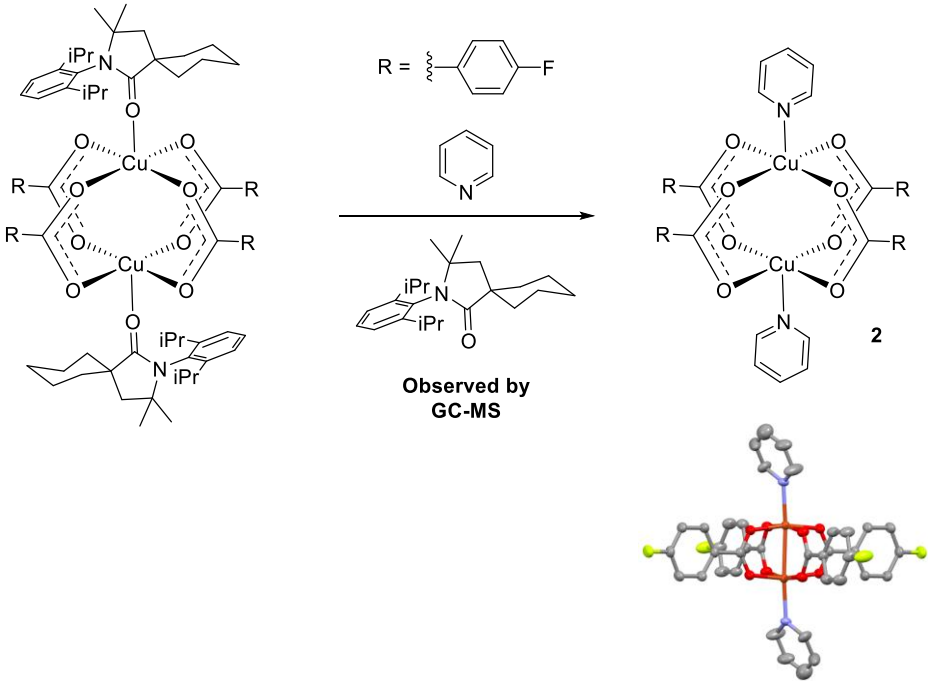

Figure 4.11. Resultant complex from ligand substitution with the copper paddlewheel complex.

4.3. Conclusion

Dehydrogenation of formanilides was found afford isocyanates in low yields, as decarbonylation was found to be an unavoidable and catalyst-deactivating competing reaction. Several catalysts and conditions were tested, but none were able to overcome the decarbonylation side process.

After work on the dehydrogenation system was concluded, a publication by Milstein and coworkers emerged reporting the synthesis of ureas and carbamates through a dehydrogenative process from formanilides.[29] They report the use of a Ru(PNP)H(CO) catalyst for dehydrogenation, proposing the formation of an isocyanate intermediate. They provide evidence for this assertion by isolating a crystal of a Ru–NCO complex bearing an isocyanate ligand derived from formamide dehydrogenation along with DFT analysis showing the plausibility of an isocyanate intermediate.

Discrete copper NHC complexes bearing –NCO ligands were synthesized but attempts at cross-coupling with these complexes were not successful. Aryl halides did not react with these complexes, while benzoyl peroxide derivatives oxidized the carbene ligands rather than promoting isocyanation.

4.4. Experimental Procedures and Characterization

4.4.1. General Experimental

NMR spectra were recorded at room temperature on a Varian vnmrs 500 (500 MHz for ^{1}H, 202 MHz for ^{31}P) and a Varian M400 (400 MHz for ^{1}H, 377 MHz for ^{19}F). NMR spectrometer with the residual solvent peak ($CDCl_3$: ^{1}H: $\delta = 7.26$ ppm, CD_2Cl_2 ^{1}H: $\delta = 5.30$ ppm) as the internal reference. Chemical shifts are reported in parts per million (ppm, δ) relative to tetramethylsilane as an external reference at 0.00 ppm. Multiplicities are reported as follows: s (singlet), d (doublet), t (triplet), q (quartet), hept (heptet), m (multiplet). Coupling constants (*J*) are reported in Hz. Yields for dehydrogenation reactions were determined by GC-FID using anisole as standard.

The following compounds were synthesized according to literature procedures: 4-*t*-butylformanilide,[30] $RuCl_2(PPh_3)_3$,[31] Cp*Ir(py-O)Cl,[32] (phen)$Ru(CO)_2Cl_2$,[33] Ru-^{iPr}MACHO-BH Ru-^{Cy}MACHO-BH,[34] IPrCuCl, SIPrCuCl, IMesCuCl, ICyCuCl,[35] ^{Cy}CAAC, (^{Cy}CAAC)CuCl.[36] $RuH_2(PPh_3)_4$, $[RuCl_2(C_6Me_6)]_2$, Ru(triphos)(OAc)Cl, and bis(4-fluorobenzoyl) peroxide were synthesized by previous group members. (^{iPr}POCOP)IrH_2 and (^{iPr}POCOP)Ir(CO) were generously donated by the Goldburg group. Ru-MACHO-BH and $RuCl_3 \cdot 3H_2O$ were purchased from Strem. Haloarenes were purchased from Oakwood, Alfa, and Acros. 1,2-diphenylphosphinoethane and 4-methoxyformanilide were purchased from TCI. CuCl, IPr, SIPr, IMes, and ICy were purchased from Aldrich. $MeNO_2$-d_3 purchased from Acros. $CDCl_3$ and CD_2Cl_2 were purchased from Cambridge Isotope Laboratories. Ethanol (EtOH) was purchased from Koptec. Chloroform was purchased from BDH. Dichloromethane (DCM), 2-propanol (iPA), ethyl acetate (EtOAc), hexanes, sodium bicarbonate, sodium carbonate, sodium sulfate, and potassium hydroxide were purchased from Fisher Scientific. Methanol (MeOH) was purchased from VWR International. Diethyl ether (Et_2O) and pentane were purchased from Fisher Scientific and either used as received (stabilized) or purified by an Innovative Technologies solvent purification system consisting of a copper catalyst, activated alumina, and molecular sieves (see details below for which was used). Tetrahydrofuran (THF) was purchased from VWR International and purified by an Innovative Technologies solvent purification system consisting of a copper catalyst, activated alumina, and molecular sieves.

4.4.2. Experimental Procedures - Dehydrogenation

General Procedure of Neat Dehydrogenation

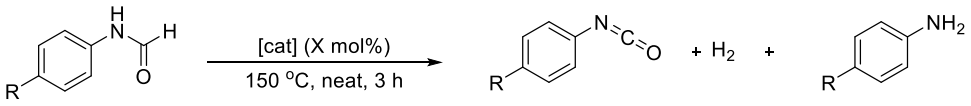

In a nitrogen filled glovebox, substrate (1.5 mmol, 1 eq.) and catalyst (0.001 mmol, 0.00064 eq.) followed by a small stir bar were added to a 2 mL vial. The vial was capped and removed from the glovebox. The vial was then submerged in a sand bath preheated to 150 °C and stirred for 3 h. The vial was removed from the sand bath and allowed to cool to room temperature before being returned to the glovebox. The vial was opened and anisole (40 µL) was added as standard. The mixture was then transferred to a larger vial, diluting and washing with DCM. The reaction was then analyzed by GC-FID.

Stoichiometric Dehydrogenation Procedure

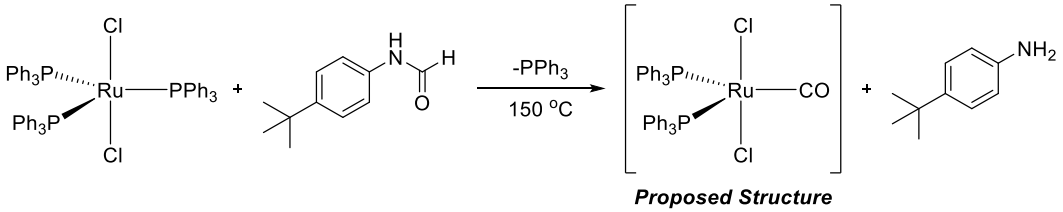

Proposed Structure

In a nitrogen filled glovebox, 4-*t*-butylformanilide (50 mg, 0.28 mmol, 1 eq.) and $RuCl_2(PPh_3)_3$ (271 mg, 0.28 mmol, 1 eq.) were added to a 2 mL vial containing a stir bar. The vial was capped and removed from the glovebox. The vial was then submerged in a sand bath preheated to 150 °C and stirred for 3 h. The vial was removed from the sand bath and allowed to cool to room temperature before being returned to the glovebox. The vial was then uncapped and diluted with

CD_2Cl_2. A portion of the resultant solution was then added to a dry screw-top NMR tube, which was then sealed and removed from the glovebox. Reaction analyzed by ^{31}P.

^{31}P NMR (202 MHz, Methylene Chloride-d_2) δ 46.56 (d, J = 37.2 Hz), 44.65 (d, J = 34.2 Hz), 38.38 (d, J = 25.0 Hz), 36.28, 25.09, -7.97 (d, J = 10.5 Hz).

General Procedure of Dehydrogenation in Solvent under Reflux

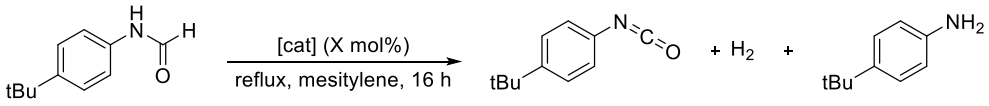

In a nitrogen filled glovebox, 4-*t*-butylformanilide (177 mg, 1 mmol, 1 eq.) and catalyst (0.01 mmol, 0.01 eq.) followed by a small stir bar were added to a 5 mL round bottom flask. Mesitylene (1.2 mL) was then added to the flask. The flask was fixed with a reflux condenser and sealed with a rubber septum, then the flask was taped both at the condenser-flask joint and the condenser-septa joint. The vial was then removed from the glovebox and submerged in an oil bath preheated to 170 °C and stirred for 16 h, with a nitrogen inlet into the condenser. The flask was removed from the oil bath and allowed to cool to room temperature before the condenser was removed and the flask was quickly sealed with a septum. The flask was briefly purged with nitrogen, then returned to the glovebox. The flask was opened and anisole (40 μL) was added as standard. The mixture was then transferred to a vial, diluting and washing with DCM. The reaction was then analyzed by GC-FID.

Procedure for Dehydrogenation with added CO

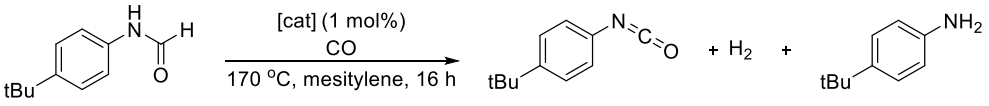

Vial, bubbled: In a nitrogen filled glovebox, 4-*t*-butylformanilide (177 mg, 1 mmol, 1 eq.) and catalyst (0.01 mmol, 0.01 eq.) were added to a 4 mL vial followed by a stir bar. Mesitylene (1.2 mL) was added to the vial, and the vial was capped with a septa cap and removed from the glovebox. A balloon of CO was inserted through the septa then the vial was vented, and CO was bubbled through for 2 min. The vial was then inserted into a hot plate preheated to 150 °C and stirred for 16 h. The vial was removed from the plate and allowed to cool to room temperature before being returned to the glovebox. The vial was opened and anisole (40 μL) was added as standard. The mixture was then transferred to a larger vial, diluting and washing with DCM. The reaction was then analyzed by GC-FID.

Vial, balloon: In a nitrogen filled glovebox, 4-*t*-butylformanilide (177 mg, 1 mmol, 1 eq.) and catalyst (0.01 mmol, 0.01 eq.) were added to a 4 mL vial followed by a stir bar. Mesitylene (1.2 mL) was added to the vial, and the vial was capped with a septa cap and removed from the glovebox. A balloon of CO was inserted through the septa. The vial was then inserted into a hot plate preheated to 150 °C and stirred for 16 h. The balloon was removed, and the vial was removed from the plate and allowed to cool to room temperature before being returned to the glovebox. The vial was opened and anisole (40 μL) was added as standard. The mixture was then transferred to a larger vial, diluting and washing with DCM. The reaction was then analyzed by GC-FID.

Flask: In a nitrogen filled glovebox, 4-*t*-butylformanilide (177 mg, 1 mmol, 1 eq.) and catalyst (0.01 mmol, 0.01 eq.) followed by a small stir bar were added to a 5 mL round bottom flask.

Mesitylene (1.2 mL) was then added to the flask. The flask was fixed with a reflux condenser and sealed with a rubber septum, then the flask was taped both at the condenser-flask joint and the condenser-septa joint. The vial was then removed from the glovebox and submerged in an oil bath preheated to 170 °C and stirred for 16 h, with a balloon of CO into the condenser. The flask was removed from the oil bath and allowed to cool to room temperature before the condenser was removed and the flask was quickly sealed with a septum. The flask was briefly purged with nitrogen, then returned to the glovebox. The flask was opened and anisole (40 μL) was added as standard. The mixture was then transferred to a larger vial, diluting and washing with DCM. The reaction was then analyzed by GC-FID.

4.4.3. Experimental Procedures – Copper Isocyanate Complexes

Synthesis of (Carbene)CuNCO

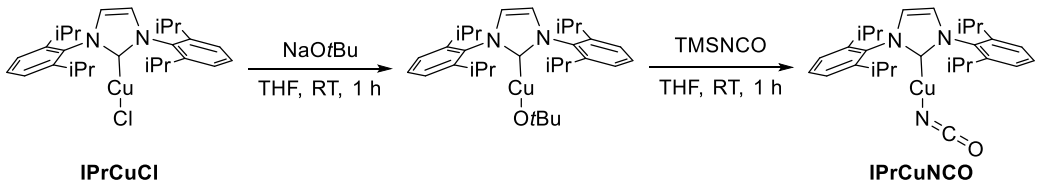

IPrCuCl **IPrCuNCO**

Example shows synthesis with IPr ligand. In a nitrogen filled glovebox, (carbene)CuCl (1 eq.) was dissolved in THF (0.1 M) in a 20 mL vial containing a stir bar. Sodium *t*-butoxide (2 eq.) was suspended in THF (0.27 M measured as if dissolved) then transferred to the solution of Cu in THF. The mixture was then stirred for 1 h. TMSNCO (2 eq.) was dissolved in THF (0.82 M) then added to the reaction mixture. The mixture was then stirred for 1 h. The reaction mixture was then passed through a silica plug in a pipet, then the solvent was removed *in vacuo*. The solid was then dissolved in minimal THF and filtered through celite. Pentane was slowly added to the solution

until precipitate formed, then the mixture was capped and put in the freezer (-35 °C) for at least one hour. The solids were then collected by filtration, then dried *in vacuo*.

IPrCuNCO ^{1}H NMR (700 MHz, Methylene Chloride-d_2) δ 7.53 (tt, J = 7.8, 2.4 Hz, 2H), 7.33 (dt, J = 7.9, 2.5 Hz, 4H), 7.16 (t, J = 2.5 Hz, 2H), 2.52 (dtt, J = 10.1, 6.7, 4.3 Hz, 2H), 1.23 (ddt, J = 31.2, 7.1, 2.4 Hz, 12H), 1.14 (dq, J = 9.0, 3.7, 2.9 Hz, 12H).

SIPrCuNCO ^{1}H NMR (401 MHz, Methylene Chloride-d_2) δ 7.43 (t, J = 7.8 Hz, 4H), 7.27 (d, J = 7.8 Hz, 8H), 3.99 (s, 8H), 3.03 (hept, J = 7.8 Hz, 8H), 1.32 (t, J = 6.2 Hz, 24H).

(^{Cy}CAAC)CuNCO ^{1}H NMR (401 MHz, Nitromethane) δ 7.48 (dd, J = 8.5, 6.9 Hz, 1H), 7.38 (d, J = 7.3 Hz, 2H), 2.94 (hept, J = 7.2 Hz, 2H), 2.18 (s, 2H), 2.03 (t, J = 12.4 Hz, 2H), 1.90 – 1.81 (m, 2H), 1.75 – 1.67 (m, 2H), 1.61 (d, J = 12.9 Hz, 2H), 1.56 – 1.45 (m, 2H), 1.40 (s, 6H), 1.33 (d, J = 6.8 Hz, 6H), 1.25 (d, J = 6.7 Hz, 6H).

General Procedure for Coupling with Aryl Halides

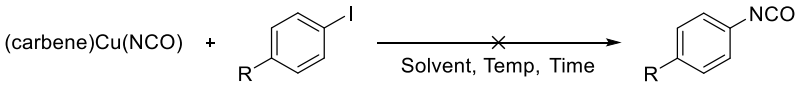

In a nitrogen filled glovebox, (carbene)CuNCO (1.25 eq.) and aryl halide (1 eq.) were added to a 4 mL vial containing a stir bar. Solvent (1 mL) was added and the vial was sealed. The vial was then removed from the glovebox and heated on a pre-heated hot plate overnight. The vial was then allowed to cool to room temperature before being returned to the glovebox. The reaction was

then filtered and diluted with DCM. The reaction was then analyzed by GC-MS to attempt observation of product.

Synthesis of 1

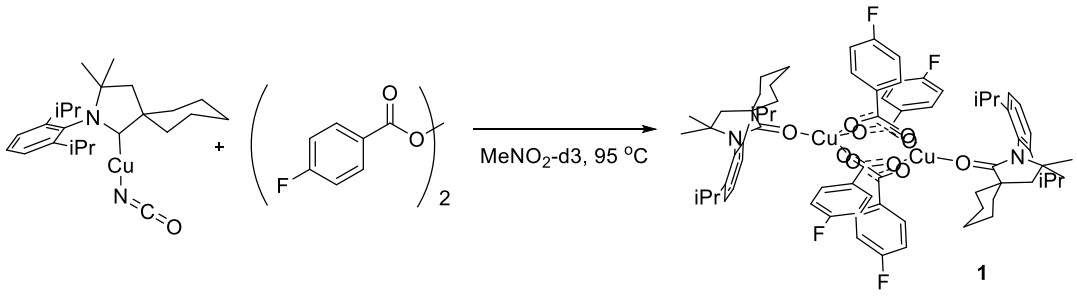

In a nitrogen filled glove box, **(^{Cy}CAAC)CuNCO** (1 eq.) and bis(4-fluorobenzoyl) peroxide (0.5 eq.) were added to a 4 mL vial containing a stir bar. $MeNO_2$-d_3 (1 mL) was added, then the vial was sealed. The vial was removed from the glovebox and inserted into a hot plate pre-heated to 95 °C for several minutes. When the reaction turned a strong blue color the vial was removed from the plate. The vial was allowed to cool to room temperature then returned to the glovebox. The vial was then opened, and a portion of the reaction solution was transferred to a dry screw-top NMR tube. The tube was then sealed, and the reaction was analyzed by ^{19}F NMR and ^{1}H NMR. Crystals were grown under air from THF/Et_2O.

Synthesis of 2

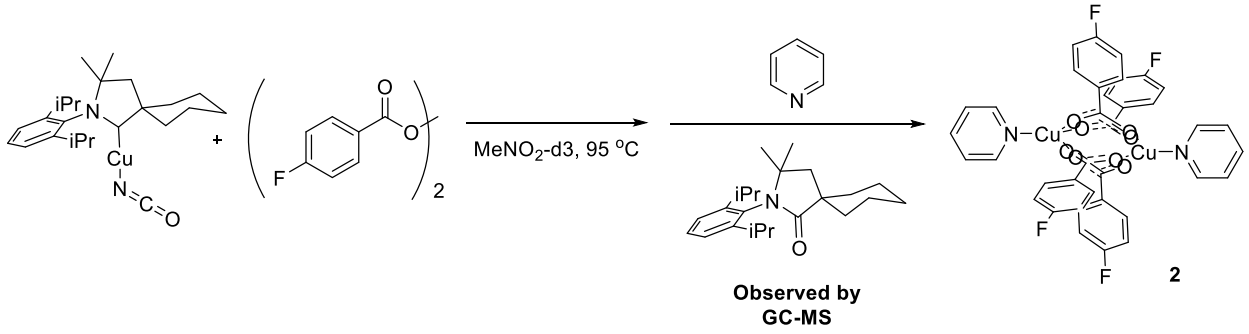

In a nitrogen filled glove box, **(^{Cy}CAAC)CuNCO** (7.5 mg, 0.017 mmol, 1 eq.) and bis(4-fluorobenzoyl) peroxide (2.4 mg, 0.009 mmol, 0.5 eq.) were added to a 4 mL vial containing a stir bar. $MeNO_2$-d_3 (~600 μL) was added, then the vial was sealed. The vial was removed from the glovebox and inserted into a hot plate pre-heated to 95 °C for several minutes. When the reaction turned a strong blue color the vial was removed from the plate. The vial was allowed to cool to room temperature then returned to the glovebox. The vial was then opened, and a portion of the reaction solution was transferred to a dry screw-top NMR tube. The tube was then sealed, and the reaction was analyzed by ^{19}F NMR and ^{1}H NMR. The NMR tube was then returned to the glovebox, and several drops of pyridine were added. The NMR tube was thoroughly mixed and analyzed again by ^{19}F and ^{1}H NMR. The crystals were grown under air from THF/pentane.

4.4.4. X-ray Crystallographic Data

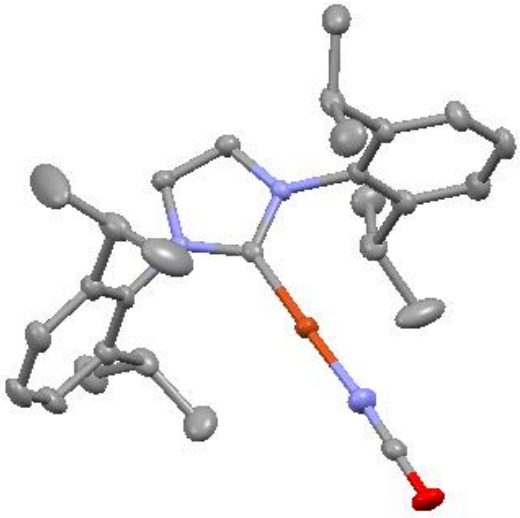

Structure Determination.

Colorless blocks of **IPrCuNCO** were grown from a tetrahydrofuran/pentane solution of the compound at 22 deg. C. A crystal of dimensions 0.20 x 0.20 x 0.18 mm was mounted on a Rigaku AFC10K Saturn 944+ CCD-based X-ray diffractometer equipped with a low temperature device and Micromax-007HF Cu-target micro-focus rotating anode (l = 1.54187 A) operated at 1.2 kW power (40 kV, 30 mA). The X-ray intensities were measured at 85(1) K with the detector placed at a distance 42.00 mm from the crystal. A total of 2028 images were collected with an oscillation width of 1.0° in w. The exposure times for images were 1 sec. Rigaku d*trek images were exported to CrysAlisPro for processing and corrected for absorption. The integration of the data yielded a total of 41199 reflections to a maximum 2q value of 138.50° of which 5005 were independent and 4996 were greater than 2s(I). The final cell constants were based on the xyz centroids of 34909 reflections above 10s(I). Analysis of the data showed negligible decay during data collection. The structure was solved and refined with the Bruker SHELXTL (version 2016/6) software package, using the space group P2(1)2(1)2(1) with Z = 4 for the formula $C_{28}H_{36}N_3OCu$. All non-hydrogen

atoms were refined anisotropically with the hydrogen atoms placed in idealized positions. Full matrix least-squares refinement based on F^2 converged at R1 = 0.0295 and wR2 = 0.0748 [based on I > 2sigma(I)], R1 = 0.0296 and wR2 = 0.0748 for all data. Acknowledgement is made for funding from NSF grant CHE-0840456 for X-ray instrumentation.

G.M. Sheldrick (2015) "Crystal structure refinement with SHELXL", Acta Cryst., C71, 3-8 (Open Access).

CrystalClear Expert 2.0 r16, Rigaku Americas and Rigaku Corporation (2014), Rigaku Americas, 9009, TX, USA 77381-5209, Rigaku Tokyo, 196-8666, Japan.

CrysAlisPro 1.171.38.41 (Rigaku Oxford Diffraction, 2015).

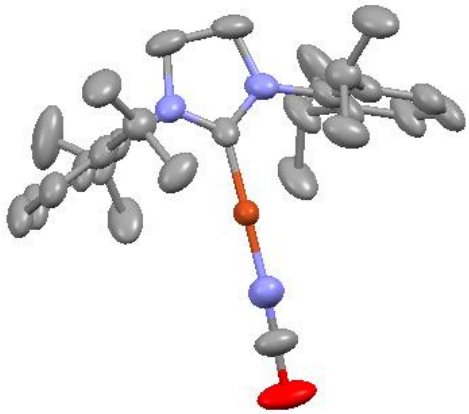

Structure Determination.

Colorless plates of **SIPrCuNCO** were grown from a tetrahydrofuran/pentane solution of the compound at 23 deg. C. A crystal of dimensions 0.10 x 0.08 x 0.02 mm was mounted on a Rigaku AFC10K Saturn 944+ CCD-based X-ray diffractometer equipped with a low temperature device and Micromax-007HF Cu-target micro-focus rotating anode (l = 1.54187 A) operated at 1.2 kW power (40 kV, 30 mA). The X-ray intensities were measured at 85(1) K with the detector placed at a distance 42.00 mm from the crystal A total of 2028 images were collected with an oscillation width of 1.0° in w. The exposure times were 2 sec. for the low angle images, 15 sec. for high angle. Rigaku d*trek images were exported to CrysAlisPro for processing and corrected for absorption. The integration of the data yielded a total of 43695 reflections to a maximum 2q value of 142.60° of which 2988 were independent and 2562 were greater than 2s(I). The final cell constants were based on the xyz centroids of 10236 reflections above 10s(I). Analysis of the data showed negligible decay during data collection. The structure was solved and refined with the Bruker SHELXTL (version 2016/6) software package, using the space group Pbcm with Z = 4 for the formula $C_{28}H_{34}N_3OCu,(C_4H_8O)_{0.5}$. All non-hydrogen atoms were refined anisotropically with the hydrogen atoms placed in idealized positions. The complex lies on a two-fold rotation

axis of the lattice. The isocyanato ligand is disordered in two orientations about the two-fold. Full matrix least-squares refinement based on F^2 converged at R1 = 0.0941 and wR2 = 0.2320 [based on I > 2sigma(I)], R1 = 0.1053 and wR2 = 0.2429 for all data. The SQUEEZE subroutine of the PLATON program suite was used to address the disordered tetrahydrofuran lattice solvates present in the structure. Acknowledgement is made for funding from NSF grant CHE-0840456 for X-ray instrumentation.

G.M. Sheldrick (2015) "Crystal structure refinement with SHELXL", Acta Cryst., C71, 3-8 (Open Access).

CrystalClear Expert 2.0 r16, Rigaku Americas and Rigaku Corporation (2014), Rigaku Americas, 9009, TX, USA 77381-5209, Rigaku Tokyo, 196-8666, Japan.

CrysAlisPro 1.171.38.41 (Rigaku Oxford Diffraction, 2015).

- PLATON Reference : Spek, A.L. (2003). J. Appl. Cryst. 36, 7-13.

Spek, A.L. (2009). Acta Cryst. D65, 148-155., v. 51012.

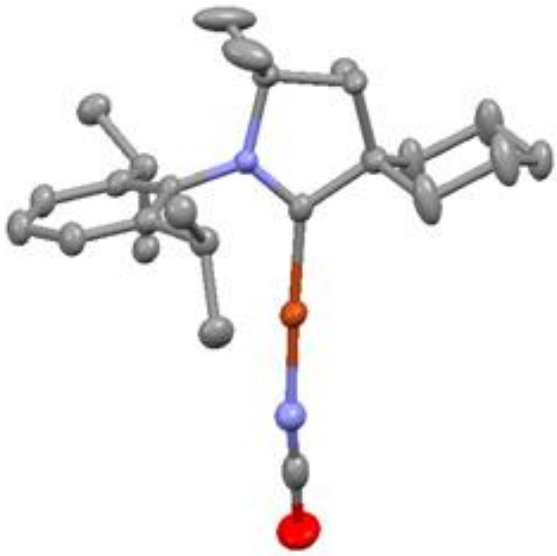

Structure Determination.

Colorless needles of **(^{Cy}CAAC)CuNCO** were grown from a tetrahydrofuran/pentane solution of the compound at 22 deg. C. A crystal of dimensions 0.12 x 0.02 x 0.02 mm was mounted on a Rigaku AFC10K Saturn 944+ CCD-based X-ray diffractometer equipped with a low temperature device and Micromax-007HF Cu-target micro-focus rotating anode (l = 1.54187 A) operated at 1.2 kW power (40 kV, 30 mA). The X-ray intensities were measured at 85(1) K with the detector placed at a distance 42.00 mm from the crystal. A total of 2028 images were collected with an oscillation width of 1.0° in w. The exposure times were 10 sec. for the low angle images, 75 sec. for high angle. Rigaku d*trek images were exported to CrysAlisPro for processing and corrected for absorption. The integration of the data yielded a total of 33979 reflections to a maximum 2q value of 135.37° of which 4151 were independent and 3148 were greater than 2s(I). The final cell constants were based on the xyz centroids of 5971 reflections above 10s(I). Analysis of the data showed negligible decay during data collection. The structure was solved and refined with the Bruker SHELXTL (version 2018/3) software package, using the space group P2(1)/n with Z = 4 for the formula $C_{24}H_{35}N_2OCu$. All non-hydrogen atoms were refined anisotropically with

the hydrogen atoms placed in idealized positions. Full matrix least-squares refinement based on F^2 converged at R1 = 0.0529 and wR2 = 0.1262 [based on I > 2sigma(I)], R1 = 0.0737 and wR2 = 0.1438 for all data. Acknowledgement is made for funding from NSF grant CHE-0840456 for X-ray instrumentation.

G.M. Sheldrick (2015) "Crystal structure refinement with SHELXL", Acta Cryst., C71, 3-8 (Open Access).

CrystalClear Expert 2.0 r16, Rigaku Americas and Rigaku Corporation (2014), Rigaku Americas, 9009, TX, USA 77381-5209, Rigaku Tokyo, 196-8666, Japan.

CrysAlisPro 1.171.38.41 (Rigaku Oxford Diffraction, 2015).

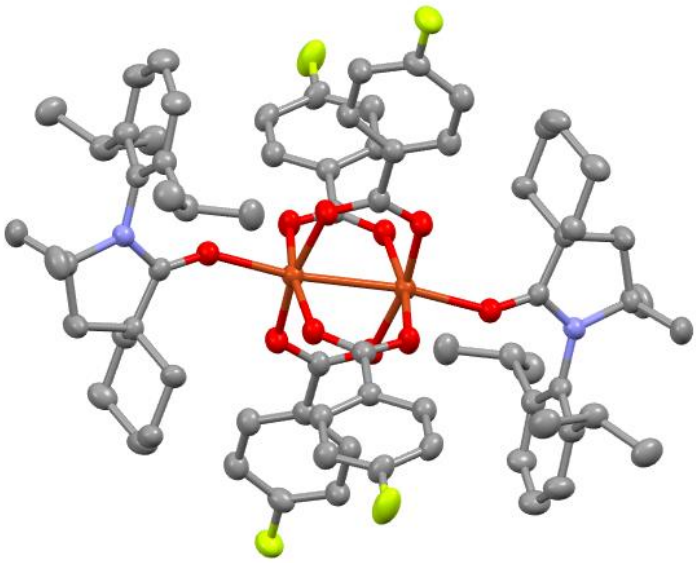

Structure Determination.

Blue plates of **1** were grown from a tetrahydrofuran/diethyl ether solution of the compound at 25 deg. C. A crystal of dimensions 0.11 x 0.10 x 0.04 mm was mounted on a Rigaku AFC10K Saturn 944+ CCD-based X-ray diffractometer equipped with a low temperature device and Micromax-007HF Cu-target micro-focus rotating anode (l = 1.54187 A) operated at 1.2 kW power (40 kV, 30 mA). The X-ray intensities were measured at 85(1) K with the detector placed at a distance 42.00 mm from the crystal. A total of 2028 images were collected with an oscillation width of 1.0° in w. The exposure times were 5 sec. for the low angle images, 35 sec. for high angle. Rigaku d*trek images were exported to CrysAlisPro for processing and corrected for absorption. The integration of the data yielded a total of 52601 reflections to a maximum 2q value of 139.08° of which 6402 were independent and 4809 were greater than 2s(I). The final cell constants were based on the xyz centroids of 8827 reflections above 10s(I). Analysis of the data showed negligible decay during data collection. The structure was solved and refined with the Bruker SHELXTL (version 2018/3) software package, using the space group P2(1)/c with Z = 2 for the formula

$C_{74}H_{86}N_2O_{10}F_5Cu_2$. All non-hydrogen atoms were refined anisotropically with the hydrogen atoms placed in idealized positions. Full matrix least-squares refinement based on F^2 converged at R1 = 0.0560 and wR2 = 0.1470 [based on I > 2sigma(I)], R1 = 0.0767 and wR2 = 0.1687 for all data. Acknowledgement is made for funding from NSF grant CHE-0840456 for X-ray instrumentation.

G.M. Sheldrick (2015) "Crystal structure refinement with SHELXL", Acta Cryst., C71, 3-8 (Open Access).

CrystalClear Expert 2.0 r16, Rigaku Americas and Rigaku Corporation (2014), Rigaku Americas, 9009, TX, USA 77381-5209, Rigaku Tokyo, 196-8666, Japan.

CrysAlisPro 1.171.38.41 (Rigaku Oxford Diffraction, 2015).

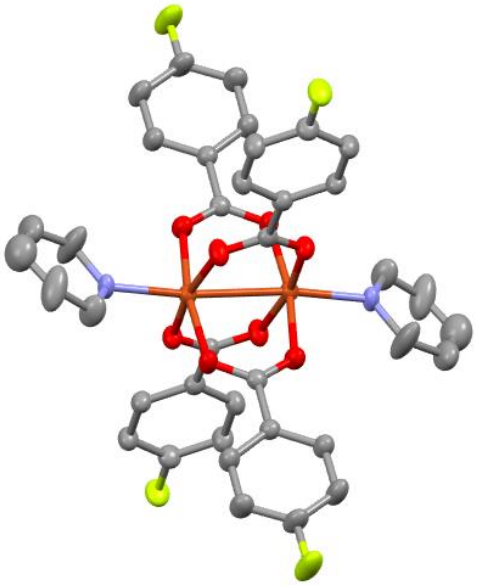

Structure Determination.

Blue needles of **2** were grown from a nitromethane-d3 solution of the compound at 22 deg. C. A crystal of dimensions 0.10 x 0.03 x 0.2 mm was mounted on a Rigaku AFC10K Saturn 944+ CCD-based X-ray diffractometer equipped with a low temperature device and Micromax-007HF Cu-target micro-focus rotating anode (l = 1.54187 A) operated at 1.2 kW power (40 kV, 30 mA). The X-ray intensities were measured at 85(1) K with the detector placed at a distance 42.00 mm from the crystal. A total of 2028 images were collected with an oscillation width of 1.0° in w. The exposure times were 1 sec. for the low angle images, 3 sec. for high angle. Rigaku d*trek images were exported to CrysAlisPro for processing and corrected for absorption. The integration of the data yielded a total of 50573 reflections to a maximum 2q value of 138.56° of which 3254 were independent and 2914 were greater than 2s(I). The final cell constants were based on the xyz centroids of 13282 reflections above 10s(I). Analysis of the data showed negligible decay during data collection. The structure was solved and refined with the Bruker SHELXTL (version 2018/3) software package, using the space group Pbca with Z = 4 for the formula $C_{38}H_{26}N_2O_8F_4Cu_2$.

The complex lies on an inversion center of the crystal lattice. All non-hydrogen atoms were refined anisotropically with the hydrogen atoms placed in idealized positions. Full matrix least-squares refinement based on F^2 converged at R1 = 0.0492 and wR2 = 0.1496 [based on I > 2sigma(I)], R1 = 0.0545 and wR2 = 0.1564 for all data. Acknowledgement is made for funding from NSF grant CHE-0840456 for X-ray instrumentation.

G.M. Sheldrick (2015) "Crystal structure refinement with SHELXL", Acta Cryst., C71, 3-8 (Open Access).

CrystalClear Expert 2.0 r16, Rigaku Americas and Rigaku Corporation (2014), Rigaku Americas, 9009, TX, USA 77381-5209, Rigaku Tokyo, 196-8666, Japan.

CrysAlisPro 1.171.38.41 (Rigaku Oxford Diffraction, 2015).

4.5. References

[1] Ghosh, A. K.; Brindisi, M. Urea derivatives in modern drug discovery and medicinal chemistry. *J. Med. Chem.* **2019**, *ASAP*.
[2] Gallou, I. Unsymmetrical ureas. Synthetic methodologies and application in drug design. *Org. Prep. Proced. Int.* **2007**, *39*, 355.
[3] Brereton, G., Emanuel, R.M., Jr, Lomax, R., Pennington, K., Ryan, T., Tebbe, H., Timm, M., Ware, P., Winkler, K., Yuan, T., Zhu, Z., Adam, N., Avar, G., Blankenheim, H., Friederichs, W., Giersig, M., Weigand, E., Halfmann, M., Wittbecker, F.-W., Larimer, D.-R., Maier, U., Meyer-Ahrens, S., Noble, K.-L. and Wussow, H.-G. Polyurethanes. *Ullmann's Encyclopedia of Industrial Chemistry* **2019**.
[4] Six, C.; Richter, F. Isocyanates, Organic. *Ullman's Encuclopedia of Industrial Chemistry* **2003**.
[5] Crabtree, R. H.; Mihelcic, J. M.; Quirk, J. M.; Iridium complexes in alkane dehydrogenation. *J. Am. Chem. Soc.* **1979**, *101*, 7738-7740.
[6] Crabtree, R. H.; Demou, P. C.; Eden, D.; Mihelcic, J. M.; Parnell, C. A.; Quirk, J. M.; Morris, G. E.; Dihydrido olefin and solvento complexes of iridium and the mechanisms of olefin hydrogenation and alkane dehydrogenation. *J. Am. Chem. Soc.* **1982**, *104*, 6994-7001.
[7] Baudrey, D.; Ephritikhine, M.; Felkin, H.; Zakrzewski, J.; The selective conversion of n-pentane into pent-1-ene via Trihydrido(trans-penta-1,3-diene)bis(triarylphosphine)rhenium. *J. Chem. Soc. Commun.* **1982**, 1235-1236.
[8] Gupta, M.; Hagen, C.; Flesher, R. J.; Kaska, W. C.; Jensen, C. M. A Highly active alkane dehydrogenation catalyst: stabilization of dihydrido Rh and Ir complexes by a P-C-P pincer ligand. *Chem. Commun.* **1996**, 2083−2084.

[9] Xu, W.; Rosini, G. P.; Gupta, M.; Jensen, C. M.; Kaska, W. C.; Krogh-Jespersen, K.; Goldman, A. S. Thermochemical alkane dehydrogenation catalyzed in solution without the use of a hydrogen acceptor. *Chem. Commun*. **1997**, 2273−2274.

[10] Liu, F.; Pak, E. B.; Singh, B.; Jensen, C. M.; Goldman, A. S. Dehydrogenation of n-alkanes catalyzed by iridium "pincer" complexes. regioselective formation of alpha-olefins. *J. Am. Chem. Soc.* **1999**, *121*, 4086−4087.

[11] Morales-Morales, D.; Redon, R.; Yung, C.; Jensen, C. M. Dehydrogenation of alkanes catalyzed by an iridium phosphinito PCP pincer complex. *Inorg. Chim. Acta* **2004**, *357*, 2953−2956.

[12] Göttker-Schnetmann, I.; Brookhart, M. Mechanistic studies of the transfer dehydrogenation of cyclooctane catalyzed by iridium bis(phosphinite) p-XPCP pincer complexes. *J. Am. Chem. Soc.* **2004**, *126*, 9330−9338.

[13] Crabtree, R. H.; Homogeneous transition metal catalysis of acceptorless dehydrogenative alcohol oxidation: applications in hydrogen storage and to heterocycle synthesis. *Chem. Rev.* **2017**, *117*, 9228−9246

[14] Smith, T. A.; Aplin, R. P.; Maitlis, P. M. The ruthenium catalysed conversion of methanol into methyl formate. *J. Organomet. Chem.* **1985**, *291*, c13−c14.

[15] Blum, Y.; Shvo, Y.; Chodosh, D. F.; Structure of $(Ph_4C_4CO)(CO)_3Ru$ - a catalyst precursor in H-transfer and dehydrogenation reactions of alcohols. *Inorg. Chim. Acta* **1985**, *97*, L25−L26.

[16] Nielsen, M.; Kammer, A.; Cozzula, D.; Junge, H.; Gladiali, S.; Beller, M. Efficient hydrogen production from alcohols under mild reaction conditions. *Angew. Chem., Int. Ed.* **2011**, *50*, 9593−9597.

[17] Yamaguchi, K.; Mizuno, N.; Efficient heterogeneous aerobic oxidation of amines by a supported ruthenium catalyst. *Angew. Chem. Int. Ed.* **2003**, *42*, 1480-1483.

[18] Gu, X. Q.; Chen, W.; Morales-Morales, D.; Jensen, C. M.; Dehydrogenation of secondary amines to imines catalyzedby an iridium PCP pincer complex: initial aliphaticor direct amino dehydrogenation? *J. Mol. Catal. A: Chem.* **2002**, *189*, 119-124.

[19] Khai, B. T.; Concilio, C.; Porzi, G. A facile synthesis of symmetrical secondary amines from primary amines promoted by the homogeneous catalyst $RuCl_2(Ph_3P)_3$. *J. Organomet. Chem.* **1981**, *208*, 249-251.

[20] Kianmehr, E.; Baghersad, M. H. Copper-catalyzed coupling of arylboronic acids with potassium cyanate: a new approach to the synthesis of aryl carbamates. *Adv. Synth. Catal.* **2011**, *353*,

[21] Yang, X.; Zhang, Y.; Ma, D. Synthesis of aryl carbamates *via* copper-catalyzed coupling of aryl halides and potassium cyanate. *Adv. Synth. Catal.* **2012**, *354* 2443-2446.

[22] Yin, H.; Chen, B.; Zhang, X.; Yang, X.; Zhang, Y.; Jiang, Y.; Ma, D. Assembly of *N,N*-disubstituted-*N'*-arylureas via a copper-catalyzed one-pot-three-component reaction of aryl bromides, potassium cyanate, and secondary amines. *Tetrahedron* **2013**, *69*, 5326-5330.

[23] Vinogradova, E. V.; Fors, B. P.; Buchwald, S. L. Palladium-catalyzed cross-coupling of aryl chlorides and triflates with sodium cyanate: A practical synthesis of unsymmetrical ureas. *J. Am. Chem. Soc.* **2012**, *134*, 11132-11135.

[24] Egbert, J. D.; Cazin, C. S. J.; Nolan, S. P. Copper *N*-heterocyclic carbene complexes in catalysis. *Cat. Sci. Tech.* **2013**, *3*, 912-926.

[25] Bour, J. R.; Kariofillis, S. K.; Sanford, M. S. Synthesis, Reactivity, and Catalytic Applications of Isolable (NHC)Cu(CHF_2) Complexes. *Organometallics* **2017**, *36*, 1220–1223.

[26] Paul, U. S. D.; Sieck, C.; Haehnel, M.; Hammond, K.; Marder, T. B.; Radius, U. Cyclic (alkyl)(amino)carbene complexes of rhodium and nickel and their steric and electronic parameters. *Chem. Eur. J.* **2016**, *22*, 11005-11014.

[27] Bour, J. R.; Ferguson, D. M.; McClain, E. J.; Kampf, J. W.; Sanford, M. S. Connecting organometallic Ni(III) and Ni(IV): Reactions of carbon-centered radicals with high-valent organonickel complexes. *J. Am. Chem. Soc.* **2019**, *141*, 8914–8920.

[28] Li, D.; Ollevier, T. Mechanism studies of oxidation and hydrolysis of Cu(I)–NHC and Ag–NHC in solution under air. *J. Organomet. Chem.* **2020**, *906*, 121025.

[29] Bruffaerts, J.; von Wolff, N.; Diskin-Posner, Y.; Ben-David, Y.; Milstein, D. Formamides as isocyanate surrogates: A mechanistically driven approach to the development of atom-efficient, selective catalytic syntheses of ureas, carbamates, and heterocycles. *J. Am. Chem. Soc.* **2019**, *141*, 16486-16493.

[30] Jia, S.; Su, S.; Li, C.; Jia, X.; Li, J. Multicomponent cascade cycloaddition involving tropone, allenoate, and isocyanide: A rapid access to a 7,6,5-fused tricyclic skeleton. *Org. Lett.* **2014**, *16*, 5604-5607.

[31] Stephenson, T. A.; Wilkinson, G. New Complexes of Ruthenium (II) and (III) with Triphenylphosphine, Triphenylarsine, Trichlorostannate, Pyridine, and other Ligands. *J. Inorg. Nucl. Chem.* **1966**, *28*, 945-956.

[32] Fujita, K. I.; Tanino, N.; Yamaguchi, R. Ligand-promoted dehydrogenation of alcohols catalyzed by Cp*Ir complexes. A new catalytic system for oxidant-free oxidation of alcohols. *Org. Lett.* **2007**, *9*, 109-111.

[33] Valore, A.; Balordi, M.; Colombo, A.; Dragonetti, C.; Righetto, S.; Roberto, D.; Ugo, R.; Benincori, T.; Rampinini, G.; Sannicolo, F.; Demartin, F. Novel ruthenium(ii) complexes with substituted 1,10-phenanthroline or 4,5-

diazafluorene linked to a fullerene as highly active second order NLOchromophores. *Dalton Trans.* **2010**, *39*, 10314-10318.

[34] F. Dumeignil, S. Desset, S. Paul, G. Raffa, L. Zhang, (PIVERT), WO 2015/ 067899 Al, 2015.

[35] Xie, W.; Chang, S. [Cu(NHC)]-Catalyzed C−H allylation and alkenylation of both electron-deficient and electron-rich (hetero)arenes with allyl halides. *Angew. Chem. Int. Ed.* **2016**, *55*, 1876-1880.

[36] Hu, X.; Soleilhavoup, M.; Melaimi, M.; Chu, J.; Bertrand, G. Air-stable (CAAC)CuCl and (CAAC)$CuBH_4$ complexes as catalysts for the hydrolytic dehydrogenation of BH_3NH_3. *Angew. Chem. Int. Ed.* **2015**, *54*, 6008-6011.